STRUCTURE AND DECOMPOSITION OF DIOL INCLUSION COMPOUNDS

by

Hong Su

B.Sc. University of Hunan

The People's Republic of China

A thesis presented to the

UNIVERSITY OF CAPE TOWN

for the degree of

MASTER OF SCIENCE

Department of Chemistry

University of Cape Town

Rondebosch

7701

South Africa

February 1998

ACKNOWLEDGEMENTS

I would like to thank

Professor L. R. Nassimbeni and Dr. A. Coetzee for their excellent supervision, enthusiasm and patience,

Associate Professor M. R. Caira and Dr. S. Bourne for their kind help,

my colleagues in the Crystallography Research Group, for their friendship and help, especially Mr. Davric Dodds for his help in proof reading,

Mr. Klaus Achleitner for his help in GC,

my parents for their love and support,

my husband, Huijie, for help in synthesis of the host compound and his loving encouragement.

ABSTRACT

The inclusion properties of the host, *trans*-9,10-dihydroxy-9,10-diphenyl-9,10-dihydroanthracene, with various guest molecules, namely cyclohexanone, 2-methylcyclohexanone, 3-methylcyclohexanone and 4-methylcyclohexanone, were investigated.

The host to guest ratios were determined by programmed temperature thermogravimetry. Two of the four molecular structures were elucidated using single crystal X-ray diffraction. All the inclusion compounds were also characterised by differential scanning calorimetry, hotstage microscopy and X-ray powder diffraction.

The kinetics of decomposition of the inclusion compound containing the guest cyclohexanone were studied using different experimental techniques under isothermal conditions: these were the quartz microbalance, the levitating balance and isothermal thermogravimetry. The kinetics of decomposition of the other three compounds were studied by means of isothermal thermogravimetry. The Arrhenius parameters determined showed a compensation effect between the activation energies and pre-exponential factors. Competition experiments were performed to determine the selectivity of the host for the four guest substances.

ABBREVIATIONS AND SYMBOLS USED IN THE TEXT

A		Arrhenius pre-exponential factors
α		Extent of reaction
	or	Unsolvated, non-porous phase of the host compound
	or	The angle between *b* and *c* unit cell axes
β		The angle between *a* and *c* unit cell axes
	or	The phase of an inclusion compound
γ		The angle between *a* and *b* unit cell axes
b.p.		Boiling point
CSDS		Cambridge structural database system
DSC		Differential scanning calorimetry
E_a		Activation energy
F		Structure factor
$f(\alpha)$		Kinetic rate expression
GC		Gas chromatography
ΔH		Enthalpy change
iso		Isothermal
k		Rate constant
LB		Levitating balance
m.p.		Melting point
QMB		Quartz microbalance
s.o.f.		Site occupancy factor
T_{on}		Onset temperature
T_b		Boiling temperature
TG		Thermogravimetry
τ		Torsion angle
V		Cell volume
XRD		X-ray powder diffraction
Z		Number of structural units in the unit cell

CONTENTS

CHAPTER 3 KINETIC STUDIES

CHAPTER 4 THERMAL ANALYSES

CHAPTER 5 CRYSTAL STRUCTURE

CHAPTER 1

INTRODUCTION

1. INTRODUCTION

1.1. General introduction

Supramolecular chemistry was defined as chemistry beyond the molecule, by Jean -Marie Lehn who also said: 'supermolecules are to molecules and the intermolecular bond what molecules are to atoms and the covalent bond'[1]. The understanding of intermolecular interactions is therefore very important in the study of supramolecular assemblies. Some important and recent subjects in this field include crystal engineering, which is the design of crystal structures via the intermolecular interactions[2], and molecular recognition, which is 'the strategy by which a molecule bears supramolecular functions'[3]. Another fundamental subject in this field is the chemistry of host-guest inclusion compounds. Crystalline inclusion compounds contain all the information regarding the importance of, and balance between, the intermolecular interactions[4].

The chemistry of inclusion compounds has a long history[5]. It can be dated back to the beginning of the last century when Davy discovered the first inclusion compound, chlorine hydrate ($Cl_2 \cdot 6H_2O$), by bubbling chlorine into cool water[6]. Since then numerous inclusion compounds and host compounds were discovered, most purely by chance. Among them are the graphite intercalations[7], hydroquinone[8], the Hofmann-type inclusion compounds[9], Dianin's compound[10], cyclodextrin inclusion compounds[11], the inclusion compounds of choleic acids[12], of phenols[13], of urea[14] and so on. In the last decade, systematic design and synthesis of host-guest compounds have received a lot of attention[2].

Two distinct categories of supermolecules can be identified among inclusion compounds according to the topology of the host-guest aggregate as proposed by Desiraju[2]: (1) those of which the host is a single molecule within which the whole guest molecule or molecules reside (*e.g.* crown ether[15], cyclodextrins,

corands, cavitands and cryptands[16]), and (2) those where several host molecules are assembled to form a host framework containing voids which can accommodate the guest molecule or molecules. This is schematically illustrated in **Figure 1.1**. The last category consists of the vast majority of inclusion compounds. Examples of inclusion compounds belonging to these two categories are illustrated in **Figure 1.2**. Many other classifications have been proposed and the most widely used one is that according to the host-guest interaction (*e.g.* hydrogen bond, covalent or ionic interaction) as suggested by Weber[17]. This is schematically shown in **Figure 1.3**. However, more detailed classification 'is difficult, not really necessary and could be quite subjective', as summarised by Desiraju[2].

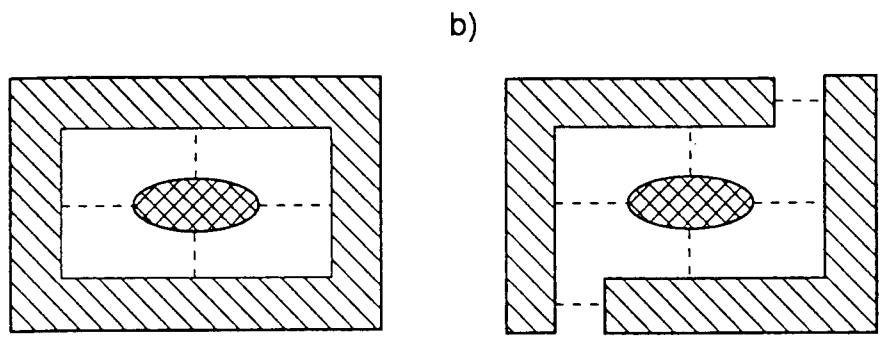

Figure 1.1 Schematic view of two types of inclusion compounds: a) Molecular Inclusion: the host is a single molecule and encloses the guest; b) Crystal Lattice Inclusion: the host network is itself composed of more than one molecule[2].

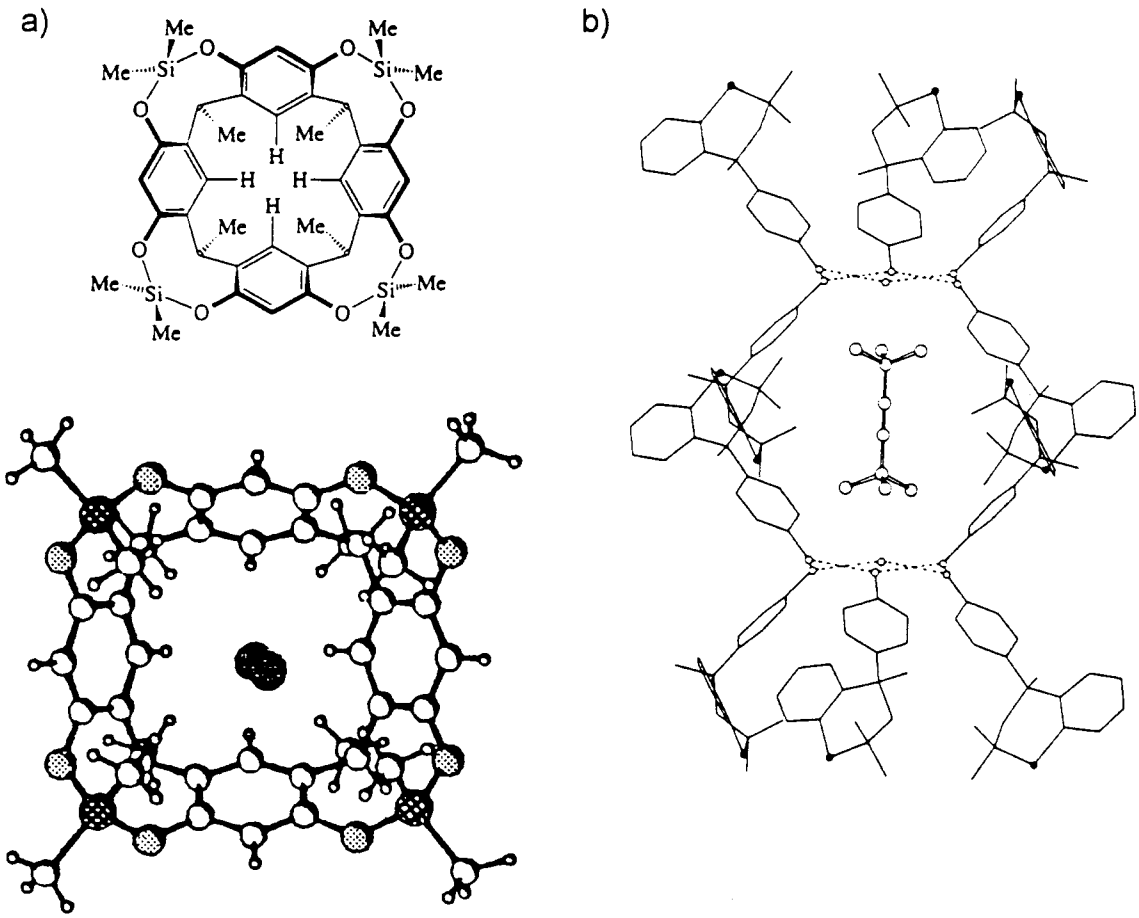

Figure 1.2 a) Structure of the inclusion compound between cavitand (above) and CS_2. In the crystal structure, oxygen atoms are dotted, silicon atoms cross-hatched, and the CS_2 guest shaded[18].
b) Structure of Dianin's compound 4-*p*-hydrophenyl-2,2,4-trimethylthiachroman with guest 2,5,5-trimethylhex-3-yn-2-ol, projected along the *a* axis. Two host molecules have been excluded apart from their hydroxy-oxygen atoms. [19]

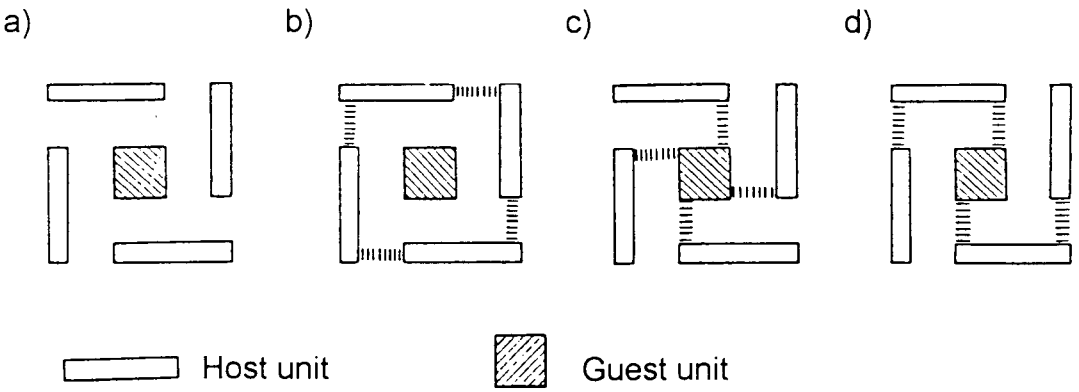

Figure 1.3 Representations of different inclusion compounds dependent on host-host and host-guest interactions. a) no host-guest or host-host interactions, b) host-host interactions only, c) host-guest interactions only and d) host-host and host-guest interactions[17].

1.2. Organic inclusion compounds

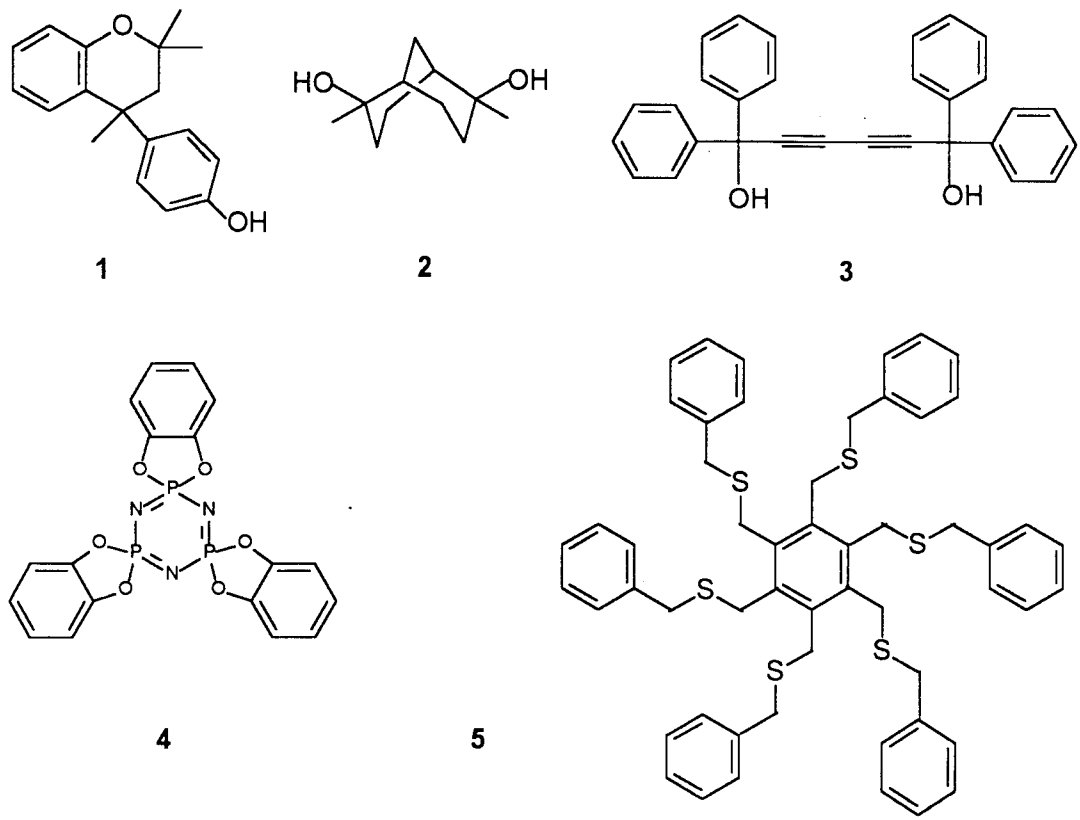

Figure 1.4 Representative examples of well-known organic crystalline host molecules[20].

Some well-established organic host molecules, efficient in lattice inclusion, are shown in **Figure 1.4**. Up to the early 1980's, most of the inclusion compounds were discovered purely by chance[4]. Recently suitable host compounds are often the products of rational design and synthesis. Initially new host compounds were created by simple modification of known hosts. An example of this is the modification of Dianin's compound (**1**)[21]. Upon substituting oxygen with sulphur, the resulting 4-*p*-hydrophenyl-2,2,4-trimethylchroman host (**6**) also forms very similar shaped cavities to those of (**1**) upon crystallisation. The introduction of only one additional methyl group, however, leads to a significant change in the shape as well as size of the host lattice cavity, as shown in **Figure 1.5**. Consequently, this change resulted in a modified selectivity.

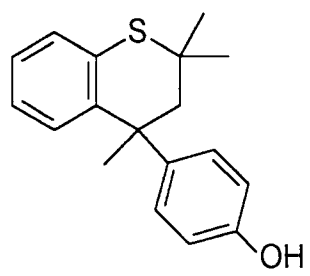

6

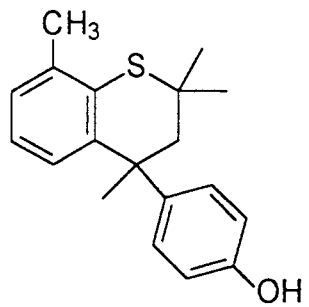

7

(1) a)

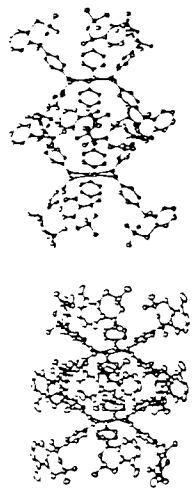

b)

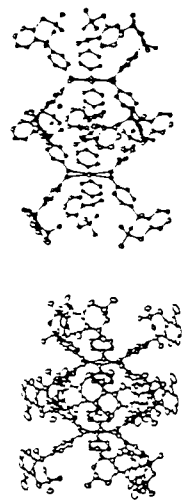

(2) a)

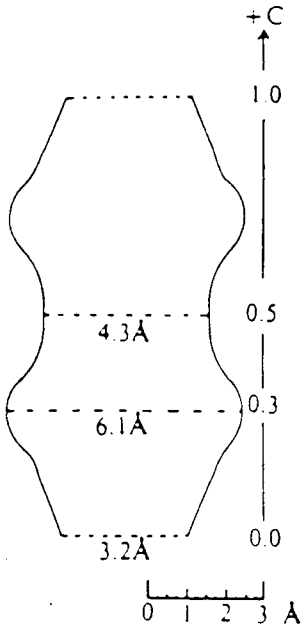

b)

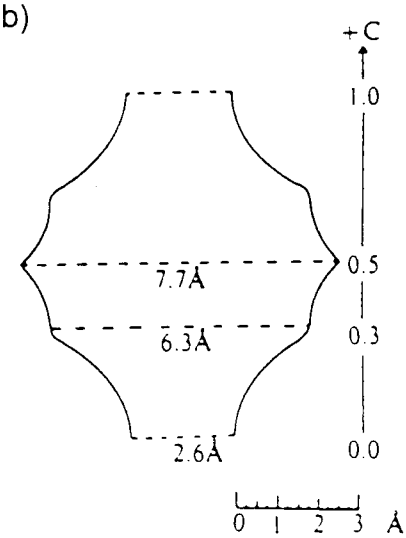

Figure 1.5 (1) Comparative stereoview of a) 4-*p*-hydrophenyl-2,2,4-trimethylthiachroman (**6**) and b) 4-*p*-hydrophenyl-2,2,4,8-tetramethylthiachroman (**7**). (2) Section through the van der Waals surface of a) and b)[21].

Based on the knowledge obtained from the study of crystal structures of known host systems with various guests, an increasing number of new compounds, unrelated to known hosts, have been designed directly. The various concepts of efficient host molecule design have been reviewed and evaluated[22,23,24]. MacNicol[25] pioneered the area of rational host design with the class of compounds called "hexahosts" (*e.g.* (**5**)). This group of compounds were designed by analogy to the host lattice formed by quinol or Dianin's compounds, as shown in **Figure 1.6**.

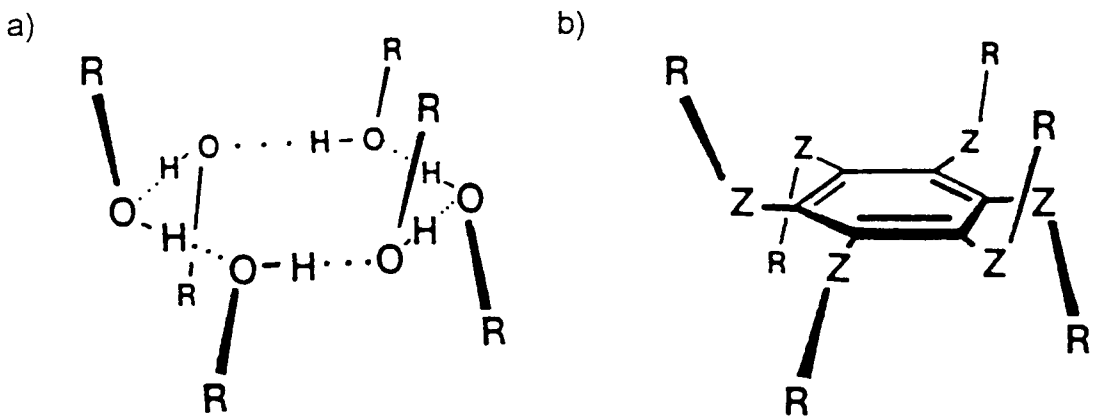

Figure 1.6 Comparison of (a) hydrogen-bonded hexamer lattice unit with (b) hexasubstituted benzene analogue. Z is any bridging group or atoms(usually CH_2) attached directly to the central benzene ring.[25]

Weber[23] has summarised the basic features of an efficient host compound. It should possess molecular bulkiness, rigidity, functional groups (e.g. hydroxygroup) and a degree of symmetry. Bulkiness provides low-density packing. Rigidity helps maintaining the cavity and prevents collapse. The functional group in a suitable position may achieve specific and strong host-guest interactions for molecular recognition. A balance of these features is needed to stabilise the crystal packing. A number of structural building elements, employed to make these principles possible are shown schematically in **Figure 1.7**. These elements are assembled to form efficient host molecules which may typically be shaped as a pair of scissors (e.g. **8**), a roof (e.g. **9**), a dumb-bell (e.g. **3**) or a propeller, as schematically illustrated in **Figure 1.8**.

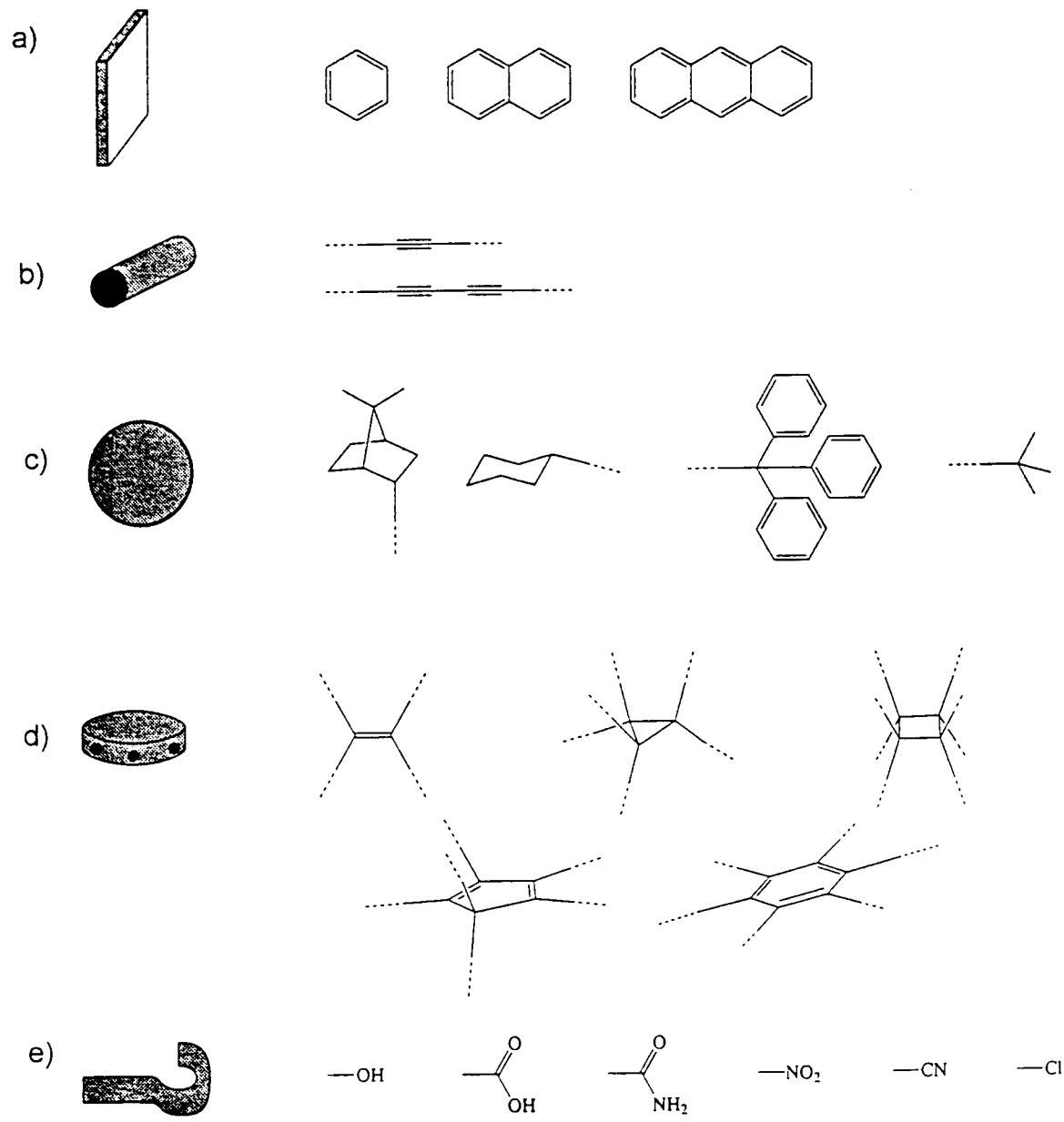

Figure 1.7 Structural building elements: a) planes, b) rods, c) bridged elements and spacious units, d) branching core modules and e) anchor groups[23].

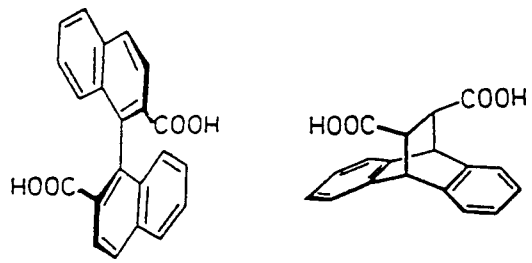

8 **9**

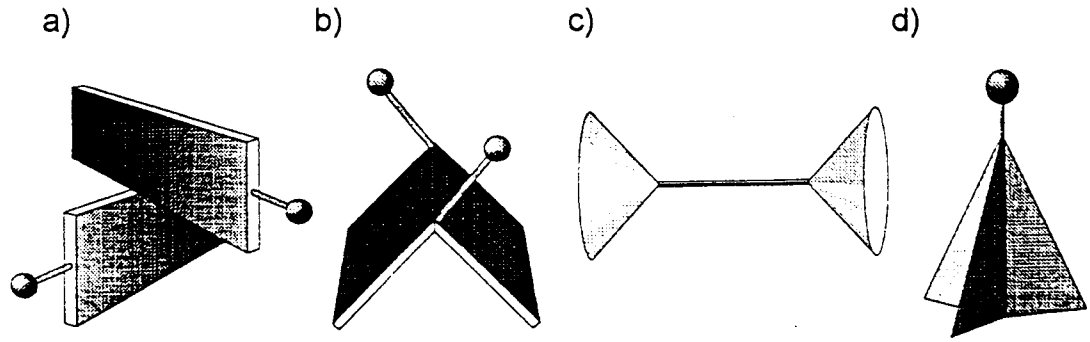

Figure 1.8 The typical overall shapes of the host molecules in host design: (a) scissors, (b) a roof, (c) a dumb-bell and (d) a propeller. The shaded balls represent functional group[23].

1.3. Diol host compounds

Based on the above principles, diol derivatives, which have a rigid molecule with an anti-diol function and sterically bulky groups (e.g. hydrophobic groups such as phenyl) may turn out to be good hosts. Toda[26], Weber[27] and Bishop[28] have specifically designed and synthesised diverse diol host compounds and found they have high inclusion affinity for a wide variety of organic solvent molecules, mostly due to the formation of hydrogen bonding between the host and guest. A few examples of diol host compounds are represented in **Figure 1.9**.

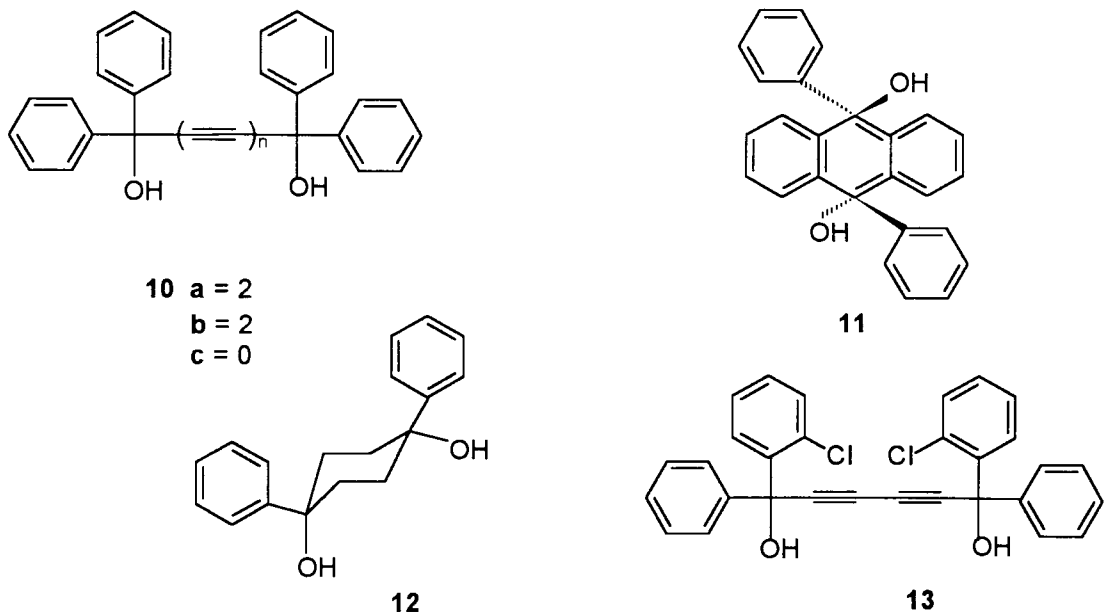

Figure 1.9 A few examples of the diol host compounds.

Toda, who synthesised the hosts (**10a**, **b** and **c**), found that larger substituents and longer alkyne linkage increased the inclusion capability of these related hosts[29]. The rigidity of the linkage of these host compounds is also important in the formation of a stable crystalline lattice. Following these findings, the simplified host, *trans*-9,10-dihydroxy-9,10-diphenyl-9,10-dihydroanthracene, (**11**) was developed. It is a very effective host compound for the inclusion of a wide range of aliphatic and aromatic guest substances[30,31,32]. However, the host (**11**) did not include alcohols, except methanol and ethanol, while in contrast, the rather simplified host (**12**), with *cis*- conformation, tended to include various kinds of alcohols. X-ray structural analysis of a 1:2 inclusion crystal of (**11**) and methanol showed that a four-membered ring is formed via hydrogen bonding, as schematically depicted in **Figure 1.10**, while the host (**12**) includes alcohol via a linear hydrogen bond chain as depicted schematically in **Figure 1.11**. Due to steric limitations, alcohols which are bulkier than ethanol cannot form the four-membered ring, while sterically bulky alcohols can still be accommodated by (**12**). This implies that, beside the consideration of shape and symmetry, it is also important to identify hydrogen bonding motifs or other intermolecular interactions which will dominate in the supramolecular design of new inclusion systems[28].

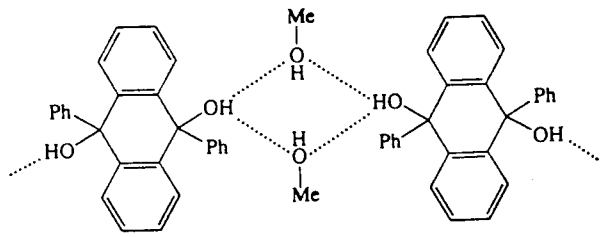

Figure 1.10 Structure of a 1:2 inclusion complex of (**11**) and methanol[32].

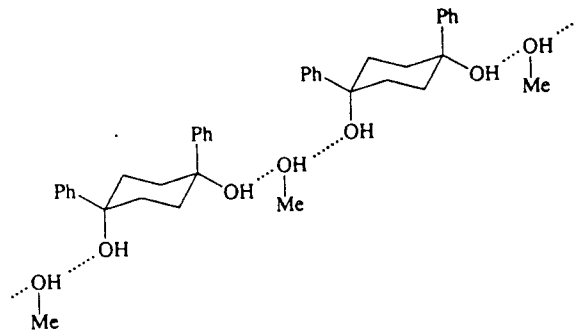

Figure 1.11 Structure of a 1:1 inclusion compound of (**12**) and methanol[32].

1.4. Applications of inclusion phenomena

Inclusion compounds are not only of theoretical interest, but have also found numerous practical applications. In 1990 Vögtle[16] summarised the following applications utilising inclusion crystallisation:

— Separation of mixtures(isomers, homologues)

— Separation of racemates

— 'Solidification' of gases and liquids

— Stabilisation of sensitive or toxic substances

— Polymerisation inside inclusion voids (topochemistry)

— Battery systems and organic conductors

For example, some of the achiral diol hosts mentioned above can be used to separate close isomers. The host (**10a**) was found to be effective for the separation of *o*- and *p*-isomers of di-substituted benzenes, e.g. methylbenzaldehyde. Interestingly, in most cases, the *p*-isomers were preferentially included. Chiral diol hosts are also very useful and have been

used to resolve guest substances into enantiomers. Toda used the chiral host ((+)**13**), derived from (**10a**), to successfully separate numerous guests into enantiomers, e.g. cyclic ketone and lactones which constitute important synthetic building blocks[26]. In Pharmacology, the well known inclusion compounds of cyclodextrins have been used to protect drugs from auto-oxidation or decomposition, or to effect rapid resorption by the body; in addition, their properties as 'artificial enzymes' have received much attention[16].

In addition of above list, many other possible applications have been suggested recently[33]. Of particular interest, the inclusion selectivities and reversible inclusion process have been explored for the development of chemical sensors[34]. The basis of this application was laid by Sauerbrey[35] with his work on oscillating quartz crystals and first successfully applied by King[36] as a hydrocarbon detector with a detection limit of 1 ppm for xylene. Ehelm, Wimmer and Weber[37] have coated a quartz oscillator with diol hosts (**14** or **15**) in a quartz microbalance system (QMB) and detected a change in frequency of the oscillator as the host included organic solvent vapours, thus gaining mass. A linear relationship exists between the change in frequency and the change in mass[35]. These techniques have possible applications for medical, industrial or environmental purposes, for example, detecting trace amounts of odorant[38], warning and safety systems and investigating environmental pollution.

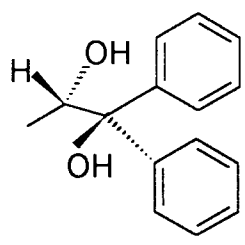

14

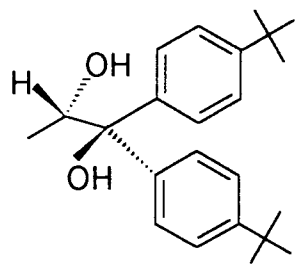

15

1.5. Physical chemistry of inclusion compounds

Crystal structures, thermodynamic and kinetic stability and selectivity of solid state inclusion compounds have been reviewed recently[39,40]. The standard techniques which are usually employed in the measurement of physico-chemical properties of inclusion compounds are summarised in **Figure 1.12**. X-ray diffraction is used to characterise the crystalline inclusion compounds and determine their crystal structures. Many of their physico-chemical properties can be interpreted in terms of their molecular structures. In particular, the strengths of the intermolecular interactions and the topology of the host-guest assembly allow us to explain such properties as their thermal stabilities, kinetics of formation and the mechanism accompanying their decomposition. Thermal analysis, such as thermogravimetric analysis (TG) and differential scanning calorimetry (DSC), has been used to establish the relative stabilities of different inclusion compounds[39]. Molecular mechanics allow us to calculate lattice energy, in order to correlate it with the measured physico-chemical quantities. Kinetics of formation or decomposition can be studied using various techniques. For solid-solid reactions, X-ray powder diffraction, solid-state UV spectroscopy, solid state NMR, *etc.* may be employed to investigate the kinetics; for solid-gas reactions, TG is the most convenient technique to study the kinetics of decomposition by isothermal or non-isothermal methods[41].

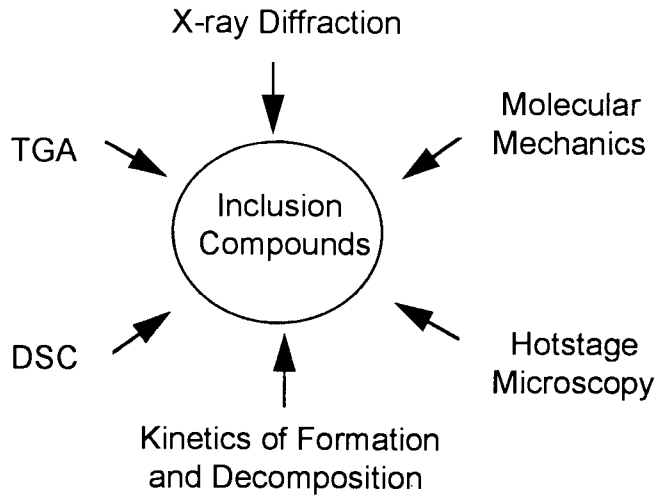

Figure 1.12 Techniques employed to study inclusion compounds[40].

1.6. About this study

Cyclohexanone and its methyl derivatives are important starting materials in organic synthesis. Cyclohexanone (b. p. = 155°C) and its mono methyl isomers (boiling range of 164-172°C) have similar physical properties. One of the aims of this study is to separate these compounds by selective inclusion by the intensively studied host, *trans*-9,10-dihydroxy-9,10-diphenyl-9,10-dihydroanthracene (DDDA) (**11**).

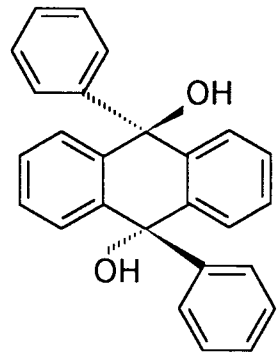

The host DDDA has proved to form stable inclusion compounds with various hydrogen bonding acceptors[32]. Since all four guest compounds, listed in **Table 1.1**, possess a ketyl-functionality, this host was chosen. The thermal stabilities of these inclusion compounds were studied and compared. Attempts were also made to relate the kinetics of decomposition of these compounds with their crystal structures. The crystal structures of the inclusion compounds between DDDA and cyclohexanone (**DACH**) and 3-methylcyclohexanone (**DA3M**) were elucidated. The crystal structures of inclusion compounds between DDDA and 2-methylcyclohexanone (**DA2M**) and 4-methylcyclohexanone (**DA4M**) have been previously elucidated by Bond *et al*[31]. Their host-guest assemblies in the crystal packing were reanalysed and compared with the other two inclusion compounds.

Table 1.1 The code names of the guest compounds and the inclusion compounds between the guests and the host DDDA in this study.

Guest compounds	Code names of guests	Code names of inclusion compounds
Cyclohexanone 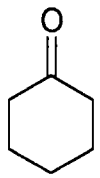	**G1**	**DACH**
2-methylcyclohexanone 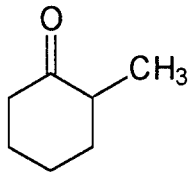	**G2**	**DA2M**
3-methylcyclohexanone 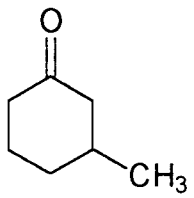	**G3**	**DA3M**
4-methylcyclohexanone 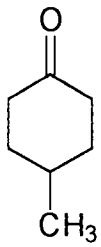	**G4**	**DA4M**

References

1. J. -M. Lehn, *Angew. Chem.*, Int. Ed. Engl. (Nobel Lecture), 27, 1988, p89.
2 G. R. Desiraju, in 'Comprehensive Supramolecular Chemistry', Vol 6, 'Solid-state Supramolecular Chemistry: Crystal Engineering', D. D. MacNicol, F. Toda and R. Bishop (Volume editors), Pergamon Press, 1996.
3 Y. Aoyama, in 'Supramolecular Chemistry', V. Balzani and L. de Cola, Kluwer (eds.), Dordrecht, 1992, p27.
4 C. B. Aakeröy and K. R. Seddon, *Chem. Soc. Rev.*, 1993, p397.
5 J. E. D. Davies, W Kemula, H. M. Powell and N. O. Smith, *J. Incl. Phenom.* 1, 1983, p3.
6 H. Davy, *Philos. Trans. R. Soc. Lond.*, 101, 1811, p155.
7 C. Schafhäutl, *J. Prakt. Chem.*, 21, 1841, p129.
8 F. Vögtle, in 'Supramolecular Chemistry', John Wiley & Sons, Chichester, 1991, reference 7-9.
9 K. A. Hoffmann and F. A. Küspert, *Z. Anorg. Allg. Chem.*, 15, 1897, p204.
10 A. P. Dianin, *J. Soc, Phys. Chem. Russe.*, 46, 1914, p1310.
11 A. Villiers, *C. R. Hebd. Sceances Acad. Sci.*, 112, 1891, p536.
12 J. Wieland and H. Sorge, *Z. Physiol. Chem. Hoppe-Seyler's.*, 97, 1916, p1.
13 E. Terres and W. Vollmer, *Z. Petroleum*, 31, 1935, p1.
14 M. F. Bengen, *German Patent Application OZ 123438*, March 18, 1940.
15 C. J. Pederson, *J. Am. Chem. Soc.*, 89, 1967, p2495.
16 F. Vögtle, 'Supramolecular Chemistry', John Wiley & sons, Chichester, 1991.
17 E. Weber, *Top. Curr. Chem.*, 140, 1987, p17.
18 E. Weber and F. Vögtle, in 'Comprehensive Supramolecular Chemistry', Vol 2, 'Molecular Recongnition: Receptors For Molecular

Guests', F. Vögtle (Volume editors), Pergamon Press, 1996, Chap.1, p13.

19 D. D. MacNicol, in 'Inclusion Compounds' Vol 2, Atwood, Davies and MacNicol (eds.), Academic Press, London, 1984, Chap.1, p1.

20 E. Weber, in 'Comprehensive Supramolecular Chemistry', Vol 6, 'Solid-state Supramolecular Chemistry: Crystal Engineering', D. D. MacNicol, F. Toda and R. Bishop (Volume editors), Pergamon Press, 1996, Chap.17, reference 6-10.

21 A. D. Hardy, J. J. McKendrick, D. D. MacNicol, *J. Chem. Soc.*, Perkin Trans 2, 1979, p1072.

22 J. L. Atwood, J. E. D. Davies, D. D. MacNicol (eds) 'Inclusion Compounds' Vol1 1-3, Acadamic Press, London, 1984; Vols 4 and 5, Oxford University Press, Oxford, New York, 1991.

23 E. Weber, in 'Comprehensive Supramolecular Chemistry', Vol 6, 'Solid-state Supramolecular Chemistry: Crystal Engineering', D. D. MacNicol, F. Toda and R. Bishop (Volume editors), Pergamon Press, 1996, Chap. 17.

24 D. D. MacNicol and G. R. Downing, in 'Comprehensive Supramolecular Chemistry', Vol 6, 'Solid-state Supramolecular Chemistry: Crystal Engineering', D. D. MacNicol, F. Toda and R. Bishop (Volume editors), Pergamon Press, 1996, Chap. 14.

25 D. D. MacNicol and D. R. Wilson, *J. Chem. Soc. Chem. Commun.*, 1976, p494; A. D. U. Hardy, D. D. MacNicol and D. R. Wilson, J. Chem. Soc. Perkin Trans. 2, 1979, p1011.

26 F. Toda, K. Tanaka, G. Ulibarri Daumas and C. Sanchez, *Chem. Lett.* 1983, p1521.

27 E. Weber, N. Dõrpinghaus, C. Wimmer, Z. Stein, H. Krupitsky and I. Goldberg, *J. Org. Chem.*, 57, 1992, p6825.

28 R. Bishop, in 'Comprehensive Supramolecular Chemistry', Vol 6, 'Solid-state Supramolecular Chemistry: Crystal Engineering', D. D. MacNicol, F. Toda and R. Bishop (Volume editors), Pergamon Press, 1996, Chap. 4.

29 F. Toda, in 'Inclusion Compounds', J. L. Atwood, J. E. D. Davies and D. D. MacNicol (eds.), Vol 4, Oxford University Press, London (1991), p126.

30 F. Toda, K. Tanaka and T. C. W. Mak, *Tetrahedron Lett.* 25, 1984, p1359; *J. Inclu. Phen.* 3, 1985, p225.

31 D. R. Bond, L. R. Nassimbeni and F. Toda, *J. Crystallogr. Spectrosc.Res.*, 19, 1989. p847.

32 F. Toda, in 'Comprehensive Supramolecular Chemistry', Vol 6, 'Solid-state Supramolecular Chemistry: Crystal Engineering', D. D. MacNicol, F. Toda and R. Bishop (Volume editors), Pergamon Press, 1996, Chap. 15.

33 'Comprehensive Supramolecular Chemistry', Vol 10, 'Supramolecular Technology', D. N. Reinhoudt (Volume editors), Pergamon Press, 1996.

34 F. C. J. M. Van Veggel, in 'Comprehensive Supramolecular Chemistry', Vol 10, 'Supramolecular Technology', D. N. Reinhoudt (Volume editors), Pergamon Press, 1996, Chap.7.

35 (a) G. Z. Sauerbrey, *Phys. Verha.*, 8, 1957, p113. (b) G. Z. Sauerbery, *Z. Phys.*, 155, 1959, p206.

36 W. H. King, Jr., *Anal. Chem.*, 36, 1964, p1375.

37 A. Ehlem, C. Wimmer, E. Weber and J. Bargon, *Angew. Chem. Int. Ed. Engl.*, 32, 1993, p110.

38 J. Emsley, *New Scientist*, 11 March 1995, p21.

39 L. R. Nassimbeni, in 'Crystallography of Supramolecular Compounds', p285, Kluwer Academic Publishers, 1996.

40 M. R. Caira and L. R. Nassimbeni, in 'Comprehensive Supramolecular Chemistry', Vol 6, 'Solid-state Supramolecular Chemistry: Crystal Engineering', D. D. MacNicol, F. Toda and R. Bishop (Volume editors), Pergamon Press, 1996, Chap 25.

41 M. E. Brown, 'Introduction to Thermal Analysis - Techniques and Applications', Chapman and Hall, London, 1988.

CHAPTER 2

EXPERIMENTAL

2. EXPERIMENTAL

2.1. Host compound

The host compound *trans*-9,10-dihydroxy-9,10-diphenyl-9,10-dihydroanthracene (DDDA), $C_{26}H_{20}O_2$, was synthesised by Dr. Huijie Wan, according to the method of Ingold and Marshall[1]. The Grignard reaction was carried out using anthraquinone as starting material. The Grignard reagent was prepared from phenylbromide.

The resulting light-yellow raw product was recrystallised from acetone several times until the solution was colourless. The crystals obtained were dried under vacuum at 60°C for 3 hours in order to remove the solvent. The melting point of the white crystalline powder product was measured on a Linkam TH600 microscope, and was observed in the temperature range of 269-270°C. The DSC experiment showed a sharp endothermic peak at an onset temperature of 261°C due to melting. From the report in literature[1], the m.p. of pure DDDA is 260-261°C. The temperatures at which the changes were observed on the Hotstage were often higher than those measured in the thermal analysis of the samples. This is mainly due to the difference in geometry of the Hotstage and DSC apparatus. The purity of the product was confirmed using microanalysis. The results of which was as follows:

Calculated for $C_{26}H_{20}O_2$: C 85.69% H 5.53%

Observed for the product: C 85.44% H 5.60%

Based on these results, the product was accepted since its percentage composition differed by no more than 0.4% from the theoretical values.

2.2. Guest compounds

All the liquid guests were bought from Aldrich Chemical and used as received. The guests **G2** and **G3** are used as racemic mixtures.

2.3. Preliminary characterisation

2.3.1. X-ray powder diffraction (XRD)

XRD experiments were carried out using a Philips vertical goniometer PW1050/80 with a Philips PW1394 motor control and PW1390 channel control. The X-rays were generated by a Philips PW1130/90 model operating at 40 kV and 20 mA. Using Nickel-filtered copper radiation (CuKα, λ = 1.5418Å), the powder patterns were collected over a 2θ range of 6-40°. The powder samples were packed in an aluminium holder and step scans were recorded at 0.1° 2θ intervals and 1 second counts, unless otherwise specified in the text. Automatic receiving and divergence slits were used.

2.3.2. Powder samples and particle sizing

Powder samples of the inclusion compounds were prepared by different methods as described below. The samples were subjected to a particle size analysis, in which the particles are classified according to their size in a number of size ranges and the fraction of sample in each range is determined. The particle size distributions were measured using a Malvern Series 2600 laser particle sizer. A suspension of the sample under investigation was made in water. Since the host compound is hydrophobic and tends to coagulate, it often gives rise to a shoulder in the particle size distribution curve, as shown typically in **Figure 2.1**. The suspensions were placed in an ultrasonic bath for 1 minute before particle sizing, in order to minimise the occurrence of this phenomenon.

Method 1. The host compound was ground into a fine powder in an agate mortar. The sample was placed on the balance pan of a levitating balance (LB) and subsequently exposed to the vapour of the guest compound. This method yielded sample A with particle diameters in the range of 10 to 100μm, having a mean particle size of approximately 70μm.

Method 2. The host compound was dissolved in the guest solvent. The inclusion complex powder was obtained by evaporation of a continuously stirred solution at room temperature. This yielded sample B particles with a diameter range of 10 to 100μm, having a mean particle size of 50μm. Samples obtained from different guest solvents yielded particle size distributions in the same range.

Method 3. Method 2 was used, but the solvent was changed to acetone. After being dried properly to remove the acetone, the host powder was then used on the LB to absorb the targeted guest vapour. This yielded sample C . A mean particle size of approximately 50μm with a spread range of 10 to 100μm was obtained, which is the same as that obtained by method 2.

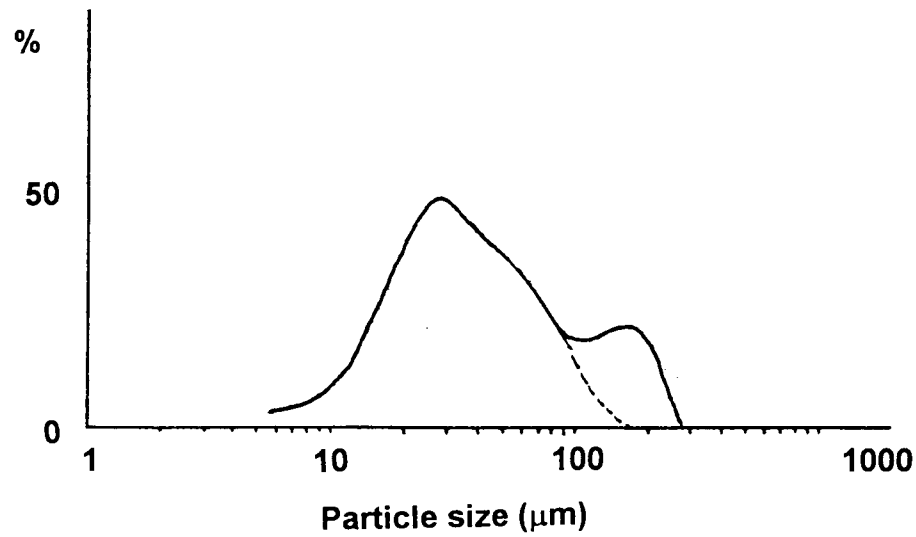

Figure 2.1 An approximately log-normal distribution of particle size for sample C. The shoulder, which arise from particle coagulation was ignored in the analysis of the mean value.

2.4. Thermal analysis

2.4.1. Hotstage microscopy (HSM)

HSM is used as a visual method to observe the thermal events of samples during the heating process. The crystals of the inclusion compounds were subjected to heating on a Linkam TH600 hot stage mounted on a Nikon SMZ-

10 microscope, on which a Nikon FX-35 camera was mounted for simultaneous photography. The temperature was controlled by a Linkam TP92 temperature controller and can be raised manually at a linear rate.

2.4.2. Thermogravimetric analysis (TG)

TG measures the weight loss of a sample as a function of temperature or time and is used to establish the stiochiometry of the inclusion compounds as well as kinetic parameters.

TG was performed on a Perkin Elmer PC series 7 system. Sample weights were typically between 2 and 8 mg. The samples were held in a open platinum pan and continuously purged by a stream of dry nitrogen gas at a flow rate of 40 mL/min. The TG analyser was regularly calibrated using built-in procedures for furnace and weight calibration. A two-point standard temperature calibration was performed by measuring the Curie points of Alumel (163°C) and Nickel (354°C).

The programmed TG analyses were typically carried out over a temperature range of 30°C to 300°C, at a predetermined linear heating rate of 10°C/min. This technique was primarily used to determine the host-guest ratio of the inclusion compounds from the percentage weight loss.

The isothermal TG was employed for kinetic studies, and will be described in section 2.5.3.

2.4.3. Differential scanning calorimeter (DSC)

DSC was used to measure the enthalpy changes associated with the desolvation, phase transformations, melting and other thermal events of the inclusion complexes during heating.

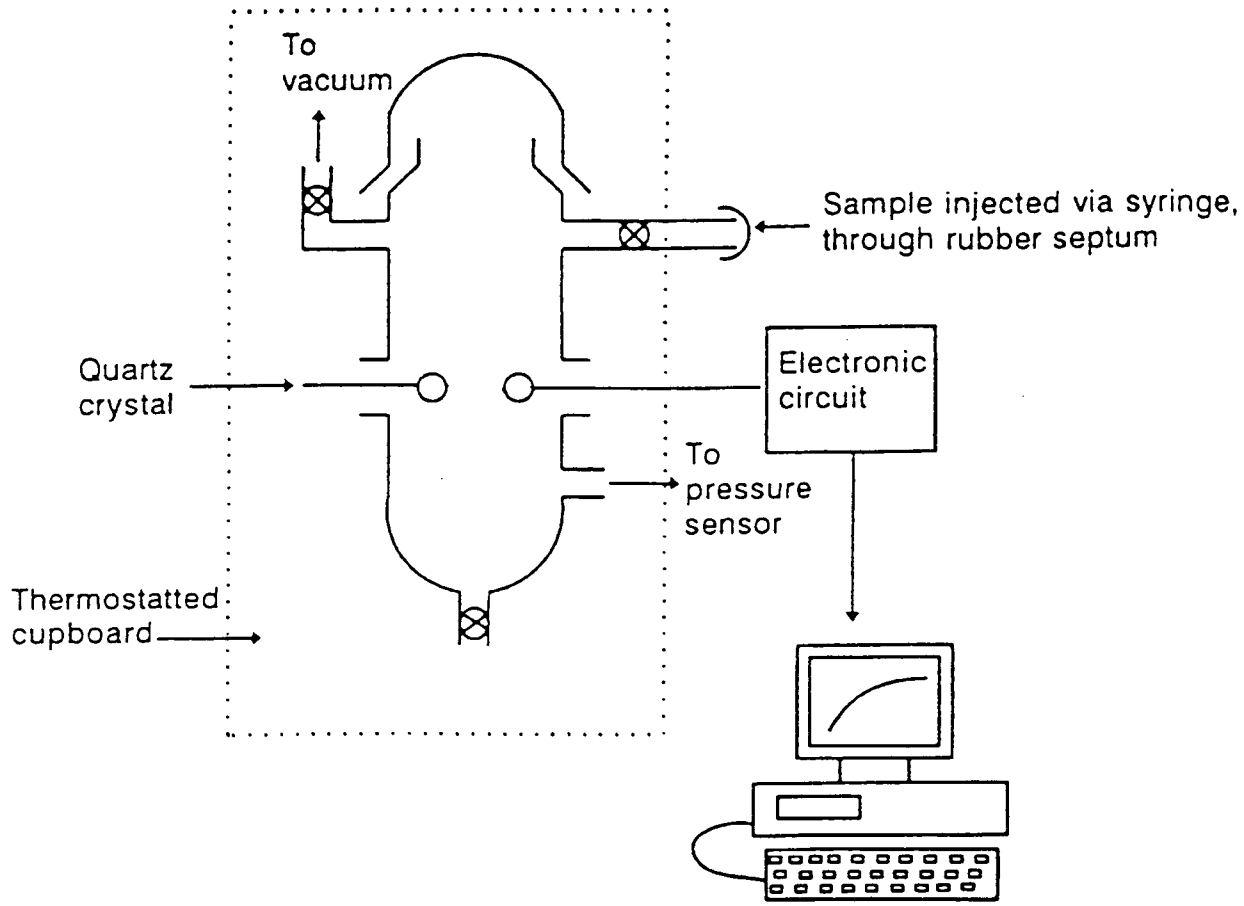

Figure 2.2 Schematic diagram showing the principle features of the QMB system[4].

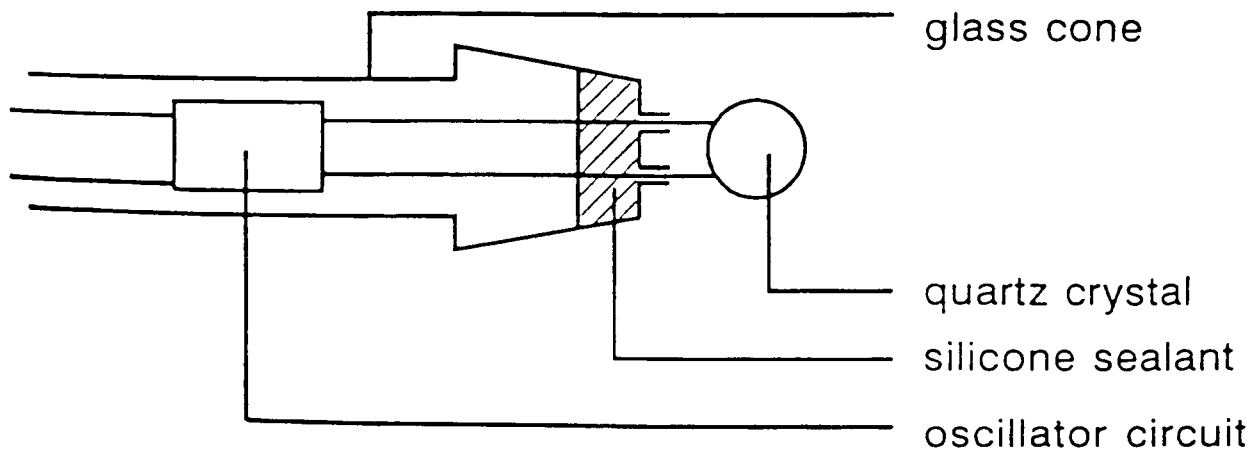

Figure 2.3 Schematic diagram of the quartz crystal probe[4].

2.5.1.2. Experimental procedure

The quartz crystal was coated with the host compound DDDA by dipping it into a concentrated solution of DDDA in diethyl ether. Upon evaporation of the solvent, a coating of the complex of DDDA with diethyl ether remained on the

surface of the quartz crystal. A sufficiently uniform coating (200-400μg) was obtained by repeating this procedure several times. Then the quartz crystal was left in a dust-free atmosphere overnight. This is done so that the DDDA-diethyl ether inclusion complex can desolvate slowly. Using this method, the non-porous α-phase host particles are evenly sized, lath shaped, uniformly spread over the surface and possess random orientation[4]. These particles were found to be < 20 μm in any dimension, using scanning electron microscopy[5].

In the reaction cell, the quartz crystal in one probe was left uncoated to monitor the response due to change in temperature and vapour pressure, and the other two were coated with known amounts of DDDA.

The reaction cell was evacuated to a pressure of less than 1 mmHg and then isolated under thermal conditions. A volume of 10-1000μL targeted solvent was injected using a microsyringe via the rubber septum. The vapour pressure can be controlled by the volume of the injected solvent based on its volatility. The solvent sample vaporised immediately and yielded a constant pressure in 10 seconds. After the guest uptake reaction reached completion, the reaction vessel was pumped down to vacuum until the guest was released from the inclusion compound and the frequency reading returned to the starting value. A series of Δf versus time curves were thus obtained at various fixed temperatures.

It is imperative for the coated crystal to be conditioned prior to kinetic studies, by repeating sorption-desorption cycles, until the rate of reaction remains constant. It was found by Coetzee *et al* [4], that the particle size of the host compound decreases with repeated cycles of sorption-desorption, resulting in an increase in the rate of reaction. The particle size and hence rate of reaction remained constant after 5 cycles.

Data obtained from these experiments were reduced to extent of reaction (α)

versus time curves, which were fitted to various kinetic models in order to find an appropriate mechanistic model. These results will be discussed in detail in Chapter 3.

The major advantage of this QMB system for kinetic studies is that it can be carried out on very small amount of host sample and it is ideal for preliminary investigation. On the other hand, the disadvantage is that there is not adequate sample to carry out X-ray powder diffraction, or other bulk analytical experiments, to verify the formation of the inclusion compound.

2.5.2. Levitating balance (LB)

In order to study bulk samples, the formation and decomposition of the inclusion compounds were also measured on a levitating balance (LB). It directly measures the mass change in the reaction of solid host with guest vapour under conditions of controlled temperature. The LB apparatus is illustrated in **Figure 2.4** and described in detail by Barbour *et al.*[6]

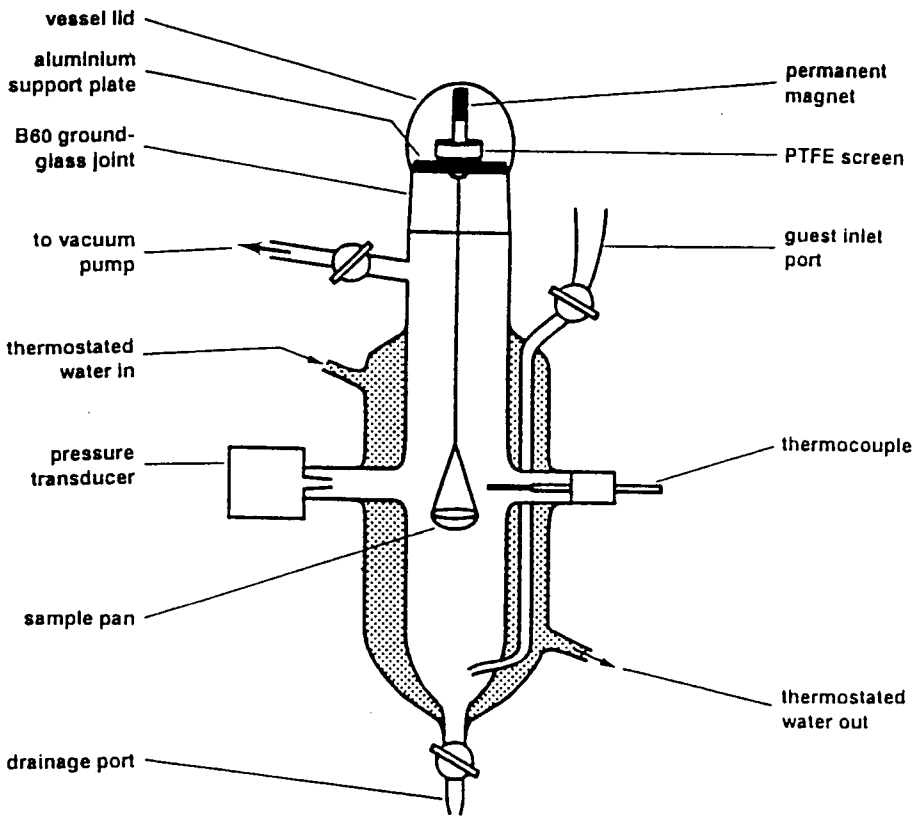

Figure 2.4 The LB system for measurement of the kinetics of gas-solid reactions[6].

The sample pan is held suspended in the reaction vessel by means of a permanent magnet coupled to an electromagnet attached to the balance. The temperature and pressure can be measured via a thermocouple and pressure transducer within the reaction chamber.

A powder sample of known particle-size, and of known mass (200-400 mg), was held in the pan in the reaction vessel. An excess of the appropriate liquid guest was introduced into the reaction vessel, which is maintained at reduced pressure. The liquid sample vaporised upon injection and an excess was reserved in the base of the vessel to ensure constant guest vapour pressure during the sorption reaction. The mass change due to guest uptake was recorded with time, and a Δm versus time curve displayed on the microcomputer.

When the mass reading reached the calculated stoichiometry and remained stable for a while, the guest uptake was complete. The inclusion complex was either removed from the reaction cell to be analysed by means of TG and X-ray powder diffraction, or, was left in the reaction vessel in order to carry out the guest desorption reaction through continuous pumping.

One of the advantages of the LB for investigating the reaction of solid hosts with guest vapours, is that it supplies sufficient samples for other analytical experiments. We can also use the LB to confirm the QMB results, since the LB measures mass change directly. But the vaporisation of a large amount of guest within a very short time period lead to an internal temperature change of 1-2°C before reaching equilibrium. This effect introduced uncertainty into the kinetic measurements. The measurements carried out on this system were not truly isothermal, but rather each reaction occurred within a 1-2 degree centigrade temperature window.

DSC measurements were performed using a Perkin Elmer series 7 DSC. There are two identical, crimped and vented aluminium pans, one of which is empty and used as the reference. In power-compensated DSC the temperature of the sample and the reference are kept the same by supplying energy to them. The difference in the energy supplied is then plotted against temperature. Endothermic reactions within the sample result in more energy being supplied to the sample and are plotted as positive peaks. Exothermic reactions are represented by negative peaks. The instrument was calibrated using standard materials, i.e. Indium (ΔH = 28.5J/g, m.p. = 156.6°C) or Zinc (ΔH = 102.1J/g, m.p. = 419.5°C)[2].

The fine powder samples ranging in mass between 2 and 8 mg were placed in the crimped, vented aluminium pan with a lid and heated at a predetermined linear rate of 10°C/min from 30°C to 300°C, with a stream of dry nitrogen purge gas at a flow rate of 40 mL/min.

2.5. The Systems for kinetic studies

2.5.1. Quartz microbalance (QMB)

2.5.1.1. Description of the QMB apparatus

The QMB is based on the mass-frequency dependence of an AT-cut oscillating quartz crystal according to the formula derived by Sauerbrey[3]:

$$\Delta f = -k f_o^2 \Delta m$$

where Δf is the frequency change, k is a constant related to each specific crystal, f_o is the unperturbed resonant frequency, and Δm is the mass change.

Such an oscillating crystal can be turned into a quartzmicrobalance (QMB), able to detect small amounts of volatile organic solvents, by coating the crystal with a suitable host compound. When the host is exposed to the guest vapour, the following reaction takes place:

$$H(s,\alpha) + nG(g) \Leftrightarrow H \cdot G_n(s,\beta)$$

The non-porous phase of the host alone is labelled as the α phase. The host molecules rearranged themselves in order to accommodate the guest molecules, and so form a new, β phase, which is the structure of the inclusion compounds. The frequency of oscillation decreases with increasing mass, hence it can be employed to measure the mass change during the reaction, therefore kinetics of inclusion or decomposition can be measured for very small amounts of host samples.

The QMB apparatus is shown in **Figure 2.2**. It consists of a glass cell which can be evacuated and whose internal pressure can be measured, using a pressure transducer. The whole cell is placed in a thermostatic cupboard whose internal temperature is controlled within 0.1°C by a PID controller.

On the cell, there are an inlet for the guest liquid to be injected via a rubber septum, three connectors for the quartz crystal probes to be inserted, and a port for the pressure transducer.

Each probe, shown in **Figure 2.3**, comprised a 5 MHz quartz crystal mounted in a socket on a glass cone, with a crystal oscillator circuit secured inside the cone. The probes are all well sealed with silicone sealant, to prevent leaks to the atmosphere.

The electronic circuit monitors the change in frequency of a given crystal and the signal is fed to a microcomputer which displays the change in frequency against time. The data is written to a file, which can be imported into a spreadsheet programme and manipulated in order to obtain extent of reaction (α) versus time curves, for the kinetic studies.

2.5.3. Isothermal TG

Isothermal TG was performed using the same Perkin Elmer PC series 7 system as the programmed TG (see section 2.4.2). A series of isothermal TG experiments were carried out at selected temperatures with given constant particle size powder samples. The samples were rapidly heated to the selected temperature, which was then maintained until guest desorption was complete. The experiments were repeated at a series of different temperatures, which were chosen so that the total reaction time ranged from 0.5 to 18 hours and were usually lower than the onset temperature for the guest release, obtained from the programmed TG experiments.

In addition, a large crystal of inclusion compound **DACH** was investigated on the isothermal TG under condition of no nitrogen purge gas. The results are discussed in Chapter 3.

2.6. Competition experiments

In order to study the selectivity and tendency of the host to include various isomers of a compound, a series of competition experiments were set up, and the analysis was carried out using Gas Chromatography.

2.6.1. Crystallisation

A series of vials were made up with mixtures of the liquid guests with varying mole fractions. For a given amount of host (DDDA), guests volumes were chosen so that an excess of the guest of lower mole fraction was always maintained. The host:guests mole ratio at 1:20 in each vial was chosen. After the guest mixture was calibrated by gas chromatography to determine the guests ratios, the host DDDA was added, and heated in order to dissolve all host. Through slow cooling in a waterbath to room temperature, crystals were obtained. During the experimental process, the vials were always covered and

sealed to prevent significant evaporation.

The crystals of the inclusion complexes formed were removed from the mother liquor solutions and blotted dry on filter paper, then placed in air tight glass vials with silicone seals incorporated into the screw-on lids. The vials were heated to 200°C, on a hot plate to induce complete desorption of the guests. The guests vapour condensed on the cool walls of the vials and formed drops, which were extracted and used for gas chromatography.

2.6.2. Gas chromatography (GC)

For the analyses involving a mixtures of guest cyclohexanone (**G1**) with any one of the other three guests, 2-methyl cyclohexanone (**G2**), 3-methyl cyclohexanone (**G3**), and 4-methyl cyclohexanone (**G4**), a Philips PYE Unicam Series 304 Chromatography equipped with a 10% OV101 on Chromosorp Packing Column (1m) was chosen. This instrument was linked to a Waters 746 Data Module integrator. The operating conditions were as follows:

Sample: 10 μL of mixture diluting in 300 μL of chloroform

Injection volume: 1.5 μL

Injector: 180°C

Detector: Flame Ionisation Detector, 250°C

Carrier gas and flow rate: Hydrogen, 10 mL/min

Column temperature programme: From 60°C to 140°C at a heating rate of 10°C/min

For the analyses involving the guests mixtures of **G2** and **G4**, or **G3** and **G4**, a Carlo Erba Fractovap 4200 instrument equipped with a Supelcowax Fused Silica Capillary Column (30 m, 0.20 mm LD, 0.20 μm film thickness), linked with a Spectra-Physics SP4290 integrator, was used. The experimental conditions were as follows:

Sample: 10 μL of mixture diluting in 300 μL of chloroform

Injection volumes: 0.5 μL

Injector: 220°C

Detector: Flame Ionisation Detector, 230°C

Carrier gas: Helium

Carrier gas pressure and splliter flow rate: 1 bar, 200 mL/min (for **G2** and **G4**)
0.5 bar, 150 mL/min (for **G3** and **G4**)

Column Temperature Programme: Keep at initial 50°C for 10 min, then heat up to 100°C at rate of 2°C/min, and keep at 100°C until finish.

The separation of guests **G2** and **G3** was not achieved on the columns available. Due to the close boiling points and polarities of the two components, a single peak appeared.

2.7. Single crystal X-ray diffraction

2.7.1. Crystal growth and preparation

Warm, concentrated solution of the host DDDA in the appropriate guest solvent were prepared. These warm solutions were filtered using a 0.25 μm Teflon Millex-LCR filters in order to remove dust and debris, thereby reducing the number of nucleation sites. The sealed vials containing hot solutions were placed in a waterbath and allowed to cool slowly to room temperature. Single crystals of suitable size (0.3 ×0.5 mm) were selected on their ability to extinguish plane polarised light uniformly. These crystals were mounted in Lindemann capillary tubes of internal diameter 0.3 or 0.5 mm, together with a drop of mother liquor to minimise deterioration of the crystal caused by guest desorption.

2.7.2. Crystal structure analysis

Approximate cell parameters and space group symmetry were established from oscillation and Weissenberg photographs taken on a Stöe camera using nickel filtered Cu-K_α radiation (λ = 1.5418 Å).

Accurate cell parameters were obtained by least-squares analysis of the setting angles of 24 reflections collected on in the θ range of 16-17° and centred on the diffractometer. Intensity data were collected on an Enraf-Nonius CAD4 diffractometer at room temperature with graphite MoK_α radiation (λ = 0.7107 Å) generated by a Philips PW1730 model operating at 20 mA, 50 kV. The ω-2θ scan mode with a final acceptance limit of 20σ at 20°/min and a maximum recording time of 40 seconds was used. The vertical aperture length was fixed at 4 mm, the aperture width at (1.12 + 1.05tanθ)mm and the scan width at (x + 0.35 tanθ, x = 0.80 or 0.85)° in ω. The intensities and orientation of three reference reflections were monitored periodically to check crystal stability and orientation and instrumental stability. Data were corrected for Lorentz-polarisation effects. Absorption corrections were not applied as values of μR_{min} and μR_{max} (where R_{min} and R_{max} are one-half the largest and smallest crystal dimensions respectively) were between 0.0 and 0.1 for all crystal fragments used[7]. Thus the absorption correction factors, A*, were virtually unity for all reflections. Final refinements were based on those reflections that satisfied the condition $I > 2\sigma(I)$.

2.8. Computation

All computation, unless otherwise stated, were performed on a VAX/VMS (version 5.5) computer at the Computer Centre of the University of Cape Town.

The structures of compounds **DACH** and **DA3M** were solved by direct methods using SHELX-86 [8]. Equivalent reflections were merged and those with $I < 2\sigma(I)$ were suppressed. Subsequent refinements by full-matrix least-squares were performed using SHELXL-93 [9], in which structures were refined against F^2. Agreement between observed structure factors (F_0) and calculated structure factors (F_c)s expressed by the residual index, R. Since residual index for refinement against F^2, R_2, is larger than that

for refinement against F, R_1, both the R-index factor based on F (R_1) and that based on F^2 (R_2) will be quoted for comparison.

$$R_1 = \frac{\in \left| |F_o| - |F_c| \right|}{\in |F_o|}, \qquad wR_2 = \left[\frac{\in w\left(F_o^2 - F_c^2\right)^2}{\in w\left(F_o^2\right)^2} \right]$$

Where w is weighting scheme and was refined for each structure:

$$w = \frac{1}{\sigma^2\left(F^2\right)^2 + \left(aP\right)^2 + bP}$$

Molecular and packing diagrams were produced using the IBM PC version of PLUTO[10]. To view the shapes and sizes of the voids in which the guest molecules were situated in the inclusion compound crystal structure, the program MOLMAP[11] was used. After guest molecules are removed from the crystal structure solution, the host molecules were viewed with atoms given their van der Waals radii[12]. Using the program, a series of slices, which are all parallel to any chosen cell face, were presented by cutting the unit cell at selected intervals. This enables one to investigated the three dimensional shape of channels or cavities formed by the host molecules.

X-ray powder diffraction (XRD) patterns were calculated using LAZY PULVERIX[13] on a PC in a DOS environment. The cell parameters, space group symmetry, atomic co-ordinates and thermal parameters were used as input for the program.

References

1. C. K. Ingold and P. G. Marshall, *J. Chem. Soc.,* 2, 1926, p3080.
2. R. C. Weast, M. J. Astle and W. H. Beyer, eds. CRC Handbook of Chemistry and Physics, CRC Press, Inc., Florida, 1985.
3. (a)G. Z. Sauerbrey, *Phys. Verha.*, 8,1957, p113;
   (b) G. Z. Sauerbrey, *Z. Phys.*, 155,1959, p206.
4. A. Coetzee, L. R. Nassimbeni and K. Alcheitner, *Thermochimica Acta* , 298, 1997, p81.
5. A. Coetzee, PhD. Thesis, Chap. 3, University of Cape Town, 1996.
6. L. J. Barbour, K. Achleitner and J. R. Greene, *Thermochimica Acta*, 205,1992, p171.
7. International Tables for Crystallography, Vol. C, A. J. C. Wilson (ed.), Klumer Academic Publishers, Dordrecht, 1992, p523.
8. G. M. Sheldrick, SHELX-86: Crystallographic Computing 3, G. M. Sheldrick, C. Kruger and R. Goddard (eds.), Oxford University Press, 1985.
9. G. M. Sheldrick, SHELXL-93: Programme For Crystal Structure Determination, unpublished work.
10. W. D. S. Motherwell, PLUTO89, Program For Plotting Molecular and Crystal Structures, University of Cambridge, England, 1989.
11. L. J. Barbour, PhD Thesis, University of Cape Town, 1994.
12. A. Gavezotti, *J. Am. Chem.* Soc., 16, 1983, P105.
13. K. Yvon, W. Jeitschko and E. Parthe, *J. Appl. Cryst.*, 10, 1977, p73.

CHAPTER 3

KINETIC STUDIES

3. KINETIC STUDIES

3.1. Introduction

3.1.1. Homogeneous kinetics

For a homogeneous reaction, the rate of reaction is conveniently measured by the decrease in concentration of reactants or the increase in concentration of products at constant temperature and can be expressed as

Rate = kf(concentration of reactants or products)

where k is the rate coefficient which is a function of temperature. The relationship between the rate constant and the absolute temperature

$k = A\, e^{-Ea/RT}$ or $\ln k = -E_a/RT + \ln A$

was first given quantitatively by Arrhenius[1], and is generally referred to as the Arrhenius law. Based on the theory of collisions[2-5], the Arrhenius parameters are defined as follows. E_a is identified as the activation energy which reactant molecules must have in order to react. While A, the pre-exponential factor or frequency factor refers to the number of collisions. The Arrhenius law is one of the most important relationships in chemical kinetics, and one that provides much information as regards to mechanism[5].

3.1.2. General solid state kinetics

For a heterogeneous reaction of the general form

A (s) + nB (g) $\Leftrightarrow$ AB_n (s)

the concept of concentration no longer has the same significance as in the homogeneous reaction, so that the rate of reaction cannot be defined in the same way[6]. Since gas-solid reactions involve gas release or gas uptake, the rate of reaction can be measured by the loss or gain of mass of the sample during reaction. Usually, at time t, the extent of reaction, α, is defined as

$\alpha = \left| \frac{m_t - m_o}{m_f - m_o} \right|$, where m_o is the initial mass of the reactant, m_f is the final mass of the product, and m_t is the mass of the sample at time t. The kinetic analysis of isothermal gas-solid reactions involves attempting to relate the experimentally measured α and t values with values predicted for a limited set of models based on processes of nucleation and growth, diffusion or geometrical progress of the reactant/product interfaces[7]. The expressions derived from these ideal geometrical models can all be written in their integral forms: $f(\alpha) = kt$, at constant T, as summarised in **Table 3.1**[7].

In the general case, the experimental α-time curve under isothermal conditions has the features illustrated in **Figure 3.1**, though, any of these features except the maximum rate may be absent in specific cases[8]. From the typical α-time curve, we can get information about the mechanism of the reaction, which is often complex, as described below[8,9]:

1. Surface adsorption or desorption, yield initial section A,
2. the formation of nuclei, termed the induction period (section B), which is regarded as being terminated by the development of stable nuclei,
3. the growth of such nuclei, perhaps accompanied by further nucleation, extends to the maximum rate of reaction at D, yielding an acceleratory section C,
4. thereafter, due to overlapping of nuclei and consumption of reactant, a deceleratory section E is yielded and continues until completion of reaction, F.

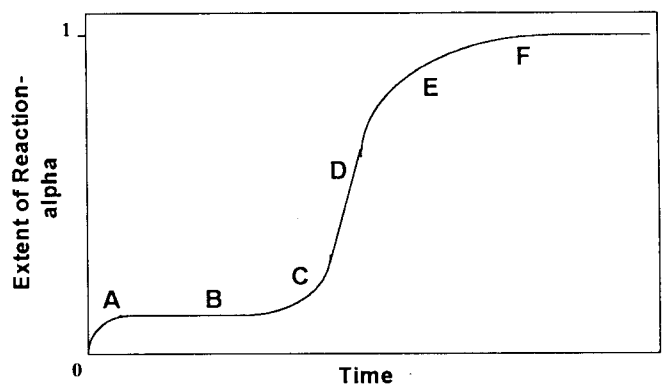

Figure 3.1 The generalised isothermal α-time curve for solid state reaction

It is generally accepted that the nucleation and growth processes play an important role in the decomposition of a solid to yield a second product phase[4,6]. The formation and growth of nuclei is depicted in **Figure 3.2**. The nuclei grow initially from "germ nuclei", which generally occurs at the defects existing in the crystalline reactant. Grains of product phase are formed in the reactant and these increase in size. The reactant/product interface advances and the growth of the product continues until no more reactant is left over.

Table 3.1 Theoretical kinetic models for solid-gas reactions[7]

	$f(\alpha) = kt$
1. Acceleratory α-time curves	
P1 power law	$\alpha^{1/n}$
E1 exponential law	$ln\alpha$
2. Sigmoid α-time curves	
A2 Avrami-Erofe'ev	$[-ln(1-\alpha)]^{1/2}$
A3 Avrami-Erofe'ev	$[-ln(1-\alpha)]^{1/3}$
A4 Avrami-Erofe'ev	$[-ln(1-\alpha)]^{1/4}$
B1 Prout-Tompkins	$ln[\alpha/(1-\alpha)]$
3. Deceleratory α-time curves	
3.1 based on geometrical models	
R2 contracting area	$1-(1-\alpha)^{1/2}$
R3 contracting sphere	$1-(1-\alpha)^{1/3}$
3.2 based on diffusion controlled models	
D1 one-dimensional	α^2
D2 two-dimensional	$(1-\alpha)ln(1-\alpha)+\alpha$
D3 three-dimensional	$[1-(1-\alpha)^{1/3}]^2$
D4 Ginstling-Brounshtein	$(1-2\alpha/3)-(1-\alpha)^{2/3}$
3.3 based on "order of reaction"	
F1 first order	$-ln(1-\alpha)$
F2 second order	$1/(1-\alpha)$
F3 third order	$[1/(1-\alpha)]^2$
Fn n-th order	$[1/(1-\alpha)]^n$

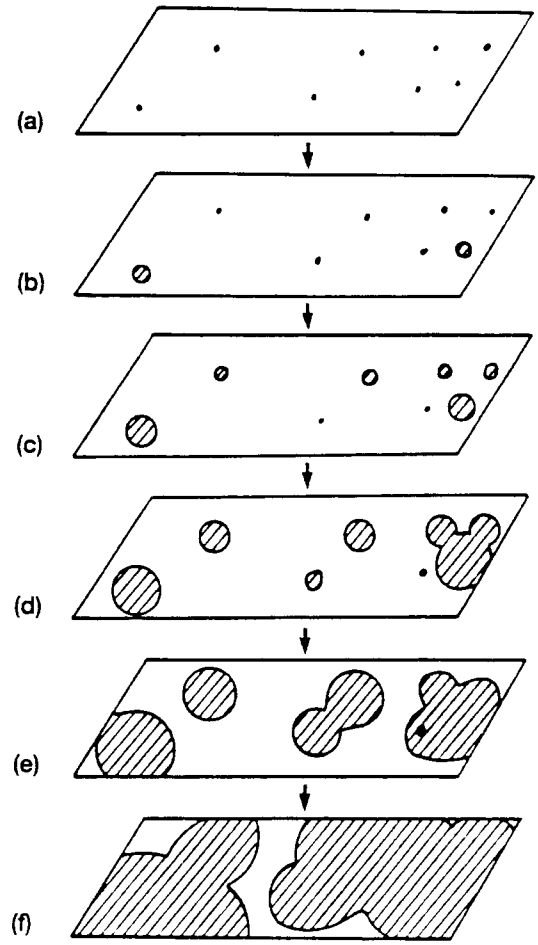

Figure 3.2 Formation and growth of nuclei in solid state decomposition.
a) nuclei site; b) first nuclei formed; c) growth and further nucleation;
d) overlap of nuclei; e)ingestion of nucleation site; d)continue growth[7].

The rate-determining step in most solid phase reactions can be either diffusion, which is the migration of product away from or reactant towards a reaction interface, or chemical reaction which generally occurs at a reaction interface[9]. For diffusion-controlled reactions, based on the assumption that the diffusion coefficient is constant, one-dimensional diffusion on the reaction layer leads to kinetic equation D1, while D2 and D3 are derived from 2 or 3-dimensional diffusion in a cylinder and sphere respectively, and diffusion starting at the exterior of a spherical particle leads to equation D4. For a phase-boundary controlled reaction, which is controlled by movement of an interface at a constant velocity, the rate equations R2 and R3 are then derived simply for a circular disk reacting from the edge inward and for a sphere reacting from the

surface inward respectively. Mainly for analytical convenience[10], the rate equations F1 - Fn based on the order of reaction has been applied to solid state reactions, being analogous to the homogeneous rate laws. The α-time curves for decomposition of solids usually give rise to a sigmoidal shape, and are accounted for by the Prout-Tompkins model (B1) and Avrami-Erofe'ev models (A2 - A4). The Prout-Tompkins model was derived for symmetrically shaped sigmoid-curves based on a chain branching mechanism for nuclei. The Avrami-Erofe'ev equations can be written in the general form[9]:

$$[-ln(1-\alpha)]^{1/n} = kt$$

with the exponent $n = \beta + \lambda$, where β is the number of steps involved in nucleus formation and λ is the number of dimensions in which the nuclei grow.

In application of the rate equations contained in Table 5.1, caution must always be taken in giving geometrical interpretation to the mathematical models. If, for a specific reaction, a given set of (α, t) values obeys a particular kinetic expression, it does not mean that the reaction follows the same mechanism from which that rate equation was derived. The different mechanistic models can lead to the same kinetic equation[7]. The converse is also true[9,11]. Other factors may also reduce the accuracy of interpretation of kinetic data, e.g. particle size effects, reactant pre-treatment or concentration of defects. The reaction rate can be inhomogeneous within the reaction mass, if for example, melting occurs[12]. It is also possible that the mechanism may change during reaction, or vary with the α. In view of these problems, geometric interpretations must be supported by independent evidence, e.g. microscopic observations, measurement of the nuclei.

The variation of the rate constant, k, with temperature is generally assumed to be governed by the Arrhenius equation, $ln\ k = -E_a R/T + ln\ A$, which was originally derived for homogeneous reactions based on well-established theories[1-5]. Being analogous to the homogeneous reaction, the activation energy, E_a, is identified as the energy barrier which must be surmounted during transformation of reactants into products during the rate-limiting step. The

frequency factor, A, was identified as a molecular encounter or as a specific vibration in the reaction co-ordinate[9]. This assignment, as well as the concept of rate constants for solid state reactions have been challenged[11-16]. Some scientists[17-19] prefer to regard both E_a and A as having empirical rather than theoretical significance and refer to them as "apparent kinetic parameters". However, the Arrhenius equation has been successfully applied to numerous reactions involving solids. The Arrhenius parameters do have practical value even though there is still no satisfactory theoretical explanation, as suggested by Brown[7].

3.1.3. Kinetics for organic inclusion compounds

When a suitable host compound is dissolved in a guest solvent or is exposed to a guest vapour, an inclusion compound is formed. The crystal structure of the inclusion compound (β-phase) is different from the non-porous α-phase of pure host. Under certain conditions of temperature and pressure of the guest, the inclusion compound may decompose in several possible ways, as schematically illustrated in **Figure 3.3**.

It may loose all the guest and revert back to the original non-porous α-phase. Alternatively, it may loose only part of the guest and form a metastable intermediate, γ-phase. Thirdly, it may loose all the guest without rearrangement of the host structure, resulting in the retention of the host framework, forming the so-called β_o-phase. Generally, the collapse of the β-phase back to the α-phase is most often encountered.

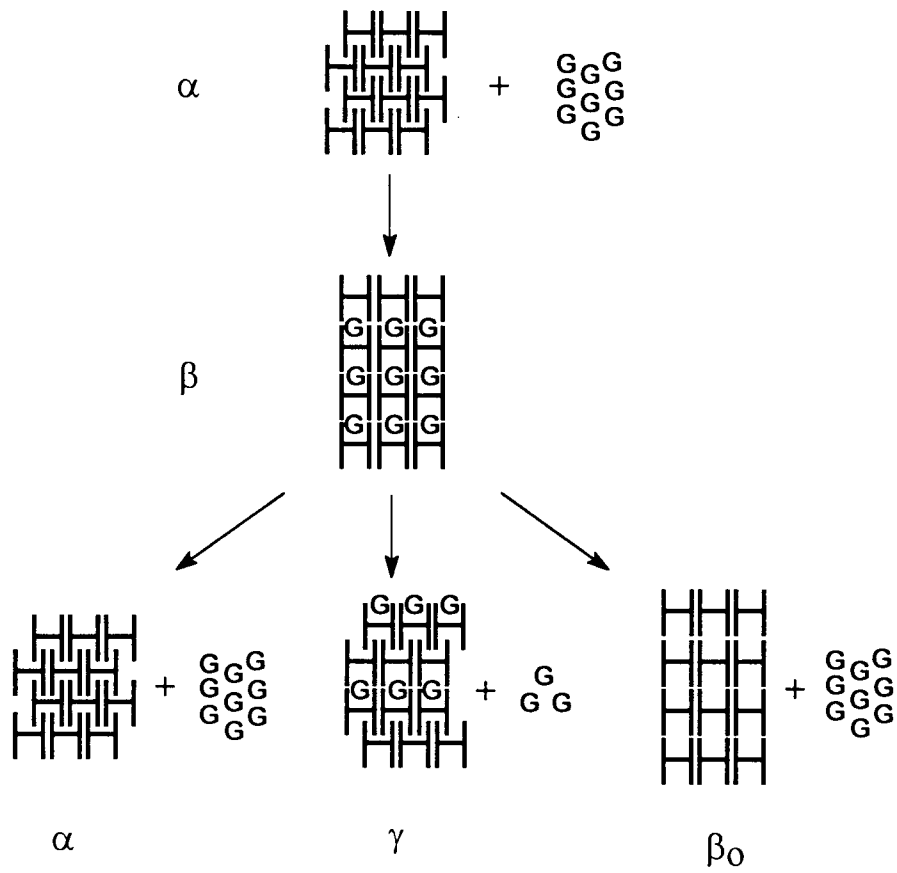

Figure 3.3 Schematic diagram showing the formation and possible decomposition pathways of the inclusion compound containing volatile guest.

The kinetics of the inclusion compounds between organic hosts and volatile guests have received relatively little attention, due to experimental difficulty and instability of the inclusion compounds under ambient conditions. There are several experimental techniques which can be employed to monitor the formation and decomposition of an inclusion compound. These include solid state UV reflectance spectroscopy, solid state NMR spectroscopy, the study of surfaces by atomic force microscopy (AFM), conductivity measurements on compressed samples of the inclusion compound and fast X-ray powder diffraction using position sensitive detectors. We shall discuss two systems which were developed in our laboratory to investigate the formation and decomposition of an inclusion compound formed between a solid host (H) and a volatile guest (G).

Inclusion $H\,(s,\alpha) + nG\,(g) \rightarrow H{\cdot}G_n\,(s,\beta)$

Decomposition $H{\cdot}G_n\,(s,\beta) \rightarrow H\,(s,\alpha) + nG\,(g).$

One is a Levitating Balance (LB)[20], which allows measurements of mass change with time using bulk samples (200-400 mg). The other is a Quartz Microbalance (QMB)[21], which measures the frequency change of a quartz crystal coated with a thin layer of host compound (0.2-0.4 mg). A linear relationship exists between the change in frequency and the change in mass[22], $\Delta f = -kf_o^2\Delta m$, and so the change in frequency recorded can be converted directly to the extent of reaction, α. Both the LB and the QMB can be used under controlled conditions of pressure and temperature, and have been described in detail in Chapter 2. Alternatively the decomposition of inclusion compounds can also be carried out on a Thermogravimeter (TG) under either isothermal conditions at pre-chosen temperatures (Iso-TG) or nonisothermal conditions at a linear heating rate (Programmed TG). Since the isothermal method of analysis yields more reliable kinetic parameters[23], the nonisothermal methods have not been applied in this study.

In order to determine which kinetic rate equation is most suitable for a particular reaction, the α-time data can be used to plot $f(\alpha)$ versus time curves for each model. The model which yields the best linear fit of the data over the widest range of α is chosen. This was done using a computer programme KINETIC[24], which calculates the best-fit linear parameters, the value of the slope (that is, the rate constant, k, for the selected model) and the correlation coefficient over any chosen range of α or time.

Crystalline compounds are characterised by the XRD patterns. In this study, for the four inclusion compounds under investigation, the experimental XRD patterns were compared with the calculated XRD patterns from the crystal structure data using the computer program LAZY PULVERIX[25].

3.2. Inclusion kinetics experiments

The formation of inclusion compound **DACH** was investigated on the QMB and the LB. The results are illustrated in **Figure 3.4**, in which a) shows α-time

curves obtained from the QMB under the same cyclohexanone vapour pressure at three different temperatures, b) shows α-time curves from the LB under cyclohexanone saturated vapour pressure at two different corresponding temperatures. From these curves, we observed that the rate of overall reaction decreased with increasing temperature. This anti-Arrhenius behaviour was first observed by Barbour, Caira and Nassimbeni[26] for the reaction between the host DDDA and acetone vapour. It was later again reported by Coetzee *et al*[27] for this same host with 1,3-dioxolane vapour. Barbour *et al*[26] proposed an empirical rate law:

$$f(\alpha) = k_f \frac{(P - P_o)}{P_o} t$$

where $k_{obs} = k_f \frac{(P - P_o)}{P_o}$ and k_f is the rate constant for the inclusion reaction, P_o is a threshold pressure, below which the inclusion reaction will not take place. A series of k_{obs} values at a certain temperature under different vapour pressures of the guest can be obtained by fitting their corresponding α-time curves to various theoretical kinetic equations. By plotting k_{obs} versus the pressure of the guest vapour, a straight line curve can be obtained. From the equation $k_{obs} = (k_f/P_o)P - k_f$, the threshold pressure, P_o, and the rate constant, k_f, can be calculated for each temperature. For the inclusion reaction of **DACH**, the existence of a threshold pressure, P_o, of the guest, which is essentially required for the formation of the inclusion compound, was experimentally confirmed. We found that the guest uptake reaction did not go to completion at partial pressures of cyclohexanone of about 2 mmHg and less at 25°C. At 40°C, this pressure rose to about 4 mmHg. It was not possible to evaluate P_o and k_f at different temperatures and pressures for the inclusion reaction of **DACH**, since the guest cyclohexanone (b.p.= 155.6°C) is not very volatile. Its saturated vapour pressure is about 10 mmHg at 38.7°C, which makes it practically difficult to obtain the necessary wide range of vapour pressures. Therefore, the activation energy of the forward inclusion reaction could not be evaluated.

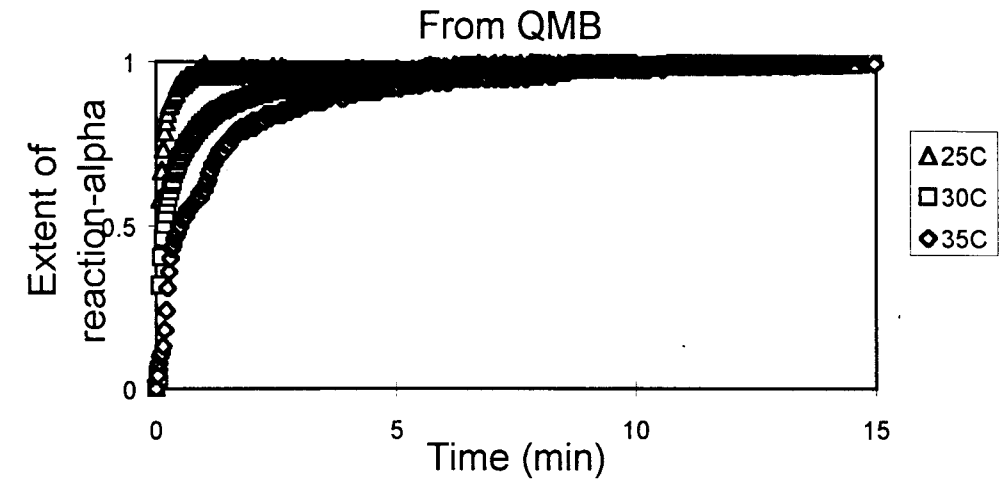

a)

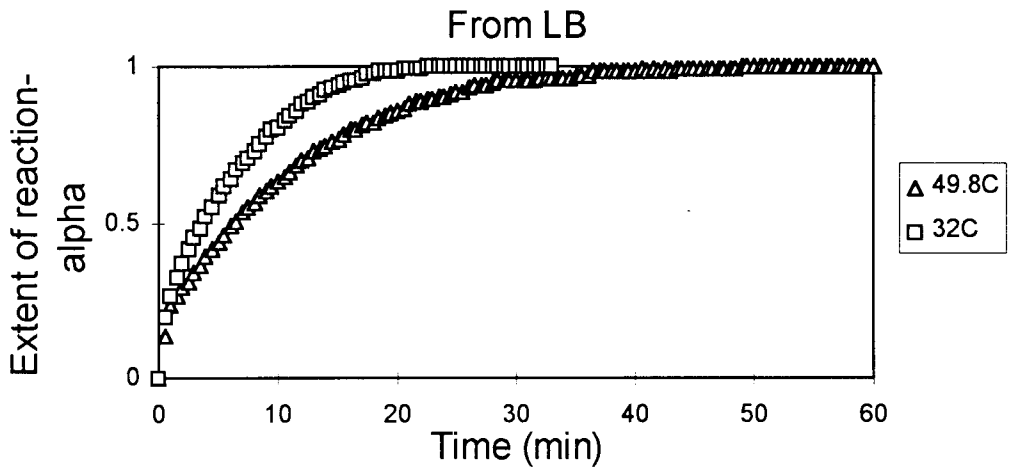

b)

Figure 3.4 α-time curves for the inclusion reaction of **DACH**.
a)obtained from the QMB under approximate 5.5 mmHg vapour pressure.
b)obtained from the LB under the corresponding saturated vapour pressure.

The anti-Arrhenius behaviour has been observed with the other three guest compounds in this study both on the QMB and the LB. It has been suggested[24] that this may be a typical phenomenon for the formation of inclusion compounds, during which the host molecules undergo rearrangement to form a new crystal structure.

We postulate that the following reaction pathway is followed:

$$H(\alpha,s)+G(g)\overset{K_{eq}}{\Leftrightarrow}H(\alpha,s)/G(g)\overset{k_f}{\Leftrightarrow}H\cdot G(\beta,s)$$
$$\xrightarrow[k_{obs}]{}$$

When the host is subjected to the guest vapour, the guest is adsorbed onto the surface of the host compound. This physical adsorption is in equilibrium with gas desorption. The equilibrium constant (K_{eq}) can be written as $k_{eq}=[H(\alpha,s)/G(g)]/[H(\alpha,s)][G(g)]$ for a given temperature. Since the concentration of a solid is unity, and $[G(g)] = P_G$, this simplifies the equilibrium constant to $K_{eq} = 1/P_G$. In this physisorption the α-phase of the host retains its molecular structure. Only once sufficient covering of the guest is obtained by the host, does the structure rearrange to form the β-phase of inclusion compound. In this case, the pressure of the gas is equal to P_o, *i.e.* $P_G = P_o$, $K_{eq} = 1/P_o$. Hence the phenomenon of the existence of threshold pressure was observed. This analysis also explain the anti-Arrhenius behaviour of the inclusion reaction. The observed rate coefficient (k_{obs}) is actually a combination of K_{eq} and k_f. The rate of formation of the inclusion compound can be written as: $v \propto k_f[H(\alpha,s)/G(g)]$, in which $[H(\alpha,s)/G(g)] = K_{eq}[H(\alpha,s)][G(g)]$, therefore we get $v \propto k_f K_{eq}$. Since the physisorption is exothermic, K_{eq} decreases with temperature. Although k_f probably increases with temperature, the equilibrium of the physisorption shifts to the left (K_{eq} decreases) as the temperature is raised, and the change is strong enough for $k_f K_{eq}$ to decrease. Hence the anti-Arrhenius behaviour was observed.

Both the α-time curves obtained from the QMB and the LB were deceleratory. Those obtained from the QMB fitted the three-dimensional diffusion controlled mechanism model (D_3), $[1-(1-\alpha)^{1/3}]^2 = kt$. Those obtained from the LB were best described by the contracting sphere model (R_3), $1-(1-\alpha)^{1/3} = kt$. This difference in mechanism for the same reaction may be due to the difference in experimental conditions as well as the geometry of the samples. On the QMB the host forms a thin layer on the surface of the quartz crystal, whereas a bulk

the host forms a thin layer on the surface of the quartz crystal, whereas a bulk sample was used on the LB. There is also a difference in particle size between the two samples.

The inclusion products formed on the LB were removed from the reaction vessel. They were stored in a sealed container under a positive guest vapour pressure, in order to prevent guest desorption. The samples were analysed using X-ray powder diffraction as well as the Iso-thermal TG for the decomposition kinetics studies. Their XRD powder patterns were recorded and were compared with those obtained from solution (refer to method 2 described in section 2.3.2, Chapter 2) and those calculated from the single crystal structure data as shown in **Figure 3.5** B for **DACH** and in **Appendix A** for **DA2M**, **DA3M** and **DA4M**. Their traces are similar in relative intensities and peak positions, with slight differences due to sample packing. We have hence confirmed that the host DDDA does indeed take up the guest from vapour to form the same inclusion compounds as that formed in solution (β-phase). The α-phase of the non-porous host is also illustrated in Figure 3.5 A and is clearly different from that of the β-phase.

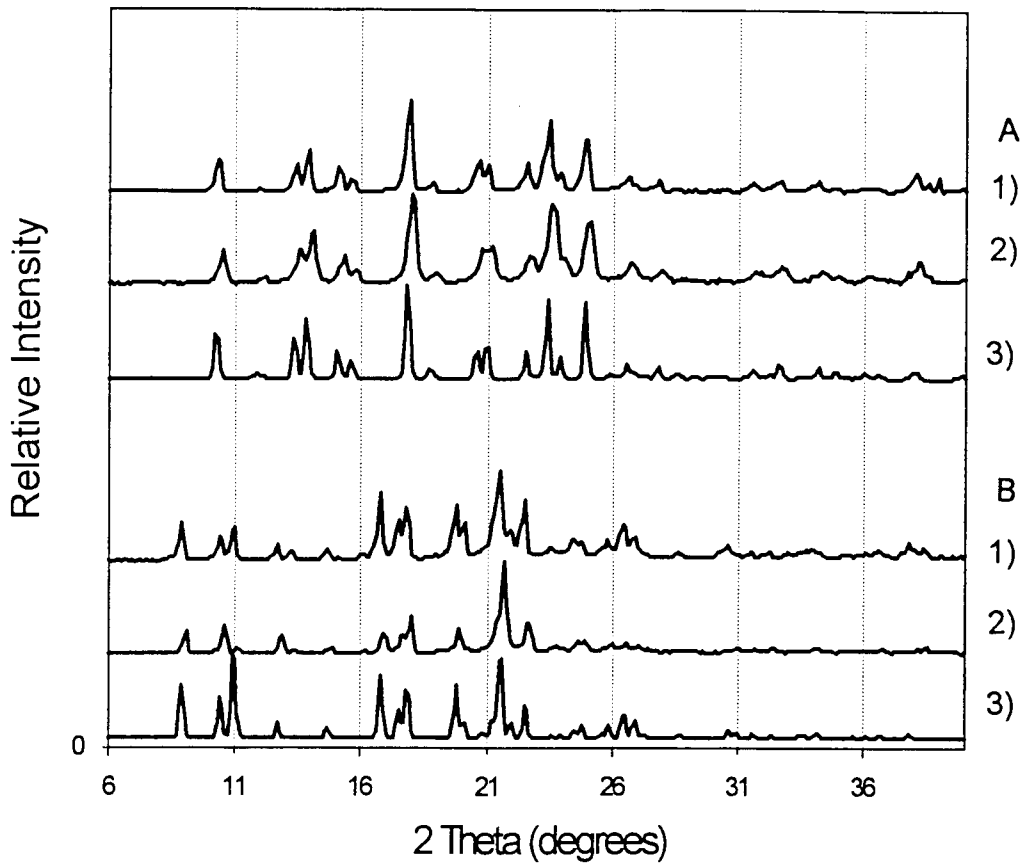

Figure 3.5 XRD traces of:
A 1). the desolvated product from inclusion compound **DACH**;
2). experimental host compound DDDA;
3). calculated from the single crystal structure of the host DDDA;
B 1). **DACH** formed by guest absorption on the LB;
2). **DACH** formed in solution;
3). **DACH** as calculated from the single crystal structure data.

3.3. Decomposition kinetics experiments of DACH

3.3.1. The decomposition of DACH on the QMB

The inclusion compound **DACH** formed in the reaction chamber of the QMB was subjected to vacuum without being disturbed. Hence the decomposition of **DACH** could be studied. The typical α-time curves generated from the frequency change versus time data at five different temperature are shown in **Figure 3.6**.

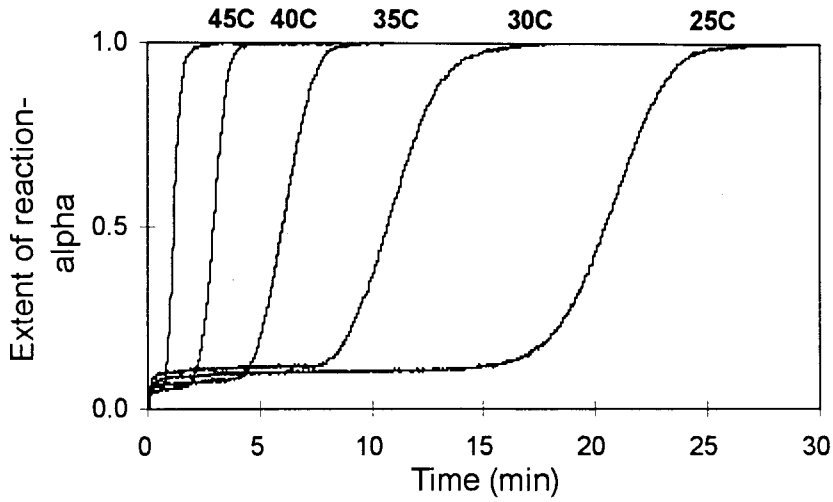

Figure 3.6 α-time curves obtained at 25, 30, 35, 40 and 45°C for the decomposition of **DACH** on the QMB.

It should be noted that the time zero point (t = 0) was counted when pumping of the reaction vessel started. The internal pressure dropped to less than 1 mmHg within 10 seconds. All the curves possess all features illustrated in Figure 3.1. The initial rapid evolution of the guest was typically limited to 5-10 per cent decomposition within 0.3-0.8 min. It may be contributed to desorption of guest which was physically adsorbed onto the surface. Alternatively it may be due to a true surface decomposition or a combined complex reaction. D. A. Young [8] investigated the activation energies of this step for various reactions and found that they were generally about 12-20 kJ/mol and sometimes as high as 166 kJ/mol. In the case of physical desorption one would expect the activation energy to be lower than that for a true surface decomposition. Attempts have been made to evaluate the activation energy of this initial part, but, no convincing rate equation could be obtained. Since this initial part only varies slightly with temperature, we assumed it belongs to surface desorption.

The initial process is succeeded by the induction period. The length of induction period, t_i, is determined by the onset of the main reaction, which is extrapolated from the sigmoid curve. The induction period is regarded as the process of formation of nuclei. It is usually assumed that the rate of the nucleation is always constant during this period, that is:

$$\frac{d\alpha}{dt} = kt_i = const.$$

so, $k \propto 1/t_i$. Accordingly, $\ell n\frac{1}{t_i} = -\frac{E_{a(i)}}{RT} + \ell nA_{(i)}$ where $E_{a(i)}$ and $A_{(i)}$ are the activation energy and pre-exponential factor for the induction period respectively[28, 29]. By plotting $ln\ 1/t_i$ versus $1/T$, we obtained a straight line, which yields the $E_{a(i)}$ = 102 (12) kJ/mol, as illustrated in **Figure 3.7** a).

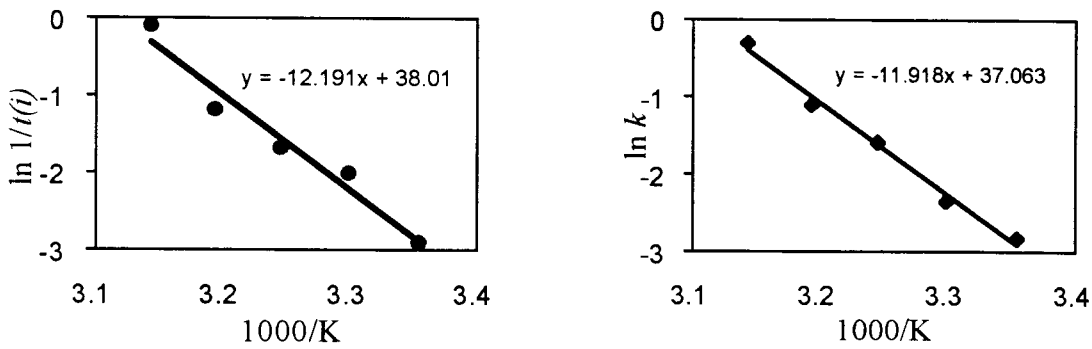

a) b)

Figure 3.7 The least-square plot of a) $ln\ 1/t_i$ versus $1/T$, b) $ln\ k$ versus $1/T$.

The main reaction was characterised by a sigmoidal α-time curve, which consists of the acceleratory period, deceleratory period and final completion. This section of the curve was isolated and analysed separately. It was found to be best described by the Avrami-Erofe'ev equation:

$$f(\alpha) = \left[-\ell n(1-\alpha)\right]^{1/n} = k(t - t_i)$$

where n=4 (A4), over an α range of 0 to 0.95. In order to confirm the chosen model, a plot of the calculated α-time curve, using the value of the rate coefficient obtained from the A4 model, was compared with the experimentally obtained α-time curve. This is shown in **Figure 3.8**. A plot of $ln\ k$ versus $1/T$ yields the activation energy, E_a = 99 (5) kJ/mol, as shown in Figure 3.7 b).

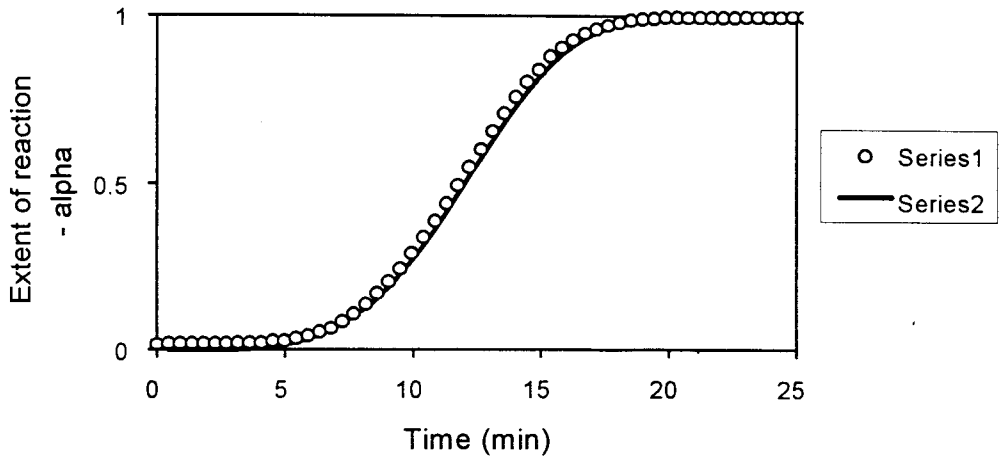

Figure 3.8 Confirmation of the theoretical kinetic model A4 chosen for the decomposition of **DACH** on the QMB. The series 1 is the experimental curve at 298K, the series 2 (solid line) is calculated from the theoretical equation,

3.3.2. The decomposition of DACH on the LB

The kinetics of decomposition of **DACH** were also investigated on the LB under reduced pressure. The host powder samples (refer to method 3, sample C, Chapter 2) were exposed to the guest cyclohexanone vapour. When it was evident that the inclusion reaction had effectively reached completion, the reaction vessel was evacuated and the weight loss versus time data for the decomposition reaction recorded. The resultant α-time curves are shown in **Figure 3.9**. The α-time curves have similar features to those obtained from the QMB, namely the initial rapid evolution of the guest, induction period and main section. The main reaction follows a deceleratory curve, while the curves of the main section from the QMB are sigmoidal. Kinetic analysis showed that the main reaction on the LB was best analysed by the contracting area model (R2): $1-(1-\alpha)^{1/2} = kt$ over an α range of 0.05-0.95. The plots of $ln\ 1/t_{(i)}$ and $ln\ k$ versus $1/T$ are shown in **Figure 3.10**, which yield the activation energy, $E_{a(i)}$, for the induction period of 97(5) kJ/mol, and E_a for the main reaction of 71(6) kJ/mol.

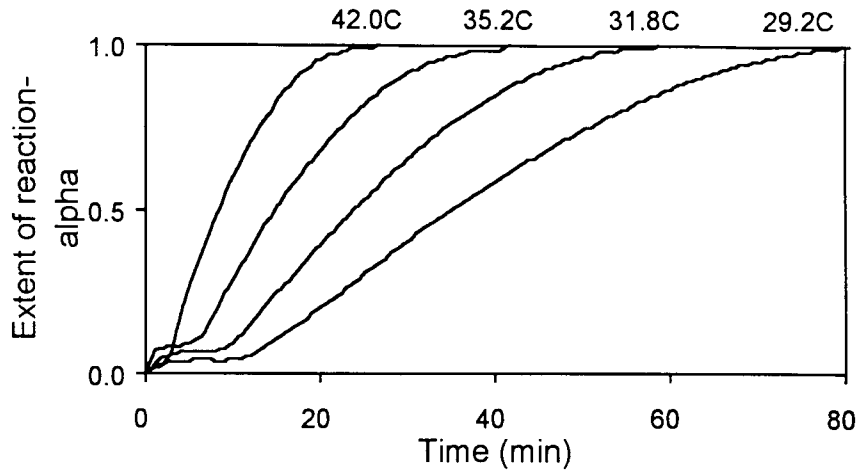

Figure 3.9 α-time curves for the decomposition of **DACH** obtained from the LB (sample C was used).

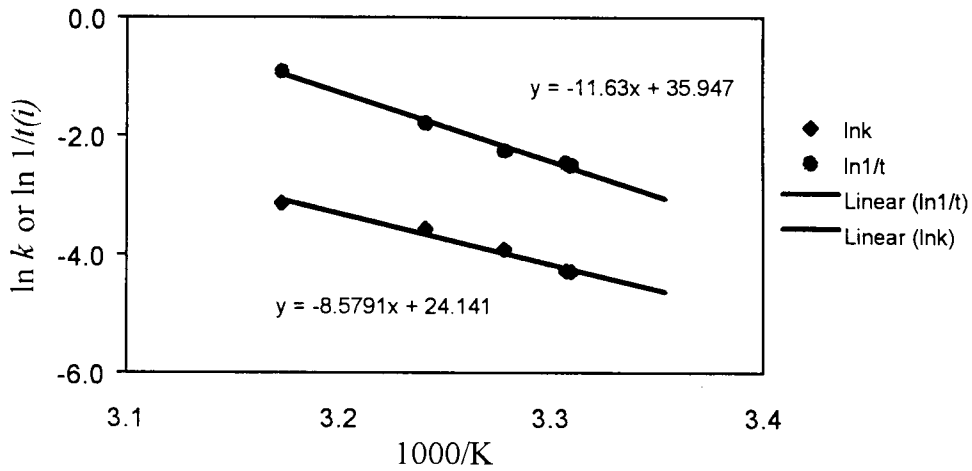

Figure 3.10 Arrhenius plot for the decomposition of **DACH** on the LB.

Following the decomposition reaction on the LB, the desolvated host compound was removed and analysed using XRD. The XRD powder pattern was recorded and compared with that calculated from single crystal structural data of DDDA, which is extracted from the Cambridge Structural Database, as shown in Figure 3.5 A in previous Section. The measured and calculated XRD traces successfully matched each other. This indicated that the β-phase of the inclusion compound **DACH** reverts back to the starting α-phase of the host, upon desolvation.

3.3.3. The decomposition of DACH by means of Iso-TG

As stated previously, powder samples of the inclusion compound **DACH**, prepared on the LB, were removed from the reaction cell and subjected to a series of conventional Iso-TG experiments under nitrogen purge flowing at a rate of 40 ml/min. A typical α versus time curve obtained using sample C is shown in **Figure 3.11**. Clearly, the reaction on the Iso-TG shows deceleratory character without any induction period. Kinetic analysis showed that it was best described by the contracting area model (R2): $1-(1-\alpha)^{1/2} = kt$, over an α range of 0.05 -0.95. A very good Arrhenius plot is obtained, as shown in **Figure 3.12**. This yields the activation energy of 86(3)kJ/mol.

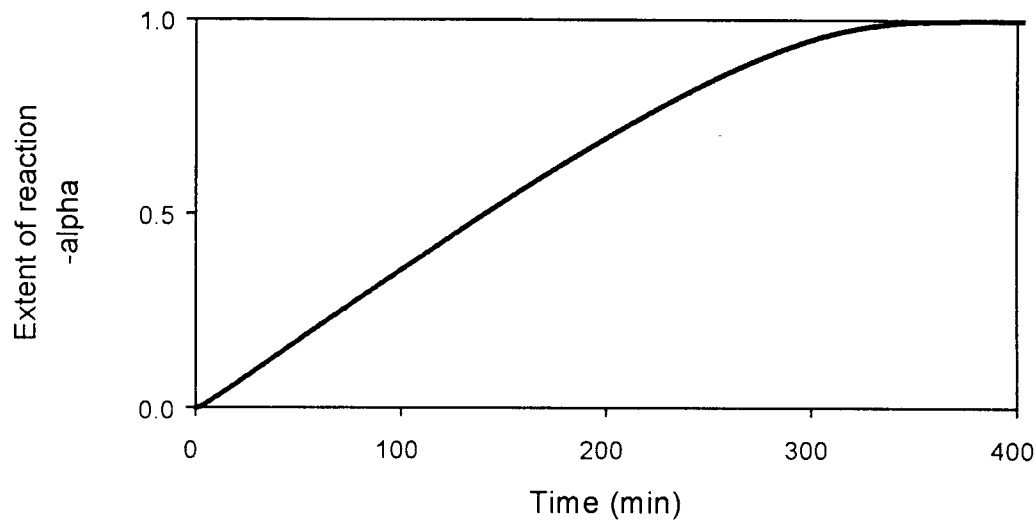

Figure 3.11 The α- time curve for the decomposition of **DACH** on Iso-TG with nitrogen flowing at a rate of 40 ml/min, at 35°C (sample C was used).

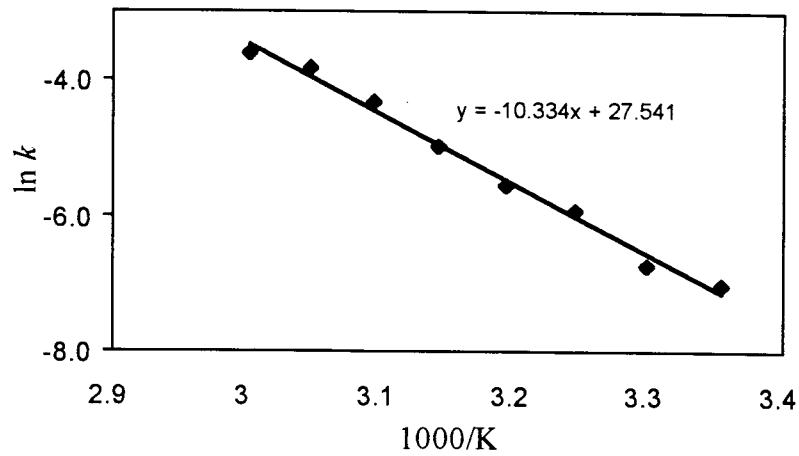

Figure 3.12 Arrhenius plot for the decomposition of **DACH** by means of conventional Iso-TG.

3.3.4. The effect of nitrogen gas flowing

We did not observe an induction period for the isothermal studies performed on the conventional TG as on the QMB and the LB. On both the QMB and the LB, experiments were carried out under reduced pressure without nitrogen gas flowing. We repeated the TG experiments without N_2 gas flowing, using the same powdered sample of **DACH** prepared on the LB (sample C). The Iso-TG experiments of the decomposition of **DACH** under normal atmosphere, without nitrogen gas flowing, were carried out. One example of the resultant α-time curve is illustrated in **Figure 3.13**. It is interesting that the induction period was observed. The main reaction α-time curves are deceleratory as in the case of the LB. Kinetic analysis shows the main reaction was best fitted by the same model R2 as in the case of the LB. The plots of $ln\ 1/t_{(i)}$ and $ln\ k$ versus $1/T$ are shown in **Figure 3.14**. The activation energy obtained for the induction period and the main section are 117(7) and 100(4) kJ/mol respectively.

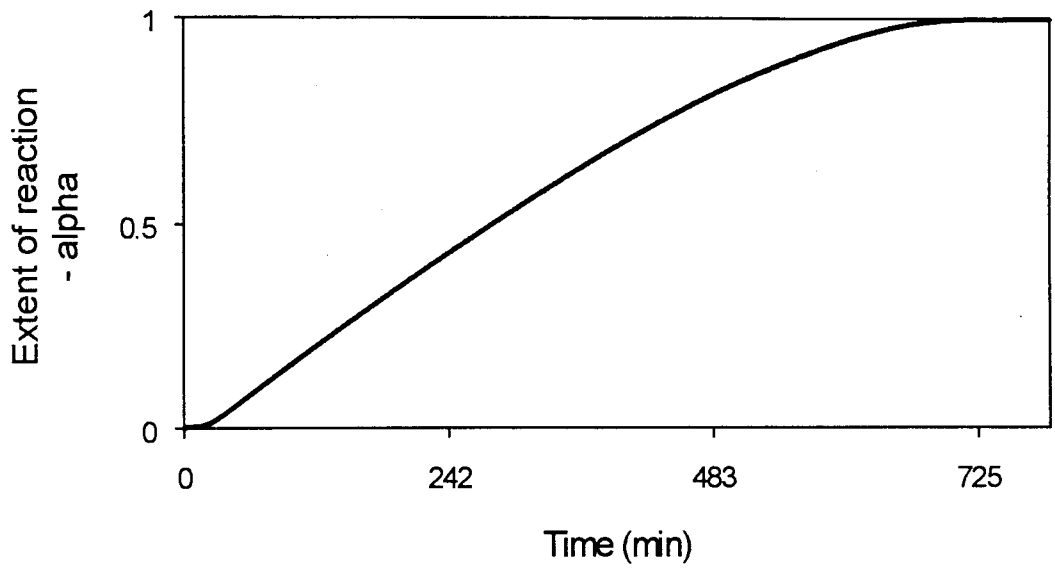

Figure 3.13 The α-time curve for decomposition of **DACH** on Iso-TG without nitrogen gas flowing at 35°C (sample C was used).

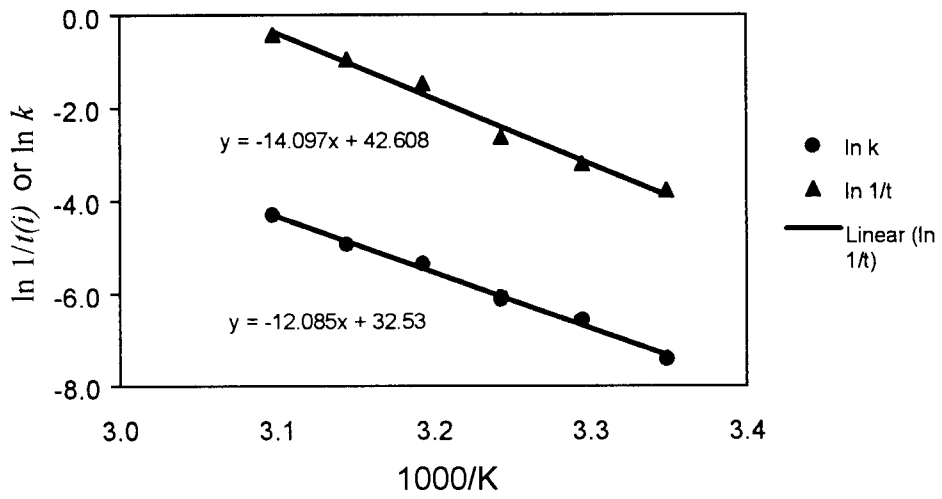

Figure 3.14 Arrhenius plots for the decomposition of DACH on Iso-TG without nitrogen flows.

Table 3.2 The kinetics parameters for the isothermal decomposition of **DACH** obtained by means of different methods. For comparison, the same prepared sample C with the same particle size was used (50 μm), except for the QMB where the particles were < 20 μm in any dimension.

	Temp. range	For induction period $E_{a(i)}$ (kJ/mol)	$ln\, A_i$	Kinetic Model	For main reaction E_a (kJ/mol)	$ln\, A$
QMB	25-45°C	102 (12)	38.0 (3)	A4	99 (5)	37.1 (1)
LB	29-42°C	97 (5)	35.9 (1)	R2	71 (6)	24.1 (1)
Iso-TG* (no N_2)	30-55°C	117 (7)	42.6 (2)	R2	100 (4)	32.5 (1)
Iso-TG** (with N_2)	25-60°C	-	-	R2	86 (3)	27.5 (1)

* Modified Iso-TG without nitrogen gas flow.
** Conventional Iso-TG, which with 40 ml/min nitrogen flowing.

Table 3.2 summarises the kinetics results obtained from the different methods for the decomposition of **DACH**. The Iso-TG experiments, done in a N_2 atmosphere, did not show the existence of an induction period. The activation energies obtained for the induction period using the three different methods, namely the QMB, the LB and the Iso-TG without N_2 gas flowing, were within the range of 97-117 kJ/mol. The main section of the reaction was found to be sigmoidal in the QMB experiments, following the Avrami-Erofe'ev model (A4), but deceleratory in all other cases, following the contracting area model (R2). The activation energies obtained from the main section ranged between 71 and 100 kJ/mol.

The nitrogen gas flow seems to alter the kinetic behaviour, eliminating the induction period. In order to verify this, we have tried to carry out the decomposition reaction of **DACH** on the QMB under constantly renewed nitrogen gas flow and ambient pressure, instead of under vacuum by pumping. But, the reaction still showed an induction period, which was only slightly shorter than before.

3.3.5. The effect of particle size

The influence of average particle size and the size distribution of the reactant on decomposition of a solid is well known[30-33]. The variation in particle size distribution may significantly change the shape of α-time curves[34,35] and apparent reaction rate, leading to different kinetic model obedience[36,37]. The difference is particularly significant between single crystals and powder samples. The preparation and pre-treatment of the reactant may also have an influence on the kinetic results[9].

In the studies of the thermal decomposition of **DACH,** single crystals and three kinds of powder samples were studied by means of conventional Iso-TG, in order to investigate the contribution of the shape and size, as well as the preparation of the reactant on the kinetic parameters and reaction rate. The single crystal used is about 1 x 2 x 2 mm. The other three samples, A, B and C, are fine powders, which were obtained by different methods as described in Chapter 2, Section 2.3.3, and of which the particle sizes are characterised by the mean values and approximately log-normal distributions. Sample A and C were prepared on the LB by exposing the host to guest vapour, and have particle sizes of about 70 and 50 μm respectively. Sample B was formed by stirring a solution of the host DDDA in cyclohexanone, and has a mean particle size of about 50 μm, which is similar to the size of sample C. The resultant weight loss versus time curves at 40°C are illustrated in **Figure 3.15**.

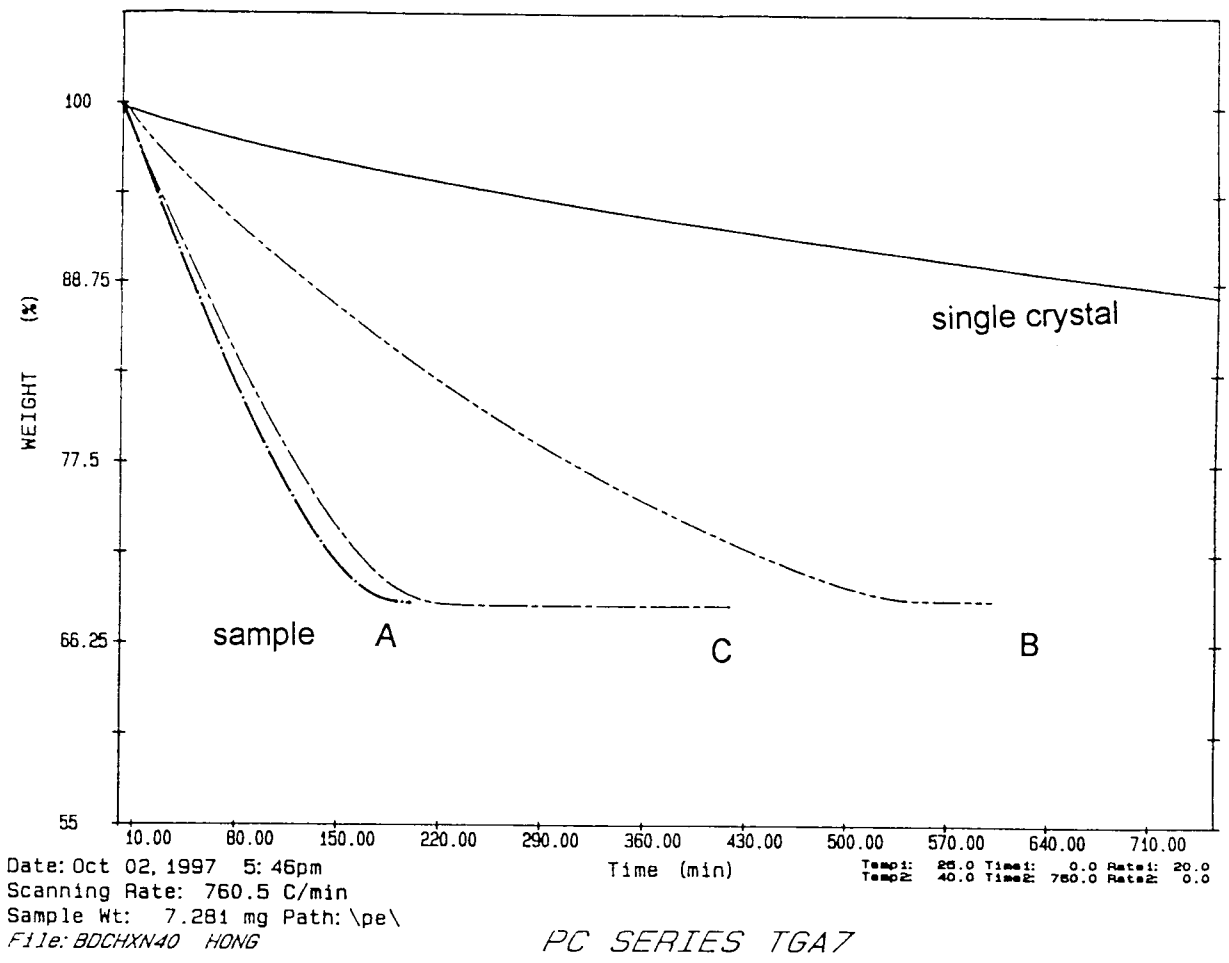

Figure 3.15 The weight loss (%) versus time curves for the decomposition of **DACH** by means of conventional Iso-TG using different samples at 40°C.

Figure 3.15 shows that there is a significance increase in the rate of reaction from single crystals to powder samples. Powder samples B and C, obtained by different methods, have approximately the same particle size distribution, but show a larger difference in reaction rate than the difference between sample A and C, which has slightly different particle sizes but were both formed by the same method. This result illustrates that particle size distribution has a significant influence on the reaction rate when comparing single crystals to powder samples. When looking at different powdered samples a small change in size does not change the reaction rate significantly. In this case the sample preparation has a greater influence on the reaction rate. The kinetic analysis shows all of the reactions obey the contracting area geometrical kinetic model (R2) besides the large single crystal which follows the diffusion controlled

model. This result is to be expected, since in the large crystal diffusion will play a predominant role, masking any other mechanism. The α-time data for the large crystal did not obey any diffusion kinetic equation contained in Table 3.1 uniquely (D1 - D4). The two models (D2 and D4) which fitted best were chosen for the crystal in order to calculate the kinetic parameters. Arrhenius parameters obtained for all samples are listed in **Table 3.3**. It is observed that the particle size and the preparation of samples changed the magnitude of the Arrhenius parameters significantly, as well as the chosen kinetic model.

Table 3.3 Kinetic parameters for the decomposition of **DACH** by means of conventional Iso-TG, using different samples prepared by different methods.

	The mean particle size (μm)	Temperature range(°C)	Kinetic Model	E_a (kJ/mol)	$ln\,A$
Sample A	70	25-45	R2	85 (4)	27.2 (1)
Sample B	50	35-70	R2	98 (3)	31 (1)
Sample C	50	25-60	R2	86 (3)	27.5 (1)
Single crystal	1 x 2 x 2 mm	55-75	D2 D4	104 (12) 109 (11)	31.6 (2) 32.1 (2)

3.3.6. Microscopic observation of the decay of DACH

Several single crystals of **DACH** were placed in the TG reaction furnace without N_2 gas flowing at room temperature. It was observed that the decomposition reaction showed an induction period as long as 6 hours, during which no measurable mass loss occurred. After 8 hours, at which the mass loss was less than 4% (converted to the extent of the reaction it is about 0.1), the crystals were removed and observed on a microscope. The photographs are shown in **Plate 3.1**. In plate 1 (8 hours) the formation of nuclei at defects in the crystal can clearly be seen. The plate 2 (12 hours) shows that these "islands" of product have grown. In plate 3 (24 hours), only small sections of reactant are still shown. This series of photographs illustrates the macroscopic features related to the model of nucleation, followed by growth of the product.

1) After 8 hours

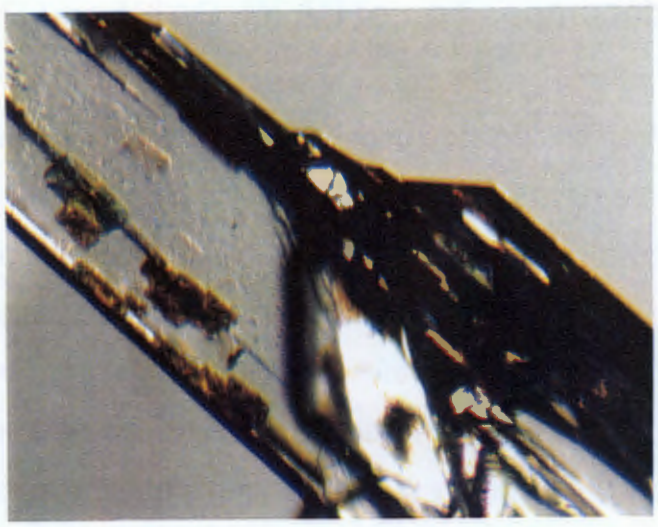

2) After 12 hours

3) After 24 hours

Plate 3.1 Microscopic observation of the decay of **DACH**. 30 x enlarged.

3.4. The decomposition of DA2M, DA3M and DA4M

The other three compounds under investigation have been subjected to kinetic analyses. We have compared the kinetics of decomposition of **DA2M**, **DA3M** and **DA4M** by means of conventional Iso-TG. For comparison, all the samples were obtained from the LB and possessed similar particle size distributions (sample C). Series of isothermal TG experiments were carried out over appropriate temperature ranges. All the α-time curves were deceleratory and were uniquely described by the contracting area kinetic model (R2): $1-(1-\alpha)^{1/2} = kt$. The Arrhenius parameters were obtained over an α range of 0 to 0.95 with correlation coefficients between 0.991 to 0.999. All the plots of $\ln k$ versus $1/T$ and kinetic results are shown in **Figure 3.16** and **Table 3.4** respectively.

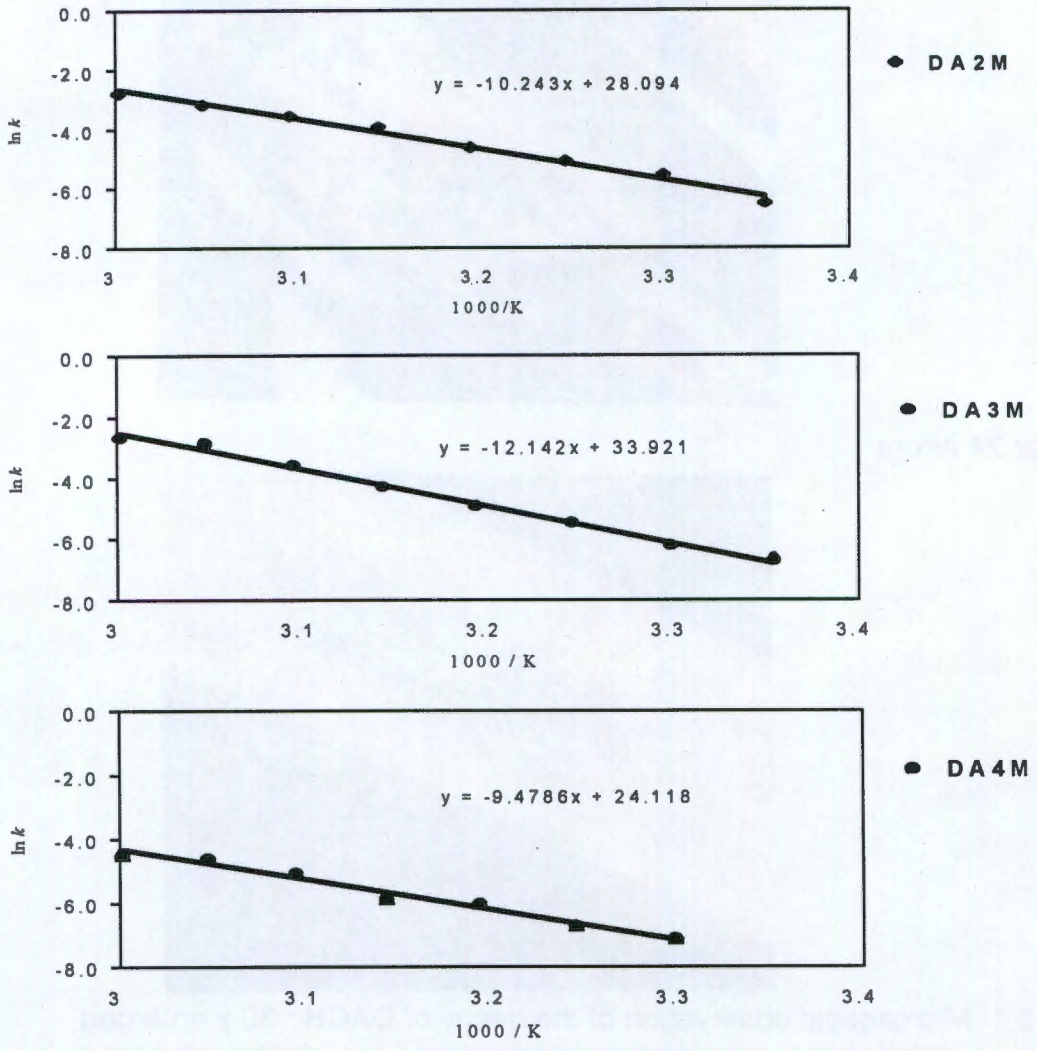

Figure 3.16 Arrhenius plots of $\ln k$ versus $1/T$ for the decomposition of **DA2M**, **DA3M**, **DA4M** by means of conventional Iso-TG.

obtained from the kinetic experiments done on powdered samples of **DACH**. This is shown in **Figure 3.18**. It is clear that an approximately linear relationship exists between the Arrhenius parameters. The values of T_{iso} and k_{iso} obtained from this plot are 331.4 K and 0.069 min^{-1} respectively.

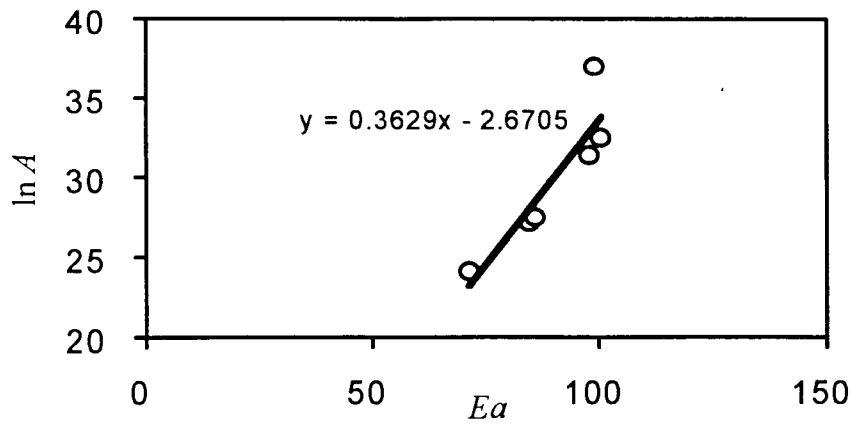

Figure 3.18 Compensation behaviour for the decomposition of **DACH**.

3.6. Discussion

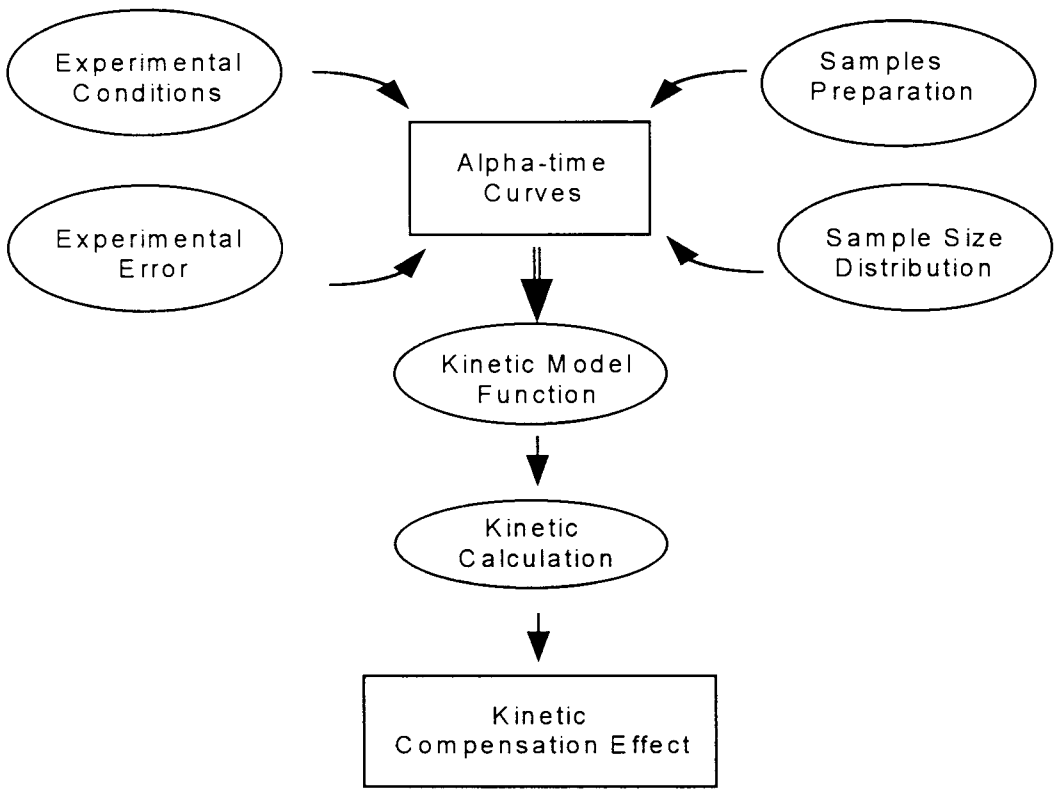

Figure 3.19 Schematic representation of the procedure of the decomposition of **DACH** kinetics.

The major features affecting the kinetics of isothermal decomposition of **DACH** are schematically shown in **Figure 3.19**. The variation in both the experimental and physicochemical factors, *e.g.* the experimental conditions, sample pre-treatment and size distribution, influence the kinetics of the process. This is detected as a change in the shape of the α-time curves. Such changes in the α-time curves result in distortion of the kinetic parameters and their consequent interdependence. In this respect, the establishment of the kinetic compensation effect itself might not have any physical significance[42]. What it does illustrate is that , irrespective of experimental technique and conditions, a temperature (T_{iso}) exists at which the rate coefficients of all the different reactions are equal.

References

1. S. Arrhenius, *Z. Phys. Chem.* (Leipzig)4, 1889, p226.
2. W. C. McC. Lewis, *J. Chem. Soc.*, 113, 1918, p471.
3. W. F. K. Wynne-Jones and H. Eyring, *J. Chem. Phys.* 3,1935, p492.
4. H. Eyring, S. H. Lin and S. M. Lin, 'Basic Chemical Kinetics', Wiley, New York, 1980.
5. K. J. Laidler, 'Reaction Kinetics', Vol.1, 'Homogeneous Gas Reactions', Vol.2, 'Homogeneous Reactions In Solution'. Pergamon press, 1963.
6. K. J. Laidler, 'Chemical Kinetics', McGraw-Hill, New York, 1965.
7. M. E. Brown, 'Introduction To Thermal Analysis - Techniques And Applications', Chapman and Hall, London, 1988
8. D. A. Young, 'Decomposition Of Solids', Pergamon press, 1966.
9. M. E. Brown, D. Dollimore and A. K. Galwey, 'Comprehensive Chemical Kinetics', Vol. 22, 'Reaction In The Solid State', Elsevier, Amsterdam, 1980.
10. J. H. Sharp, G. W. Brindley and B. N. Narahari Achar, *J. Amer. Ceram. Soc.* 49(7), 1966, p379.
11. D. Dollimore, 'Thermal Analysis-Techniques and Applications', E. L. Charsley and S. B. Warrington (eds).
12. A. K. Galwey, *J. Therm. Anal.*, 41,1994, p267.
13. A. K. Galwey and M. E. Brown, *Proc. R. Soc.* Lond. A450, 1995, p501.
14. P. D. Garn, *Crit. Rev. Anal. Chem.*, 3, 1972, p65; *J. Therm. Anal.*, 13, 1978, p581.
15. M. Arnold, G. E. Veress, J. Paulik and F. Paulik, *Thermochim. Acta*, 52, 1982, p67; *Anal. Chim. Acta*, 124, 1981, p341
16. W. Gomes, *Nature*, 192, 1961, p865.
17. J. Pysiak, *J. Therm. Anal.*, 43, 1995, p9.
18. W. W. M. Wendlandt, 'Thermal Analysis', John Wiley and sons, New York, 1964.
19. D. Dollimore, *Thermochim. Acta.*, 203, 1992, p7.
20. L. J. Barbour, K. Achleitner and J. R. Greene, *Thermochim. Acta*, 205, 1992, p171.

21. A. Coetzee, L. R. Nassimbeni and K. Achleitner, *Thermochim. Acta*, 298, 1997, p81.
22. (a) G. Z. Sauerbrey, *Phys. Verha.*, 8,1957, p113;
(b) G. Z. Sauerbrey, *Z. Phys.*, 155,1959, p206.
23. L. R. Nassimbeni, 'Crystallography of Supramolecular Compounds', p285, Kluwer Academic Publishers, 1996.
24. L. J. Barbour, PhD Thesis, University of Cape Town, 1994.
25. K. Yvon, W. Jeitschko and E. Parthe, *J. Appl. Cryst.*, 10, 1977, p73.
26. L. J. Barbour, M. R. Caira and L. R. Nassimbeni, *J. Chem. Soc., Perkin Trans.* 2, 1993, p2321
27. M. R. Caira, A. Coetzee, L. R. Nassimbeni and F. Toda, *J. Chem. Res. (S),* 1996, p280.
28. C. Mlawnds, PhD Thesis, University of Cape Town, 1972.
29. EG. Shephard, PhD Thesis, University of Cape Town, 1974.
30. L. L. Bircumshaw and B. H. Newman, *Proc. R. Soc.* London, Ser. A. 227, 1954, p115; 227, 1955, p228.
31. K. J. Gallagher, 'Reactivity of Solids', Proc. 5th Int. Symp., Elsevier, Amsterdam, 1965, p192.
32. H. Sasaki, *J. Am. Ceram. Soc.* 47, 1964, p512.
33. M. Ochiai and R. Ozao, *Thermochim. Acta.* 198, 1992, p279 and p289.
34. A. Engberg, *Acta. Chem. Scand.*, 24, 1970, p931.
35. P. C. Kapur, *J. Am. Ceram. Soc.*, 56. 1973, p79.
36. R. W. Hutchinson, S. Kleinberg and F. P. Stein, *J. Phys. Chem.*, 77, 1973, p870.
37. P. G. Fox, *J. Solid State Chem.*, 2, 1970, p491.
38. A. K. Galway, *Catal. Rev.*, 26, 1977, p247.
39. R. K. Agrawal, *J. Therm. Anal.*, 31, 1986, p1141; 35, 1989, p909.
40. N. Koga and J. Šesták, *Thermochim. Acta,* 182, 1991, p201.
41. J. Šesták, *Thermochim. Acta,* 32, 1987, p325.
42. H. Tanaka, N. Koga and J. Šesták, *Thermochim. Acta*, 203, 1992, p203.
43. J. Zsako, Cs. Varhelyi and K. Szilagyi, *J. Therm. Anal.*, 7, 1975, p41.

Table 3.4 Kinetic parameters of isothermal decomposition of all four inclusion compounds under investigation by means of conventional Iso-TG, using samples C.

	Temp. range (°C)	Kinetic model	E_a (kJ/mol)	$ln\,A$
DACH	25-60	R2	86 (3)	27.5 (1)
DA2M	25-60	R2	85 (4)	28.1 (2)
DA3M	25-60	R2	101 (3)	33.9 (1)
DA4M	30-60	R2	79 (5)	24.1 (2)

The activation energies obtained for the different decomposition reactions were in the range of 80-100 kJ/mol, with the decomposition of **DA4M** showing the lowest activation energy and **DA3M** the highest.

The desolvated inclusion compounds **DA2M**, **DA3M** and **DA4M** were analysed using XRD. The XRD powder pattern was recorded and compared with that calculated from single crystal structural data of DDDA, which is extracted from the Cambridge Structural Database, and this is shown in **Appendix A**. The measured and calculated XRD traces successfully matched each other. This indicated that the β-phase of the product reverts back to the starting α-phase of the reactant (the host DDDA), upon desolvation.

3.5. Kinetic compensation effect

It is a known phenomenon that for a group of related reactions, a linear relationship exists between E_a and $ln\ A$[38]. This is called the kinetic compensation effect and is expressed generally as follows:

$$ln\,A = bE_a + c$$

where b and c are constants. This effects has been observed both for heterogeneous and homogeneous reactions[9]. Although much effort has been focused on the theoretical interpretation of this phenomenon, there is still no satisfactory explanation and it remains a puzzle for many scientists[39-41]. However, Zsako *et al* [43] have suggested that, the parameter *b* characerises

the strength of the bond to be broken, and *c* is related to the structure of, and defects in, the starting reactant.

For the decomposition of all four inclusion compounds under investigation, the Arrhenius parameters, obtained from Iso-TG, show an approximately linear relationship, as illustrated in **Figure 3.17**. Hence the compensation behaviour exists between the Arrhenius parameters for these four related reactions.

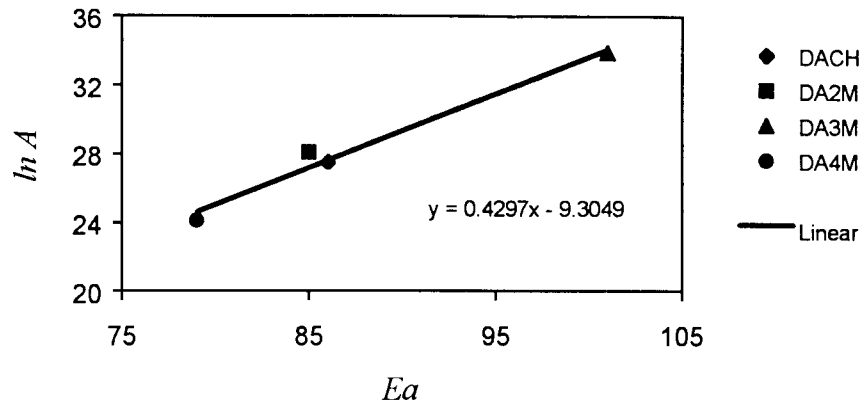

Figure 3.17. Compensation behaviour for the decomposition of **DACH**, **DA2M**

Tanaka[42] has investigated the effect of sample preparation, measuring conditions, experimental errors and the properties of the reaction itself on the subsequent Arrhenius parameters obtained. He has found that a kinetic compensation effect (KCE) exists showing the mutual interdependence between $ln\ A$ and E_a for kinetic studies, in which the apparent values of the Arrhenius parameters change with sample preparation and measuring conditions. The KCE can be expressed as

$$ln\ A = E_a/RT_{iso} + ln\ k_{iso}$$

where *R* is the gas constant and T_{iso} is the isokinetic temperature at which the rate constants of the all the processes compared have a unique value k_{iso}.

In the kinetic studies of the decomposition of inclusion compound **DACH**, the apparent values of E_a and $ln\ A$ were found to change with sample preparation and different experimental conditions, showing the mutual interdependence between these two Arrhenius parameters. We decided to plot $ln\ A$ versus E_a,

CHAPTER 4

THERMAL ANALYSES

4. THERMAL ANALYSES

4.1. General introduction

The study of the effect of heat on material has a long history, since almost every substance undergoes physical and chemical changes on heating. Over the last quarter of this century, thermal analysis has passed through phases of full recognition and consolidation to reach the present period of further rapid increase in applications ranging from polymers to earth science[1].

The currently accepted definition of thermal analysis, as given by Brown[2] and the International Confederation for Thermal Analysis (ICTA) is: *the measurement of changes in physical properties of a substance as a function of temperature, whilst the substance is subjected to a controlled temperature programme*. It also has been suggested[3] that the definition should be extended to allow for rapid heating of the sample to some elevated temperature, followed by measurement of the property with time under isothermal conditions, i.e. at zero heating rate.

The physical properties which can be measured by thermal techniques include mass, enthalpy, dimensions as well as mechanical, acoustic, optical, electrical and magnetic properties. The most widely used techniques are thermogravimetry (TG) and differential thermal analysis (DTA), followed by differential scanning calorimetry (DSC) and thermomechanical analysis (TMA)[4]. It is usual to combine two or more techniques in order to get sufficient and complementary information. For example, it is fairly common to complement all DSC or DTA data with TG.

The use of combined techniques such as Hotstage Microscopy (HSM), DSC, TG and Evolved Gas Analysis (EGA) for investigating inclusion compound desolvations has been described[5]. EGA employing mass spectroscopy (MS)

or infrared spectroscopy (IR) also can be used in combination with TG or DTA to determine the identity and amount of desolvated evolved gas products.

The thermal analysis techniques applied in this study were TG, DSC and HSM.

4.2. TG, DSC and HSM

For solid inclusion compounds which release their guests and undergo phase transformations upon heating, TG and DSC can be used to obtain quantitative information on the interaction energy between host and guest molecules. Hence establishing a trend for similar compounds about its thermal stability, as well as determining phase transformations by the accompanied enthalpy change. These issues have been discussed for a number of clathrate systems such as Werner clathrates[6] and diol host compounds with a variety of organic guests[7,8].

For the general decomposition reaction of inclusion compounds:

$$H \cdot G_n(s,\beta) \xrightarrow[\Delta]{} H(s,\alpha) + nG(g)$$

TG measures the weight loss of solid inclusion compound, due to guest release, while it is subjected to a selected temperature program under controlled atmospheres. The enthalpy changes which accompany the loss of guest, phase transformations and melting of guest-free host are conveniently measured by DSC. The idealised schematic TG and DSC traces of a solid inclusion compound containing a volatile guest is given in **Figure 4.1**.

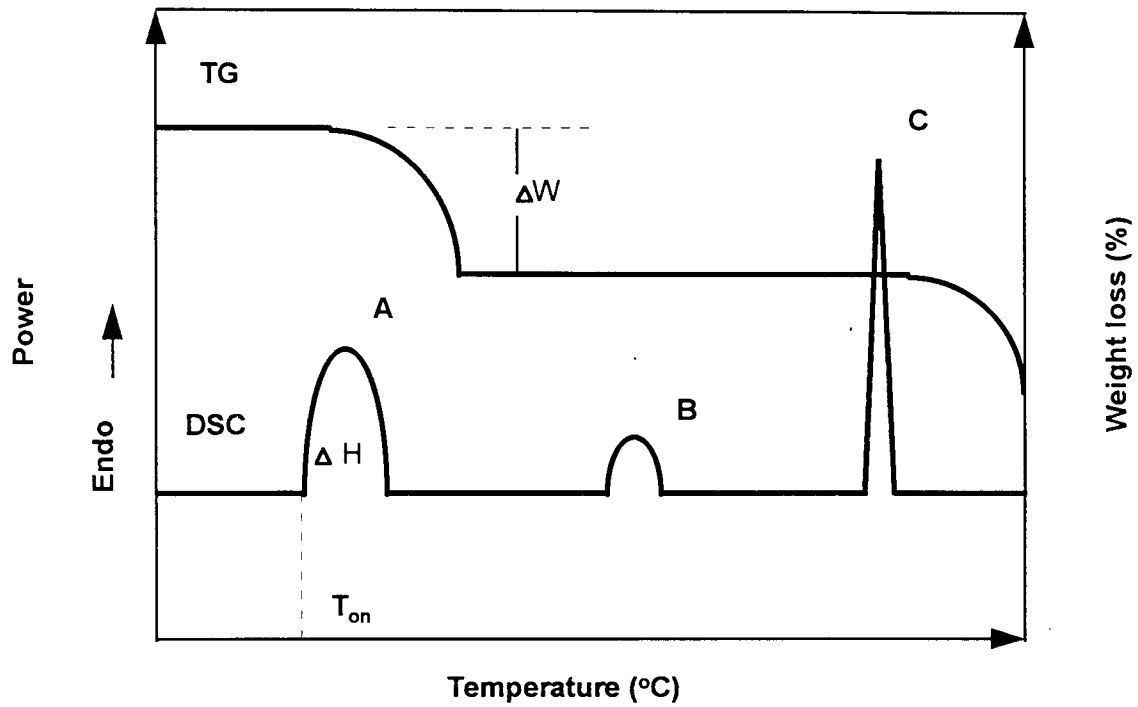

Figure 4.1 General TG and DSC curves of an inclusion compound with a volatile guest

A primary application of TG is the determination of host:guest ratios, however, much effort has been expended on extending this technique for isothermal and non-isothermal decomposition kinetics[9,10]. The isothermal TG method for kinetics has been employed in this study, the results have been discussed in Chapter 3. From Figure 4.1, the inclusion compound shows a single mass loss step, ΔW. This yields an accurate host:guest ratio for the compound under study. The result thus obtained can be usefully employed in crystal structure analysis, where the site occupancy factors of the guest atoms can be sensibly assigned[11].

DSC is used to evaluate the enthalpy change associated with guest release, phase changes and melting, as well as their onset temperatures. In Figure 4.1, the endothermic peak A represents a one-step guest release, the area under the peak can be measured, to obtain a value of ΔH. The endothermic peak C indicates the melting of guest-free host compound. The presence of peak B could be interpreted as follows (refer also to Figure 3.3 in Chapter 3): The inclusion compound with a β-phase frame-work loses all the guest, and forms

an intermediate metastable phase. This could be a β_o-phase if the frame-work of the host molecule is retained after loss of the guest, or another polymorphic form. When the metastable phase undergoes a molecular rearrangement to form the α phase, it gives rise to peak B, which therefore represents a phase change. Peak B is often not observed. In this case, as the guest is released from the inclusion compound, concomitantly the β-phase rearranges and the α-phase is formed, there is no perceivable intermediate stage between the β-phase and the α-phase. Peak B may also be associated with other thermal events, for instance, sublimation, recrystallization, or decomposition, although in the latter case the process is often exothermic, and therefore the peak is reversed with respect to the basic line.

The mechanism of the phase change is not very clear, but the different phases can be investigated and their existence verified by X-ray powder diffraction. In addition, for two or more step guest release reactions, the DSC trace can exhibit two or more peaks, which represent guest release. Depending on the number of phase changes, there may also be more than one peak between A and C. It must be noted that under incorrectly chosen heating rates, some peaks might disappear on the DSC trace[11].

From the DSC trace, we also can get T_{on}, the onset temperature characterising the start of the guest release. The thermal stability of the inclusion compound can be regarded as "its ability to maintain the guest as nearly unchanged as possible on heating"[4]. Therefore T_{on} for a group of similar inclusion compound depends on both the host-guest interactions and the physical properties of the guest, especially the normal boiling point of the volatile guest (T_b). It was found that the difference between T_{on} and T_b, or T_{on}/T_b is a reliable indication of the relative thermal stability of inclusion compounds[11].

There are two factors or conditions that affect the TG and DSC experiments, namely instrumental factors, including mainly heating rate, furnace atmosphere, sample holder, and calorimeter *etc.*; and the sample

characteristics, for example, sample mass, particle size, packing density, and thermal conductivity. In order to resolve the problems of reproducibility of duplicated runs and to compare the results, the experimental conditions and sample preparation should be kept constant.

Often, Hotstage Microscopy (HSM) is a useful complementary technique. It is used as a visual method to observe the thermal events of samples during the heating process. Generally, sublimation, recrystallisation and melting can be seen. Subsequent phase changes may also be visible, such as growth of new crystal phases. If the crystals are suspended in an inert medium (e.g. silicone oil), desolvation is easily detected by the evolution of gas bubbles. Since desolvation is often accompanied by a change in crystal structure, it is also accompanied by the change of the crystal from clear to opaque. The temperature at which any phenomenon is observed by the HSM may be correlated with the DSC onset temperatures.

4.3. Experimental results and discussion

The programmed TG, DSC and HSM methods employed in this thermal studies were described in detail in Chapter 2. The powder samples used for the TG and DSC experiments were prepared using method 3 (described in Section 2.3.2, Chapter 2) by exposing the host to the targeted guest vapour to form an inclusion compound on the Levitating Balance, so that the samples all had the same particle size. In the TG and DSC runs, fairly constant conditions with respect to sample mass (4-5 mg), heating rate (10°C/min) and furnace purge gas (N_2, 40 mL/min) have been used. Therefore comparison of their results to establish the relative thermal stability of the different inclusion compounds is valid. However, it still must be noted that TG and DSC curves were not always in perfect agreement mostly due to the difference in experimental geometry. In the TG experiment the samples are placed in an open platinum pan, whereas the DSC samples are placed in crimped and vented aluminium pans.

4.3.1. DACH

The TG and DSC plots of compound **DACH** are shown in **Figure 4.2**. **DACH** having a 1:2 host:guest ratio has a theoretical guest weight% of 35.0%. From the TG trace in Figure 4.2, it can be seen that from 69 to 128°C, 34.3% weight loss is observed. At about 258°C the weight % starts to decrease again and this is attributed to host decomposition accompanying the melt.

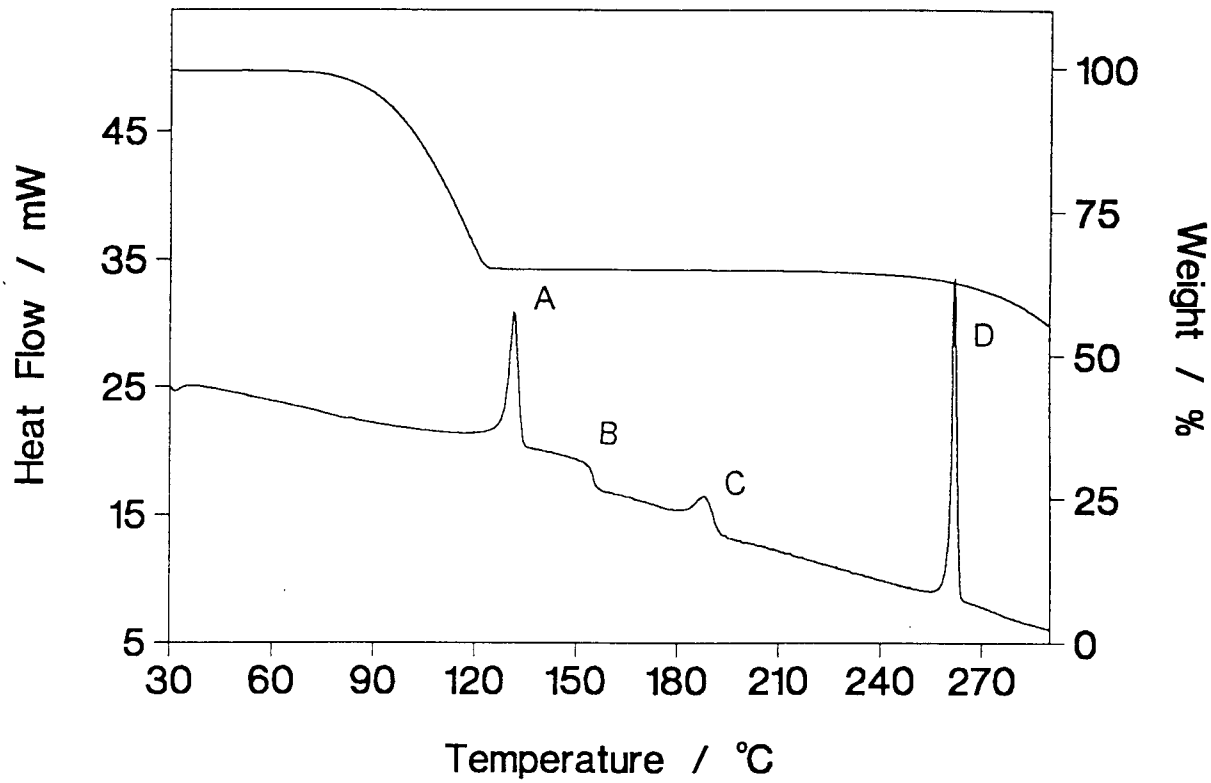

Figure 4.2 TG and DSC curves of compound **DACH**.

The DSC trace in Figure 4.2 is characterised by three sharp endothermic peaks A, C and D. The first peak A having a onset temperature of 128.5°C is attributed to guest release in a one-step reaction. The area under the endothermic peak gives the enthalpy change (ΔH = 35.5kJ/mol) upon guest loss from the host-guest compound. The third sharp endothermic peak D with T_{on} = 260.5°C corresponds to the melting of guest-free host, and is confirmed by the melting point of the synthesised host stated in Chapter 2. The peak C between guest release (peak A) and host melting (peak D) with T_{on} = 184.2°C

may be associated with a phase change or other thermal event. A diffused step B in the baseline is observed after peak A at 158°C.

In order to correctly interpret the DSC trace, direct observations were made by HSM on a clear crystal of **DACH**. The crystal was placed between thin glass slides. Upon heating the crystal on the Hotstage at a controlled heating rate, photographs were taken whenever a thermal event was observed. At the beginning, the crystals were heated at a linear rate of 10°C/min. After the initial sublimation was observed, the heating rate was changed to 5°C/min in order to slow down the process for taking photographs. These photographs are shown in **Plate 4.1** and described as follows:

Plate 1 shows the lath-shaped crystal of compound **DACH** at room temperature with mother liquor under polarised light.

Plate 2 was taken at 60°C, the crystal is losing its guest, and turning opaque gradually.

Plate 3 taken at 160°C shows that the crystal has become totally opaque, which indicates the guest loss is complete, but still maintains its shape.

Plate 4 taken at 200°C shows the tiny spots around the crystal indicating sublimation which initially started at about 190°C.

Plate 5 was taken at 230°C, sublimation continues and the host recrystallises on the cover slide.

Plate 6 taken at about 268°C shows the host has sublimed and recrystallised to form tiny perfect crystals on the cover slide.

Plate 7 shows the melting of the crystallites at about 269°C.

Sublimation of the guest-free host was observed starting at about 190°C on the Hotstage, while the peak C appears on the DSC trace between 184-195°C. This suggests that peak C is associated with sublimation of the host. Yet no mass loss was observed in the TG experiments around this temperature. No physical explanation can be given for the diffused step B observed at 158°C in the DSC trace.

Attempts have been made to combine the DSC experiment with Microscopy using a sample of crystals of 0.05-0.1mm in diameter of mass 4-6mg. By replacing the swing-away enclosure cover on the sample holder of the DSC with a thick glass plate (18mm), we can use a microscope to observe the crystals, which were subjected to heating in the DSC sample holder. The thermal changes observed in the DSC trace were photographed by a camera mounted on the microscope. This had been done in order to correlate the observed phenomena using the HSM with the DSC onset temperatures. The photographs are not as clear as those obtained from the HSM, mostly due to the host sublimation and recrystallization onto the glass cover. We were able to observe the guest loss and sublimation before host melting. This experiment verified that peak C was correctly attributed to the sublimation of the host. No other visible phase changes could be attributed to peak C.

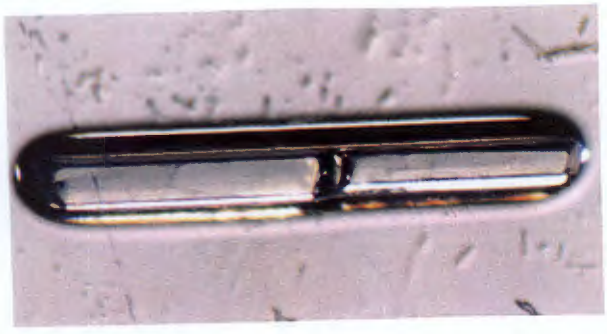

1. Crystal of **DACH**, with polarised light, at room temperature.

2. At 60°C, the crystal is turning opaque. Only bottom light on.

3. At 160°C, the crystal is completely opaque with its shape maintained. Only top light on.

4. Sublimation commenced at 190°C. Only bottom light on.

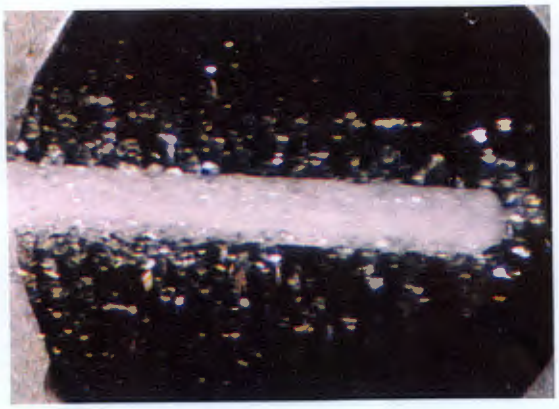

5. At 230°C, it continues to sublime and recrystallise. Only top light on.

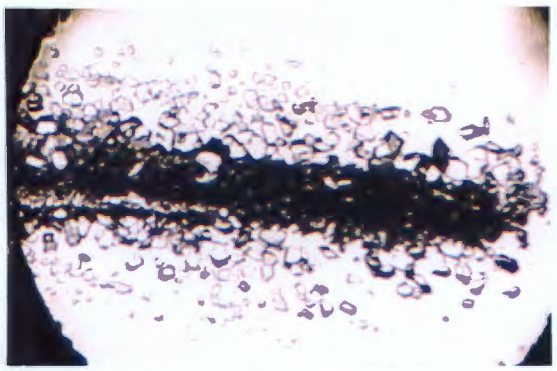

6. At 265°C, more tiny crystals have formed. Only bottom light is on.

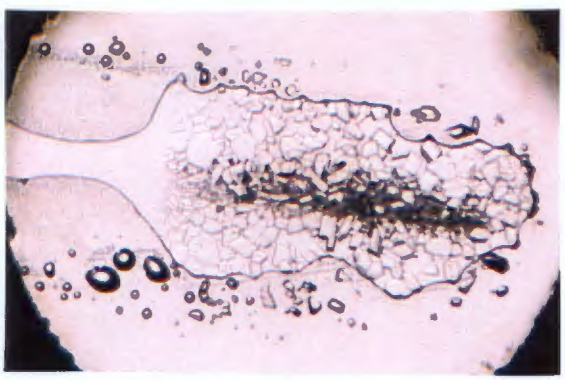

7. The crystals start melting at 269°C.

Plate 4.1 Hotstage microscope photographs for crystal of **DACH**. 20 x enlarged.

4.3.2. DA2M, DA3M and DA4M

The TG and DSC plots of inclusion compounds **DA2M**, **DA3M** and **DA4M** are illustrated in **Figure 4.3**.

From the analysis of TG plots, these three compounds have 1:2 host:guest ratios and lose their guests in a single step. At approximately 258°C the weight % start to decrease again and this is attributed to host sublimation and decomposition. The TG results for all four compounds in this study are summarised in **Table 4.1**.

Table 4.1 Determination of inclusion compounds stoichiometry by TG

Compound	Temp.range (°C)	Wt.loss (%) (exp.)	Wt.loss (%) (calc.)	H : G
DACH	68.6 - 128.3	34.3	35.0	1 : 2
DA2M	40.2 - 96.2	37.7	38.1	1 : 2
DA3M	43.5 - 97.2	37.8	38.1	1 : 2
DA4M	52.5 - 117.2	37.9	38.1	1 : 2

The DSC traces of **DA2M**, **DA3M** and **DA4M** show similar results to that exhibited by compound **DACH**. The first endothermic peak A corresponds to single step guest release observed in the TG with onset temperatures of 81.4, 80.3 and 108.9°C respectively. The last endothermic peak D is attributed to the melting of guest-free host, which occurred in all four compounds at 256-262°C. Both the DSC traces of **DA2M** and **DA4M** show the presence of diffuse peaks (C) with onset temperatures of 212.6°C and 215.8°C respectively. This is similiar to the peak C observed in **DACH**. For **DA3M**, no such thermal event was observed in the DSC trace. A step (B) in the baseline was observed after the peak A at 157, 146 and 165°C for **DA2M**, **DA3M** and **DA4M**, respectively, which is similar to the observation in **DACH**. The DSC results for all four compounds are summarised in **Table 4.2**. Only the enthalpy change, ΔH, of

the guest release and host melting are reported, for both their peaks are sharp and easily distinguished. Since all four inclusion compounds collapse back to the α-phase upon guest release (see Chapter 3), the state of the host after guest release should be the same. Accordingly ΔH values of guest release are normalised based on their melting point enthalphies. The normalised values are shown in Table 4.2.

Table 4.2 DSC results for the four inclusion compounds under study.

Compound	Peak	T_{on} (°C)	T_{on}-T_b (°C)*	ΔH (kJ/mol)	ΔH(kJ/mol)* (normalised)
DACH	A	128.5	-27.1	35.5	35.5
	B	158			
	C	184.2			
	D	260.5		43.4	
DA2M	A	81.4	-81.1	41.7	39.1
	B	157			
	C	212.6			
	D	262.0		46.2	
DA3M	A	80.3	-88.2	48.8	53.5
	B	146			
	D	256.8		39.6	
DA4M	A	108.9	-61.1	52.7	51.5
	B	165			
	C	215.8			
	D	262.7		44.4	

*For guest release only

One might expect to observe a correllation between the values of T_{on}-T_b and the values of ΔH for the guest release reactions of all four inclusion compounds. The nomalised ΔH values in Table 4.2 show that there is no such correlation. The trend in order of increasing enthalpy change of the guest release reactions was as follows: **DACH** ≅ **DA2M** < **DA4M** ≅ **DA3M**.

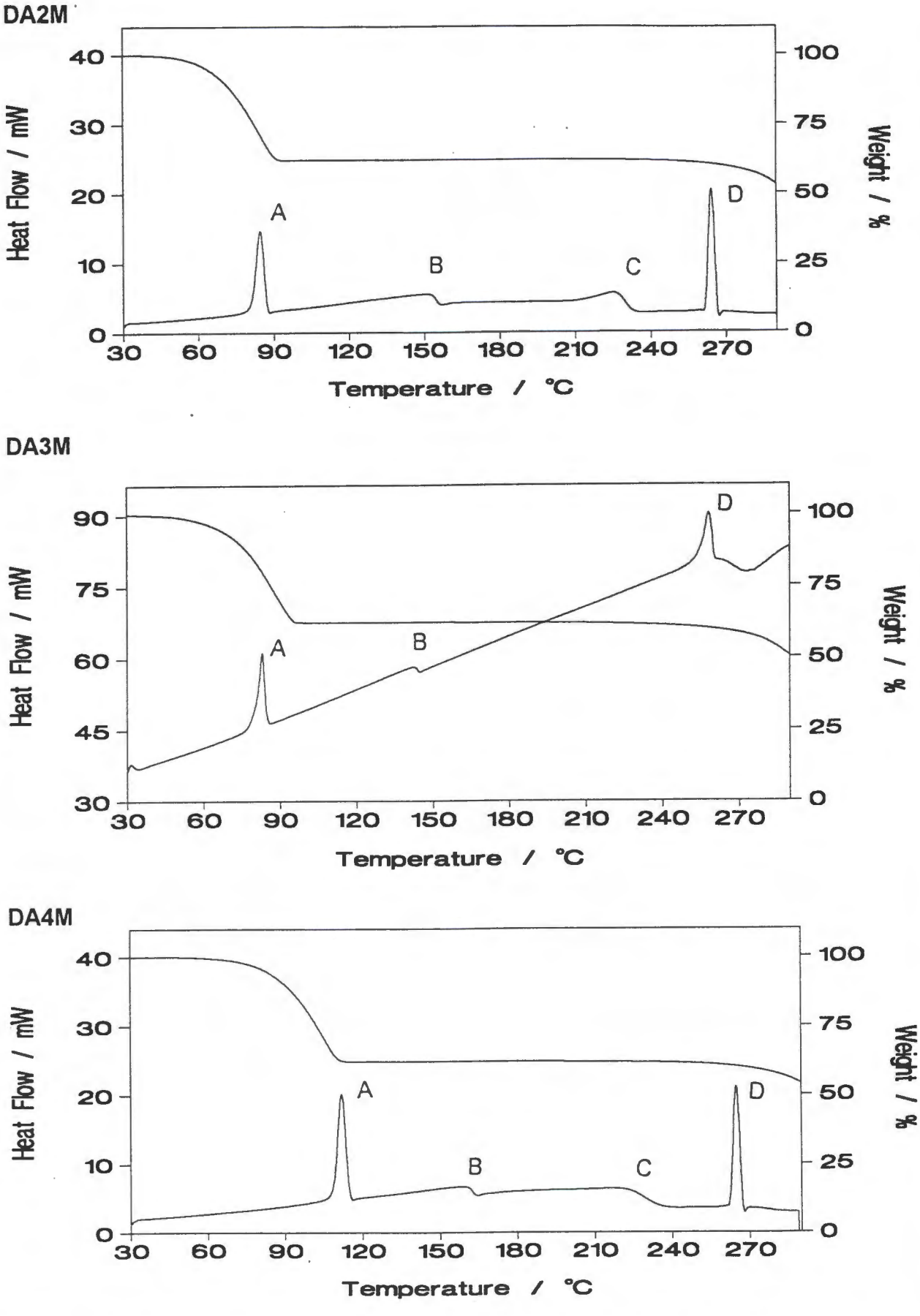

Figure 4.3 TG and DSC curves of compounds **DA2M**, **DA3M** and **DA4M**.

Crystals of **DA2M**, **DA3M** and **DA4M** were observed on the Hotstage. Their crystals were placed between two thin glass slides and subjected to heating at controlled heating rates as stated previously. These photographs are shown in **Plate 4.2**, **4.3** and **4.4** respectively. It is clearly seen that a very similar sequence of thermal events as that for the crystal of **DACH** was observed. The crystals often change slowly from clear to opaque in the temperature ranges of guest release. Sublimation accompanied by recrystallization of the host initially commenced at about 215°C, 210 °C, 220 °C for **DA2M**, **DA3M** and **DA4M**, respectively. Finally the desolvated substance melted at about 269°C.

Based on the observations from the Hotstage, we can attribute peak C, observed on the DSC for **DA2M** and **DA4M**, to the sublimation and accompanied recrystallization of the desolvated host DDDA. Though the corresponding temperatures are slightly lower than that at which the changes were observed on the Hotstage. This is mainly due to the particle size differences, entirely different geometries, and different operating conditions of the two experiments.

For **DA3M**, the phenomenon of sublimation and recrystallization of the desolvated host was observed on the Hotstage, as is the case for the other three compounds. No peak corresponding to this thermal event was observed in the DSC trace. This is may be due to that peak C for **DA3M** is too diffused to be observed, using the current experimental conditions.

Yet, no visible thermal events could attributed to the step B observed in the baseline after peak A in the DSC traces for the three compounds.

1. Crystal of **DA2M**, at 30°C.

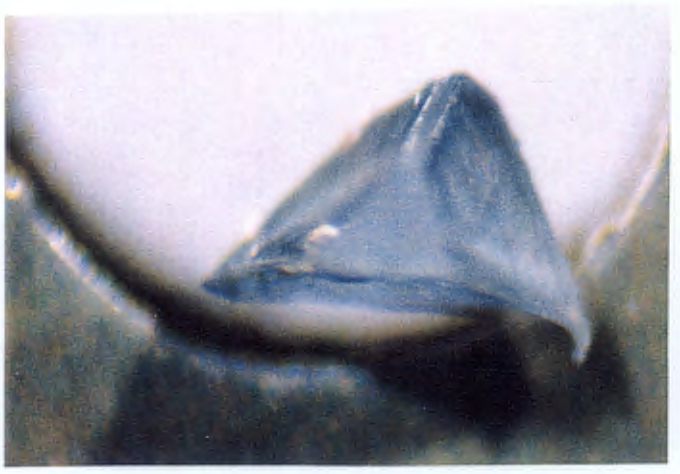

2. At 150°C, the crystal is opaque, with its shape retained.

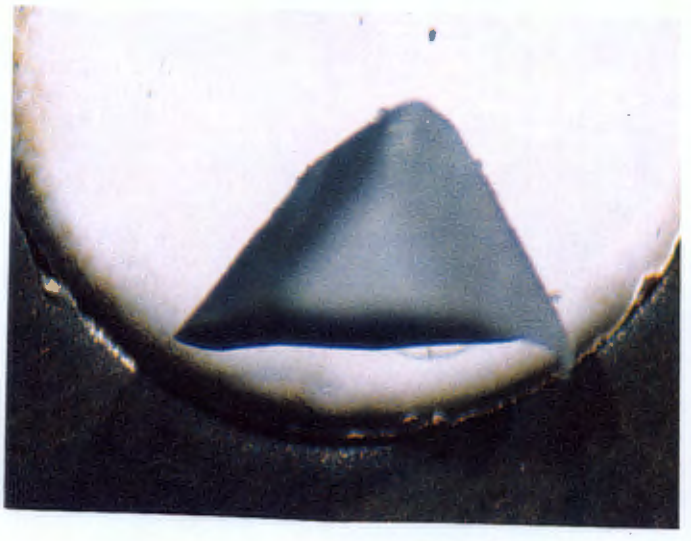

3. At 255°C, the sublimed crystal has formed many tiny crystals. Sublimation commenced at about 215°C.

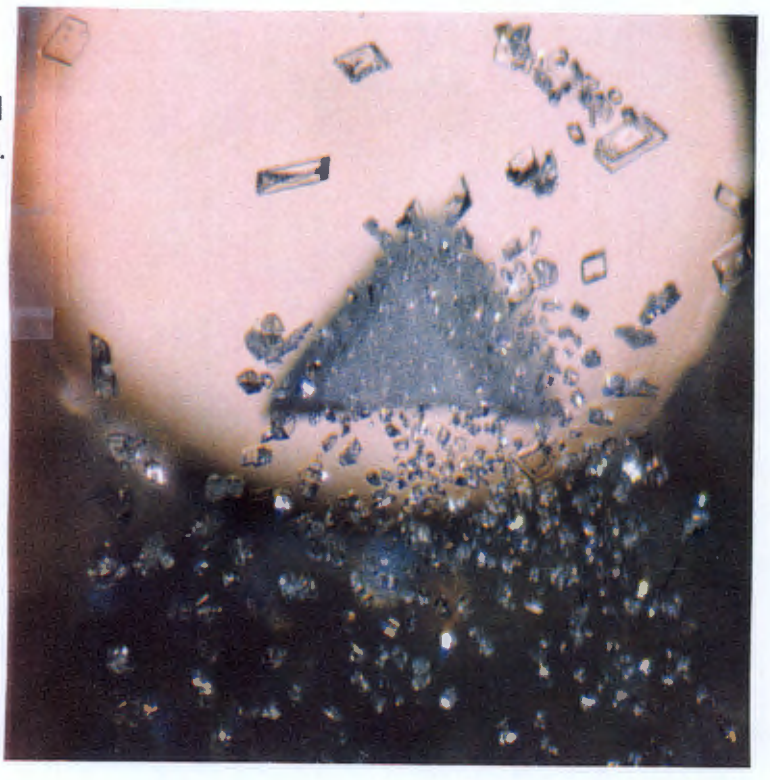

Plate 4.2 Hotstage microscope photographs for crystal of **DA2M**. 30 x enlarged.

1. Crystals of **DA3M** at 40°C.

2. At 80°C, the crystals are turning opaque.

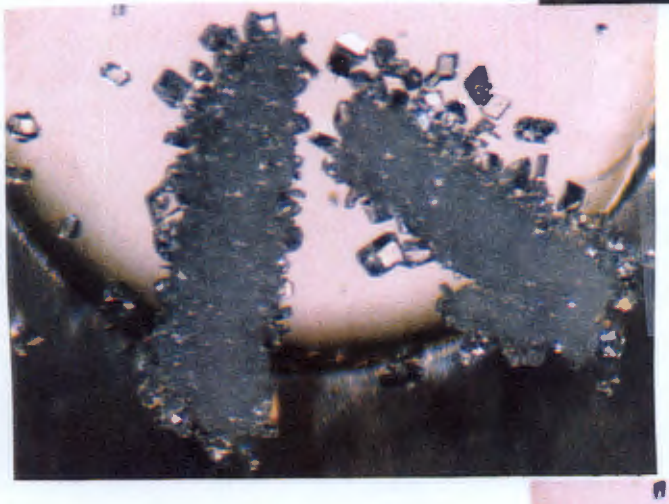

3. At 250°C, the crystals recrystallise to form many tiny crystals. Sublimation commenced at about 210°C.

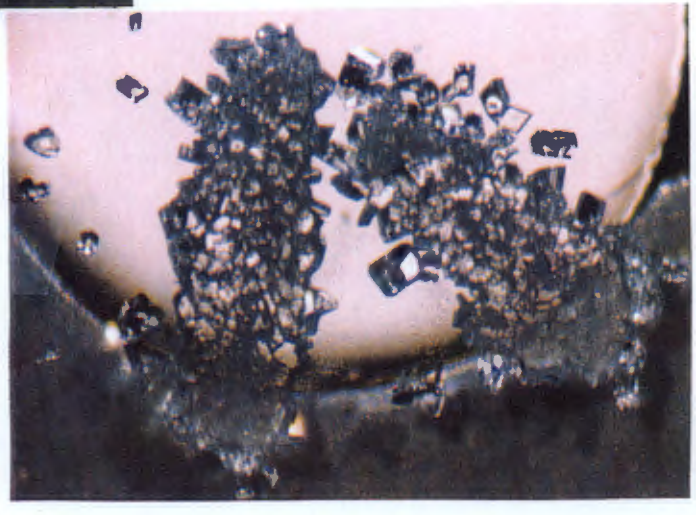

4. At 268°C, just before the melting of the crystals.

Plate 4.3 Hotstage microscope photographs for crystals of **DA3M**. 30 x enlarged.

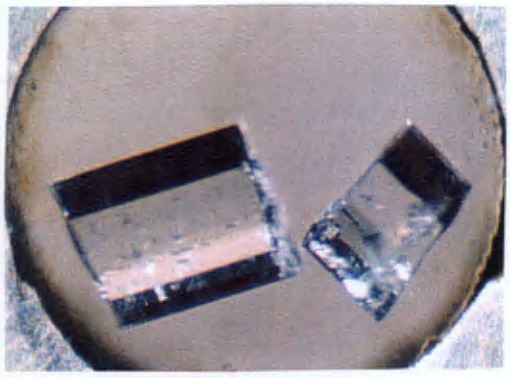

1. Crystals of **DA4M** at room temperature.

2. At 60°C, the crystals are turning opaque.

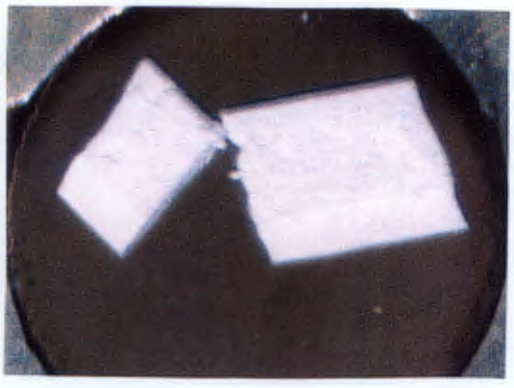

3. At 130°C, the crystals are completely opaque.

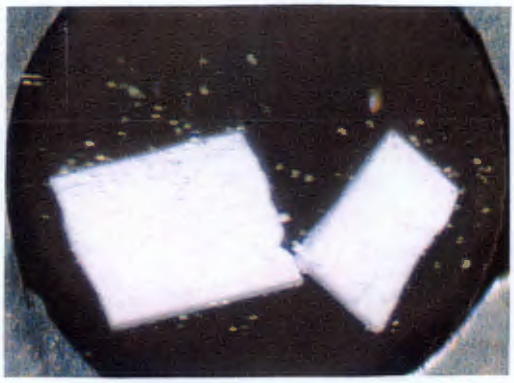

4. At about 220°C, the crystals sublimation commences

5. At 250°C, the sublimed crystals recrystallised and have formed many tiny crystals.

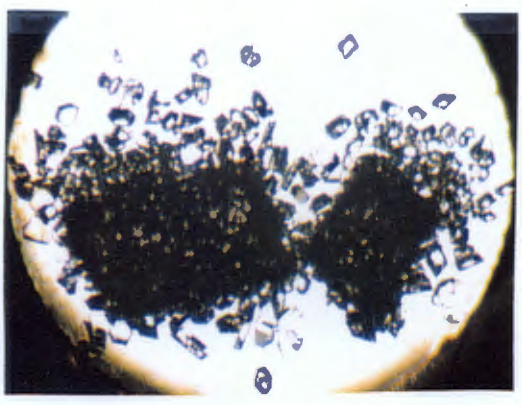

6. More tiny crystals formed at 266°C, just before the melting which starts at about 269°C. Only bottom light is on.

Plate 4.4 Hotstage microscope photographs for crystals of **DA4M**. 20 x enlarged.

4.4. Discussion

The TG results show all the four inclusion compounds under investigation have host:guest ratios of 1:2 and lost their guests in one single step. The DSC curves were mainly characterised by two sharp peaks, the first peak (A) for guest release and the last peak (D) for the melting of the residual host compound. A third diffused peak (C) between the above mentioned two peaks was observed in **DACH**, **DA2M** and **DA4M**, and can be due to sublimation of the sample based on the observation from the Hotstage. HSM on all four compounds showed very similar thermal changes. The guest release showed a slow change in the crystal from clear to opaque in the temperature ranges of guests loss, followed by sublimation with recystallization of the desolvated guest-free host, then a melting at around 269°C. In the case of **DA3M** no peak corresponding to the sublimation was observed in the DSC curve.

The DSC experiments resulted in the determination of the onset temperature, T_{on}, and enthalpy changes, ΔH, of guest release. For all four compounds, T_{on} is lower than T_b ($T_{on} < T_b$). There are examples of inclusion compounds of the same host DDDA with $T_{on} > T_b$. For example, inclusion compound involving actone showed the value of T_{on}-T_b is +14.2°C[12]. In case like this, an increase in T_{on}-T_b was often accompanied by an increase in ΔH. It was suggested that T_{on}-T_b can be used as a measure of relative thermal stability[11], when comparing inclusion compounds of the same host with similar guests. From Table 4.2, **DACH** has the largest value of T_{on}-T_b, while **DA3M** and **DA2M** have similar smaller values. Using this as an indicator the trend in order of increasing thermal stability was observed as follows:

DA3M ≅ **DA2M** < **DA4M** < **DACH**.

The same trend is not observed when comparing ΔH values.

References

1. E. L. Charsley and S. B. Warrington (eds.), 'Thermal Analysis, Techniques and Applications', Royal Society of Chemistry, London, 1992.
2. M. E. Brown, 'Introduction To Thermal Analysis', Chapman & Hall, London, 1988.
3. R. L. Fyans, W. P. Brennan and C. M. Earnest, *Thermochim. Acta*, 92, 1985, p385.
4. W. W. Wendlandt, 'Thermal Analysis', 3rd edn., Wiley, New York, 1986.
5. M. Kuhnert-Brandstatter and F. Proll, *Mikrochim. Acta,* 3, 1983, p287.
6. M. H. Moore, L. R. Nassimbeni and M. L. Niven, *Inorg. Chem. Acta.* 131, 1987, p45.
7. M. R. Caira, L. R. Nassimbeni, N. Winder, E. Weber and A. Wierig, *Supramol. Chem.*, 4, 1994, p135.
8. L. J. Barbour, M. R. Caira, A. Coetzee and L. R. Nassimbeni, *J. Chem. Soc. Perkin Trans* 2, 1993, p1345.
9. M. E. Brown and A. K. Galwey, *Anal. Chem.*, 61 1989, p1136.
10. A. P. Salvador and E. G. Galvo, *Thermochim. Acta*, 203, 1992, p503.
11. M. R. Caira and L. R. Nassimbeni, in 'Comprehensive Supramolecular Chemistry', Vol 6, 'Solid-state Supramolecular Chemistry: Crystal Engineering', D. D. MacNicol, F. Toda and R. Bishop (Volume Editors), Pergamon Press, 1996, chpt 25.
12. L. J. Barbour, M. R. Caira and L. R. Nassimbeni, *J. Chem. Soc. Perkin Trans* 2, 1993, p2321.

CHAPTER 5

CRYSTAL STRUCTURE

5. CRYSTAL STRUCTURE

In this chapter, the crystal structures of the four inclusion compounds between the host **DDDA** and the guest cyclohexanone and its three methyl isomers are discussed. A description of the structure solution and refinement of **DACH** and **DA3M** will be given. Their structures are compared with those of **DA2M** and **DA4M**, of which the atomic co-ordinates were extracted from Cambridge Structural Database System (CSDS)[1], and which have been solved and refined by D.R. Bond *et al* [2].

5.1. Structure Solution and Refinement

Both the structures of **DACH** and **DA3M** were solved using the direct methods package SHELXS-86[3] and refined on F^2 using SHELXL-93[4]. The host **DDDA** numbering scheme is shown in **Figure 5.1**. The crystallographically independent guest molecules are assigned numeric suffixes after the letter "G". For each compound the molecular formula, space group and cell geometry are summarised together with the guest labelling scheme.

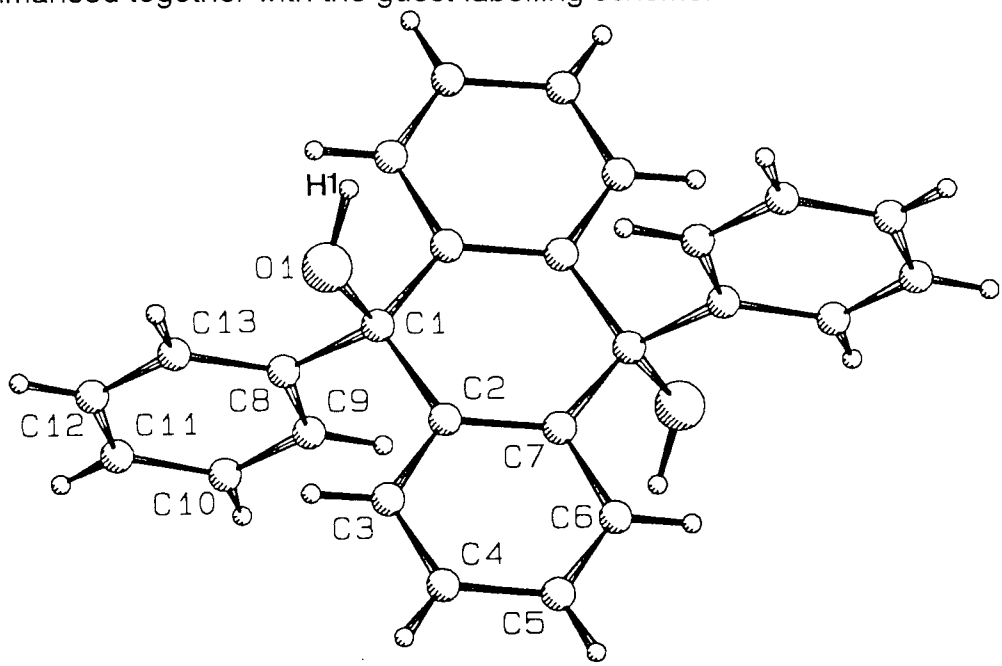

Figure 5.1 Host DDDA atomic numbering scheme. To simplify the picture only the hydroxyl hydrogen is labelled. The other hydrogen atoms are numbered according to the carbon to which they are bonded, e.g. H(4) is bonded to C(4).

5.1.1. DACH

$C_{26}H_{20}O_2 \cdot 2(C_6H_{10}O)$

Guest: Cyclohexanone

Space group: P $\bar{1}$

a = 8.741(3) Å α = 112.30(6)°

b = 9.008(3) Å β = 93.290(5)°

c = 10.863(7) Å γ = 101.14(3)°

V = 768.5(4) Å^3

Z = 1

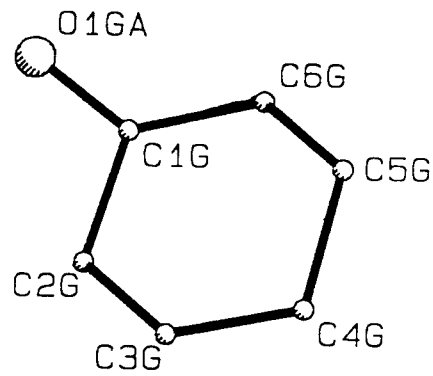

Guest molecule numbering scheme

A host:guest ratio of 1:2 was established by TG (see chapter 4, Table 4.1). Preliminary oscillation and Weissenberg photography indicated that **DACH** belongs to the triclinic crystal system. The centrosymmetric space group P $\bar{1}$ was assigned based on the mean $|E^2-1|$ values obtained from direct methods, and this was vindicated by the successful refinement of the structure. Determination of the unit cell volume suggested that one host molecule and 2 guest molecules are located in the unit cell, with Z = 1.

All non-hydrogen atoms of the host molecule were located using direct methods. The guest non-hydrogen atoms were located in the difference electron density map, upon subsequent refinement. Since Z = 1, the host:guest ratio is 1:2, symmetry requires the host to be located at a special position and the guest molecule to be located in a general position. The host molecule was placed with its molecular centre at the centre of inversion, at Wyckoff position *h*. Because of the centrosymmetry, only half a host molecule and one whole guest molecule were placed in the asymmetric unit, the other atoms of the unit cell were generated via the centre of inversion.

Analysis of the difference electron density maps showed that the carboxyl oxygen on the guest molecule was disordered as depicted in **Figure 5.2**. The oxygen atom was modelled in two positions, O(1GA) and O(1GB) attached to

C(1G) and C(2G) with fractional site occupancy factors of 0.6 and 0.4 respectively. The assignment of site occupancy factors was based on the relative peak heights in the electron density map.

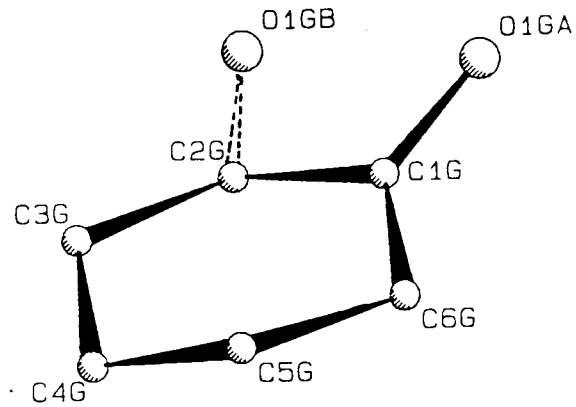

Figure 5.2 Disorder modelled in guest cyclohexanone.

Both the host and the guest non-hydrogen atoms were treated anisotropically in the final model. The aromatic hydrogen atoms on the host molecule were placed with geometric constraints, using the build-in function in SHELXL-93, for idealised aromatic CH groups, and assigned a common isotropic temperature factor, but the co-ordinates were allowed to refine freely. The hydroxyl hydrogen atom H(1) on the host was independently located in the difference electron density map, and then refined with simple bond length constraints at a value of d[O(1)-H(1)] = 0.975Å. Typical O-H bond lengths were obtained by extrapolation from a plot of O-H versus O···O distances for a large number of crystal structures[5]. The distance of 0.975Å was thus arrived at, by calculating the average O···O distance between O(1)···O(1GA) and O(1)···O(1GB) respectively. The constraints placed on the distances are summarised in a schematic representation of the disorder, shown in **Figure 5.3**. The refined H(1) details are given in **Table 5.1**.

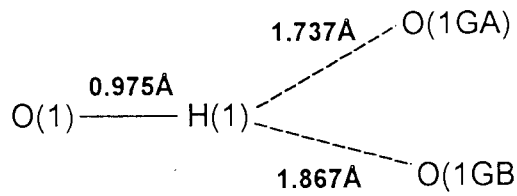

Figure 5.3 Schematic diagram showing the bond length constraints on O-H.

Owing to the guest disorder, no attempt was made to place the guest hydrogen atoms. A residual electron density of 0.46 eÅ^{-3} was observed in the region of the guest. The structure refined successfully to R_1 = 0.0797. All bond lengths and angles of the host and guest molecules were in acceptable ranges[6].

Crystal data, data collection and final refinement parameters of **DACH** are given in **Table 5.2**, appearing at the end of this chapter. Final fractional atomic co-ordinates, temperature factors, table of bond lengths and angles, and torsion angles are in **Appendix B**. Tables of observed and calculated structure factors are contained in **Appendix C**.

5.1.2. DA3M

$C_{26}H_{20}O_2 \cdot 2(C_7H_{12}O)$

Guest: 3-methylcyclohexanone

Space group: P $\bar{1}$

a = 9.171(6) Å α = 93.82(2)°

b = 9.692(3) Å β = 104.93(4)°

c = 10.359(2) Å γ = 112.54(4)°

V = 807.5(6) Å^3

Z = 1

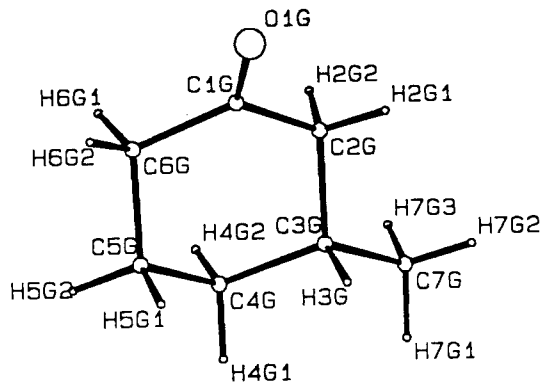

Guest molecule numbering scheme

A host:guest ratio of 1:2 was established by TG (see chapter 4, Table 4.1). The triclinic crystal system was indicated by preliminary X-ray photography. The mean $|E^2-1|$ values obtained by direct methods indicated that the space group is P $\bar{1}$, and this was confirmed by the successful refinement of the structure. Determination of the unit cell volume suggested one whole host and two guest molecules are located in the unit cell, with Z = 1.

Direct methods yielded the positions of all the host non-hydrogen atoms. The guest molecule was located in the difference electron density map, upon subsequent refinement. Because there is one host and two guest molecules

per unit cell, symmetry requires the host molecule to be located with its molecular centre at a centre of symmetry. The host was placed on a special position, at Wyckoff position *f*. The guest molecule was located in a general position.

Refinement of the all non-hydrogen atoms was carried out with them treated anisotropically. The host hydroxyl hydrogen atoms were located in the difference electron density map and refined with bond length constraints of d[O(1)-H(1)] = 0.96Å and individual temperature factors[5]. The rest of the host hydrogen atoms and the guest methylenic and methylic hydrogen atoms were placed with geometric constraints and refined with common isotropic temperature factors for similar hydrogen atoms. The host aromatic hydrogen atoms were treated as idealised aromatic CH groups; the guest methylenic hydrogen atoms were treated as idealised secondary CH_2 groups, which are approximately tetrahedral; the guest methylic hydrogen atoms were treated as an idealised CH_3 group with tetrahedral angles. A maximum residual electron density of 0.18 $eÅ^{-3}$ was observed. The structure refined successfully to R_1 = 0.0446. All bond lengths and angles of the host and guest molecules in this structure were all in acceptable ranges[6].

The 3-methylcyclohexanone guest in compound **DA3M** has a definite chair conformation (see **Figure 5.4**). The average internal torsion angles in the ring is 65°. The deviation of C(1G) and C(4G) from the least-squares plane through the starred atoms given as follows, confirms the chair conformation:

C(2G)*	C(3G)*	C(5G)*	C(6G)*	C(1G)	C(4G)
0.006	-0.006	0.006	-0.005	0.500	-0.657

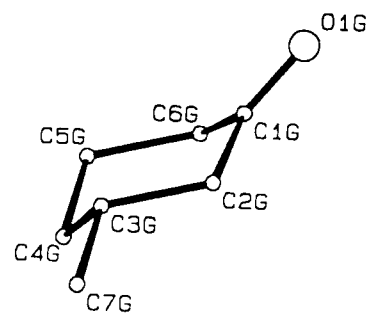

Figure 5.4 Chair conformation of the guest 3-methylcyclohexanone.

The crystal data, experimental and final refinement parameters for **DA3M** are given in Table 5.2 at the end of this chapter. Final fractional atomic co-ordinates, temperature factors, table of bond lengths and angles, and torsion angles are listed in **Appendix B**. Tables of observed and calculated structure factors are contained in **Appendix C**.

5.2. Molecular packing

5.2.1. DACH

The interaction between the molecules in the crystal was observed as following: each one of the two hydroxyl groups on a host molecule formed a hydrogen bond with the ketonic group on a guest molecule. The hydrogen bonding details are given in Table 5.1 which is a summary of all four inclusion compounds under study. A stereoscopic view of the molecular structure is shown in **Figure 5.5**, in which the guest is presented with its disordered model. The hydrogen bonding scheme is indicated with dotted lines. A projection of the crystal packing viewed along [010] and [001] is shown in **Figure 5.6** a) and b) respectively.

Table 5.1. Details of hydrogen bonding observed in the inclusion compounds.

Compounds	O(1)···O(1G) (Å)	O(1)–H(1) (Å)	O(1)–H(1)···O(1G) (°)
DACH			
O(1G) = O(1GA)	2.701(3)	1.030(3)	145.2(3)
O(1G) = O(1GB)	2.821(3)		142.8(3)
DA2M *	2.894(4)	0.969 **	168.5(3)
DA3M	2.862 (3)	0.921(4)	166.7(4)
DA4M *	2.806(5)	0.975 **	148.6(3)

* taken from reference [2].
**Calculated from published data, no estimated standard deviations(esd) given.

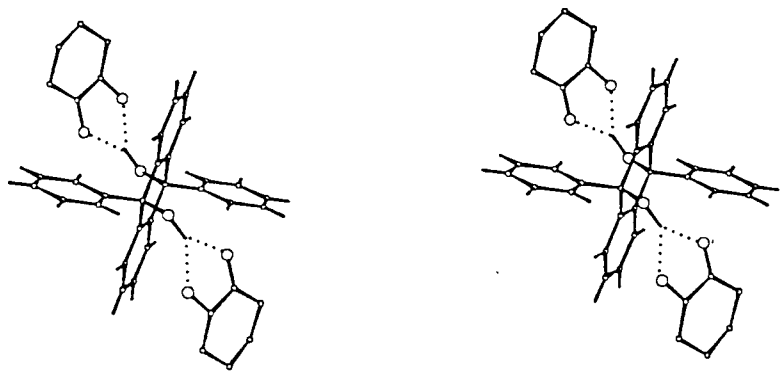

Figure 5.5 Stereoscopic view of **DACH** with the guest disorder modelled. The hydrogen bonds are indicated with dotted lines.

Analysis using the program MOLMAP[7] by cutting through the unit cell at given intervals, shows that the packing of host molecules results in the formation of a snakelike channel running parallel to [001], along which the guest molecules reside. The topologies of the channels can be seen in **Figure 5.7** a) when view down [010], where the area occupied by the host are represented by a hatched area, and the guest atoms are presented with van der Waals radii. These channels running along [001] are of diameter of ~5.5Å at the widest portions, and ~4.5Å at the narrowest. A view down these channels is shown in **Figure 5.7** b). The packing factor, calculated as the volume per non-hydrogen atoms, is 18.3Å^3.

a)

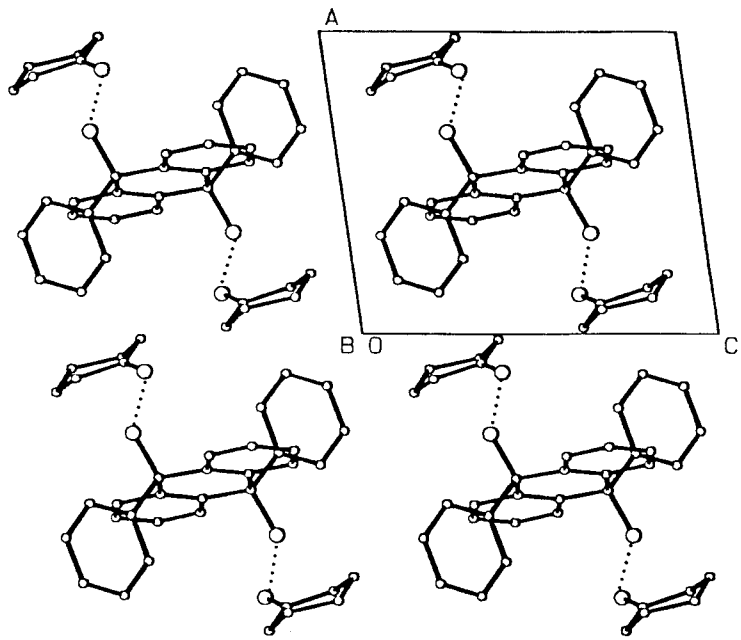

b)

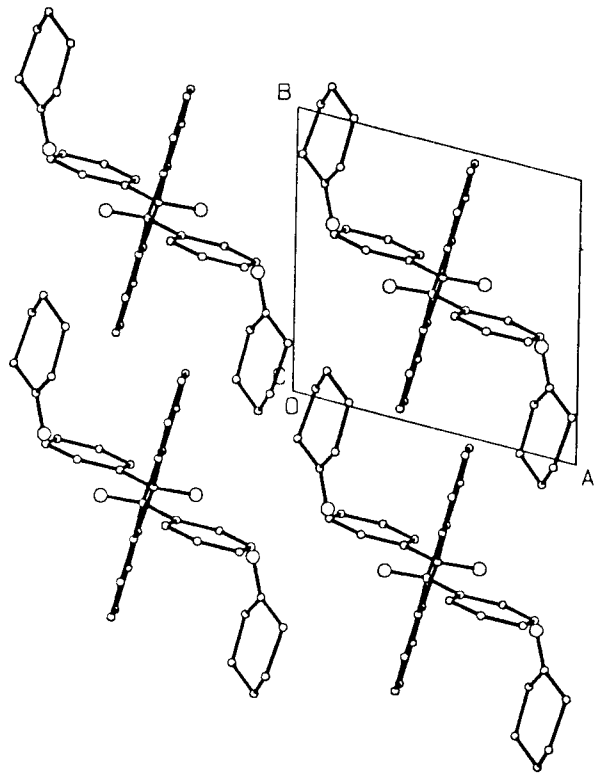

Figure 5.6 Projection down a) [010], b) [001], showing the crystal structure of **DACH**. The guest molecules are only shown with O(1GA). For clarity hydrogen atoms are omitted. In a) the hydrogen bond contacts bewteen O···O are indicated as dotted lines.

a)

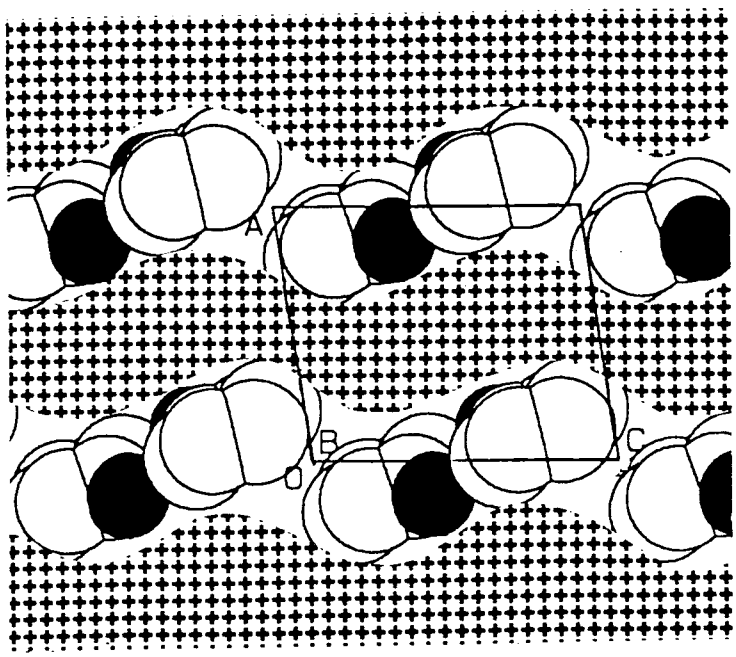

b)

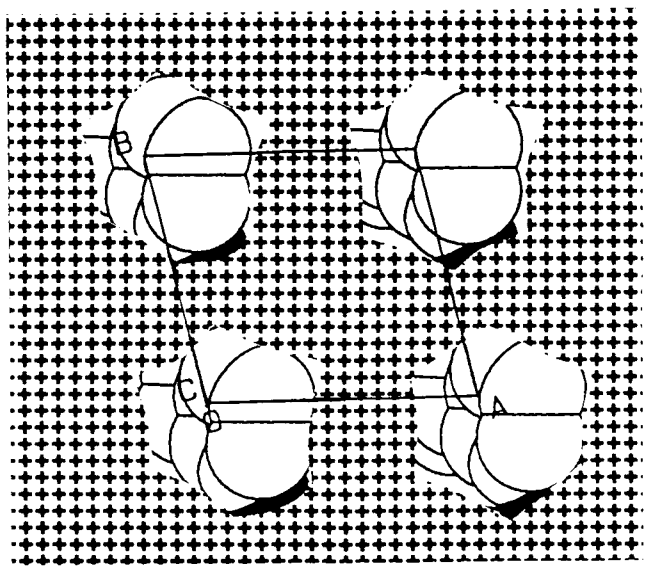

Figure 5.7 A cross section of the host molecules of **DACH**, viewed down a) [010], cut at y = 0 and b) [001], cut at z = 0.7, showing channels parallel along [001]. The hatched area represents a cross section of the host framework, while the guest is presented with van der Waals radii with oxygen atoms shaded.

5.2.2. DA3M

The interaction in the crystal of **DA3M** is similar to that of **DACH** described previously. The two guest molecules are hydrogen bonded to the two hydroxyl groups of the host molecule. The hydrogen bonding scheme is shown in **Figure 5.8**. The crystal packing, viewed down [100] and [001] are shown in **Figure 5.9** a) and b) respectively.

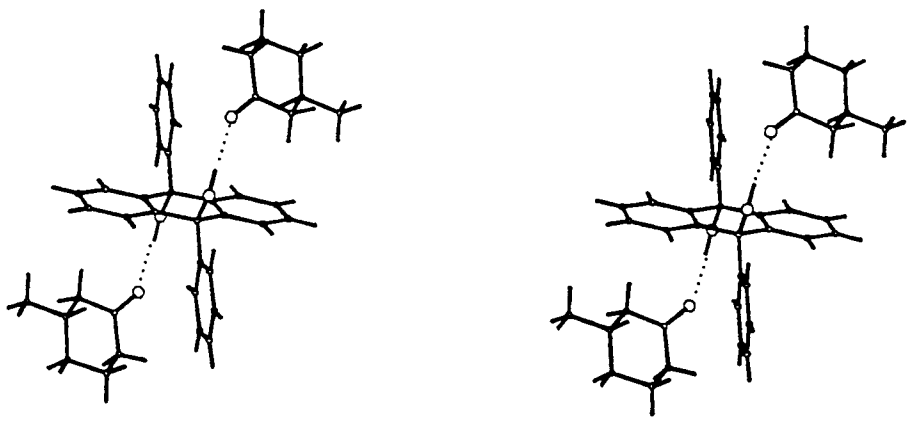

Figure 5.8 Stereoview of **DA3M** with dotted lines showing the hydrogen bonding scheme.

Upon investigating the molecular packing of the crystal **DA3M** using MOLMAP, it was found that the host molecules pack to form channel parallel to [001], in which the 3-methylcyclohexanone guest molecules reside, as can be seen in **Figure 5. 10** a). The channel has diameters of ~6Å at the widest portion, and ~5Å at the narrowest. A view down [001] in **Figure 5.10** b) shows that these channels are linked to one another along [100]. These constrictions are less than 2Å in diameter, hence the only channels in this structure are those parallel to [001]. The packing factor for this structure was found to be 18.4Å^3 / non hydrogen atom.

a)

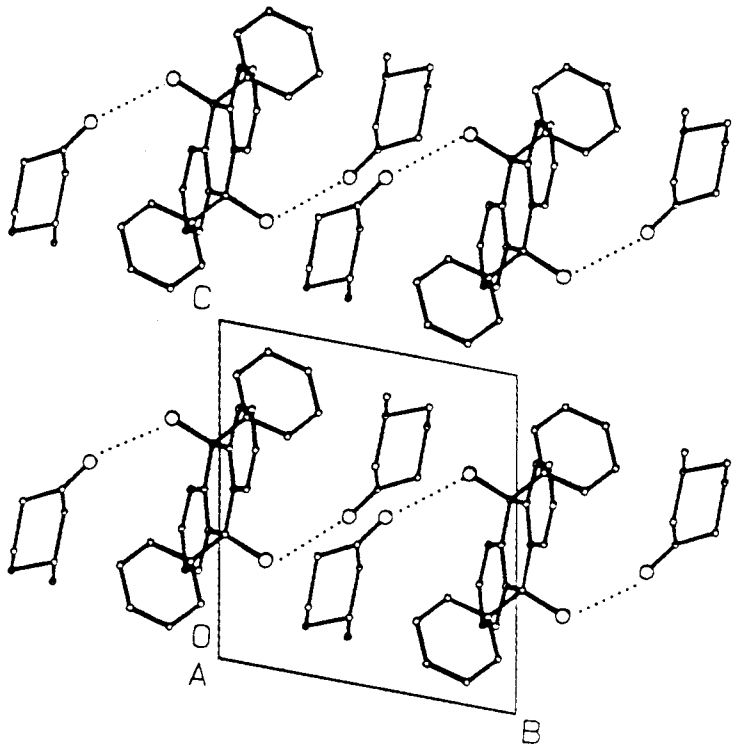

b)

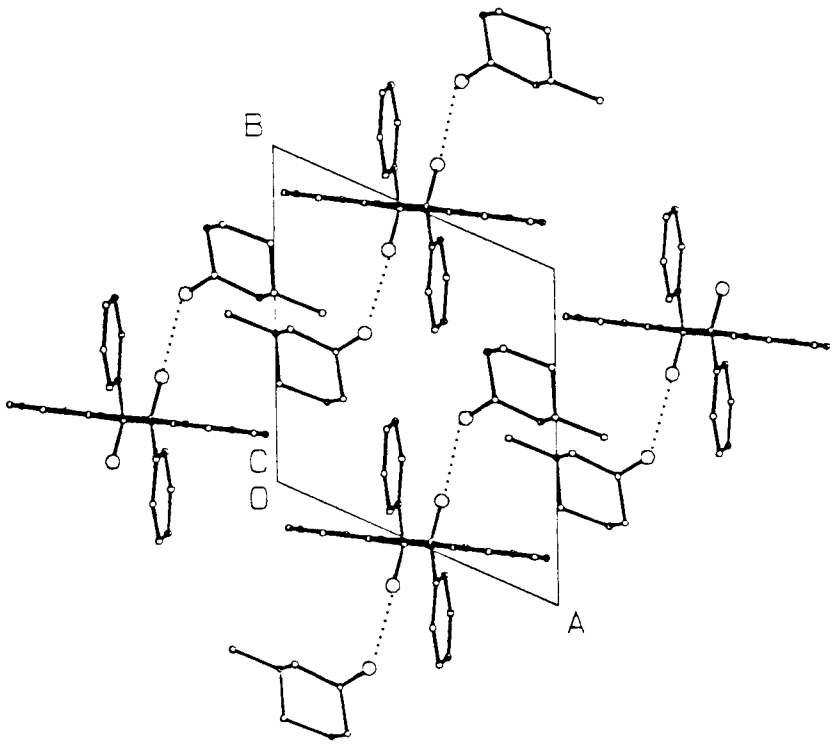

Figure 5.9 A projection viewed down a) [100] and b) [001] for **DA3M**. For clarity the hydrogen atoms are omitted. The hydrogen bond contacts between O···O are represented with dotted lines.

a)

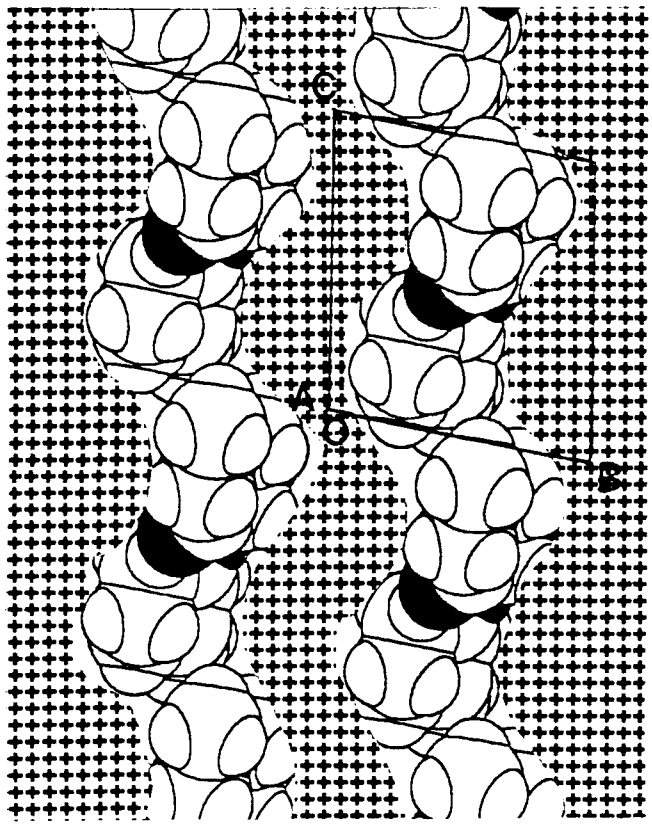

b)

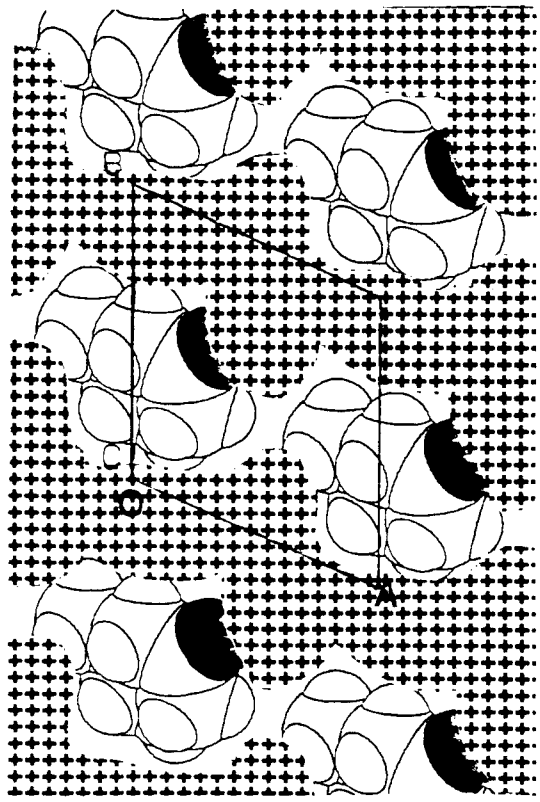

Figure 5.10 A projection of the crystal structure **DA3M**, a) viewed down [100], showing channels running along [001]; b) viewed down the channels running parallel to [001]. The hatched area represents a cross section of the host framework, cut at a) x = 0.1 and b) z = 0.3, while the guest is presented with van der Waals radii with oxygen atoms shaded.

5.2.3. DA2M and DA4M

The crystal structures of **DA2M** and **DA4M** were reported in reference [2]. their crystallographic data are summarised as follows:

DA2M		**DA4M**	
$C_{26}H_{20}O_2 \cdot 2(C_7H_{12}O)$		$C_{26}H_{20}O_2 \cdot 2(C_7H_{12}O)$	
Guest: 2-methylcyclohexanone		Guest: 4-methylcyclohexanone	
Space group: P $\bar{1}$		Space group: $P2_1/c$	
a = 8.917(3) Å	α = 68.72(2)°	a = 8.838(2) Å	α = 90°
b = 9.900(2) Å	β = 64.39(3)°	b = 8.92(1) Å	β = 98.67(2)°
c = 11.250(4) Å	γ = 74.86(2)°	c = 20.879(8) Å	γ = 90°
V = 828.1(5) Å^3		V = 1627(2) Å^3	
Z = 1		Z = 2	

* taken from reference [2].

DA2M has a host:guest ratio of 1:2 (see Table 4.1, Chapter 4). It crystallises in the space group P $\bar{1}$, and shows similar packing as **DACH** and **DA3M**. The molecular packing and hydrogen bonding scheme observed is shown in **Figure 5.11** and **5.12** respectively. Details of the hydrogen bonds are given in Table 5.1. Bond *et.al.*[2] reported that the guests are located in channels running parallel to [100], ranging in diameter between 4 and 7Å. Upon closer examination of the MOLMAP diagrams, the existence of additional channels running parallel to [010] was established. These channels range in diameter between 4 and 6Å. **Figure 5.13** a) and b) shows these channels running parallel to [010] and [100] respectively. The packing factor was calculated as 18.8Å^3 / non hydrogen atom.

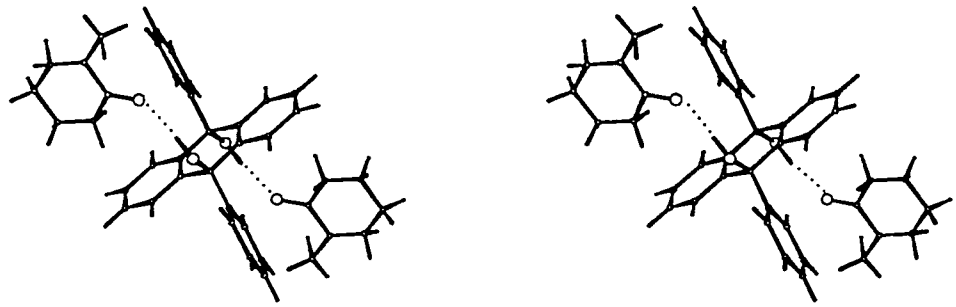

Figure 5.11 A stereoview of molecular structure of **DA2M**. The hydrogen bonds are represented as dotted lines.

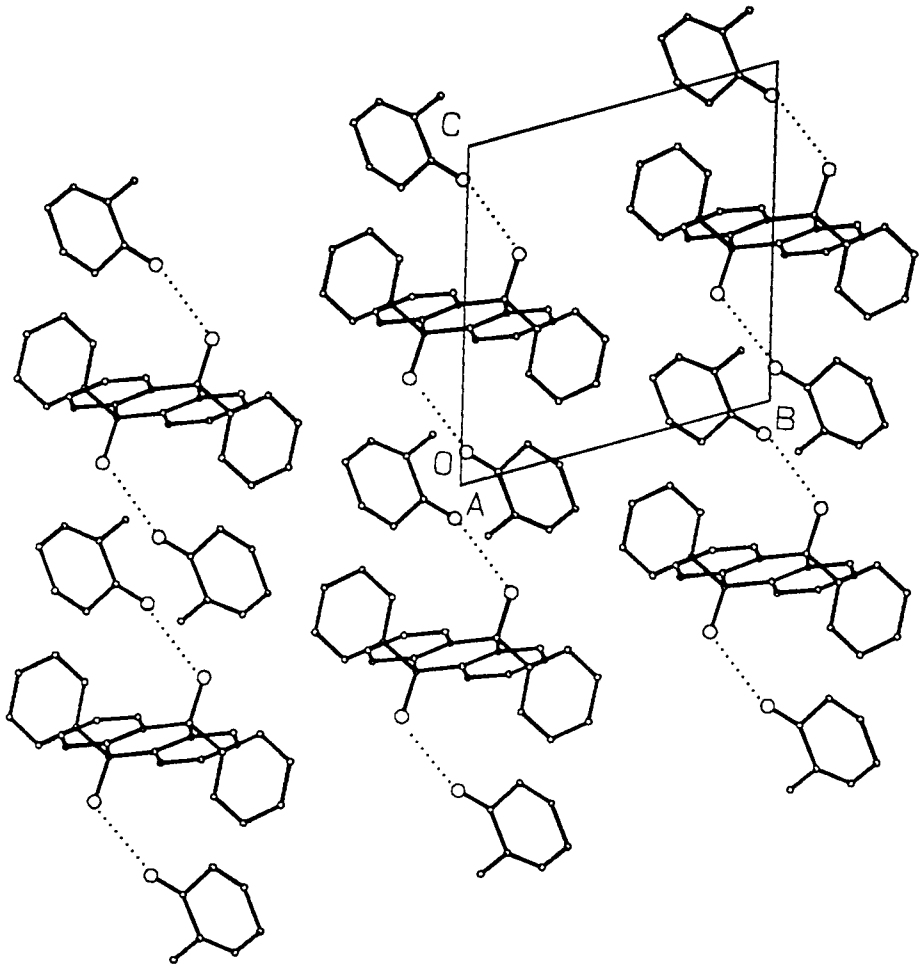

Figure 5.12 Crystal packing in **DA2M** viewed down [100]. The hydrogen atoms are omitted. The hydrogen bond contacts between O···O are shown with dotted lines.

a)

b)

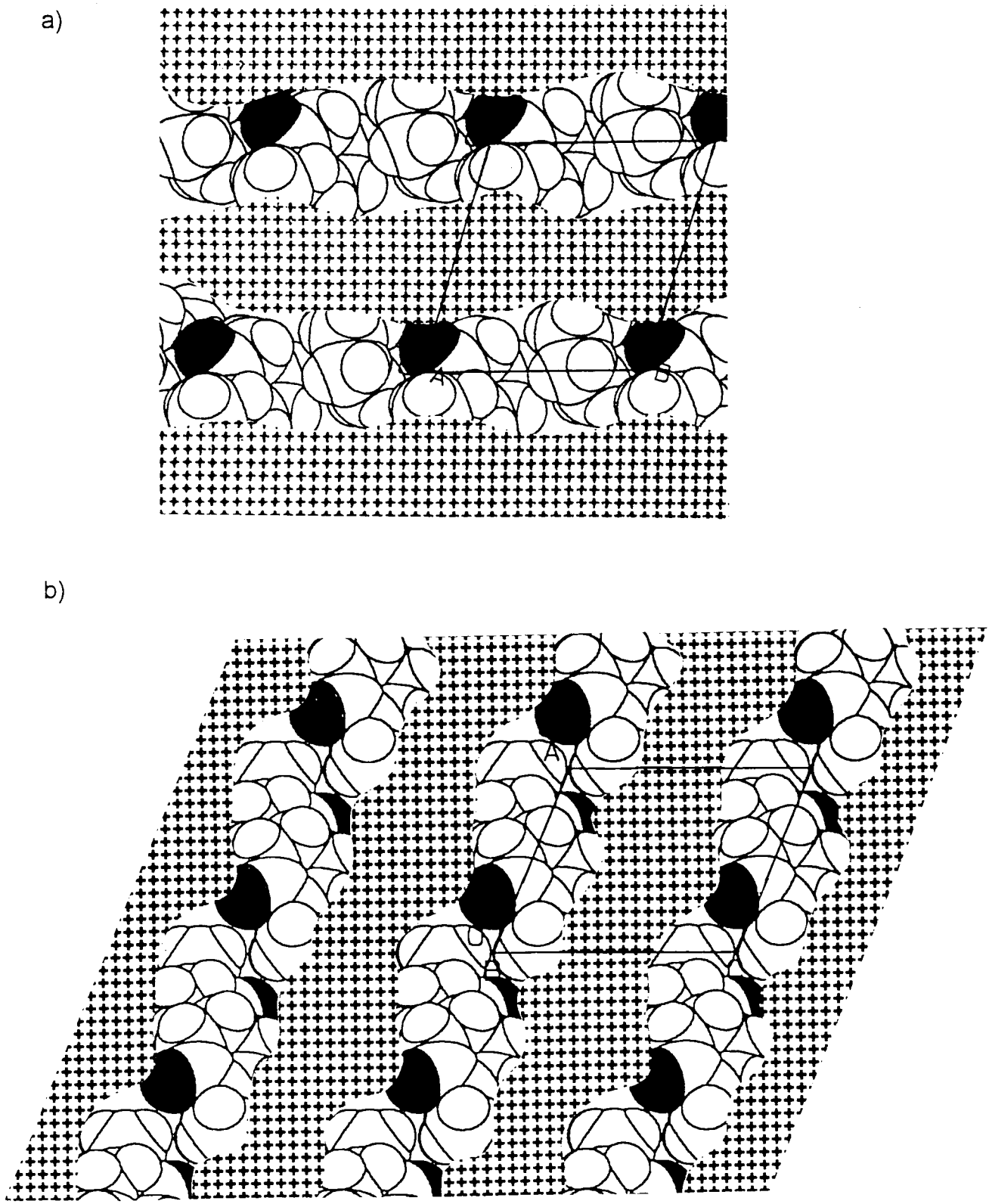

Figure 5.13 A projection of the crystal structure **DA2M**, viewed down a) [100] and b) [010], showing the guest molecules are located in channels running along [010] and [100] respectively. The hatched area represents a cross section of the host framework, cut at a) x = 0 and b) y = 0.1. While the guest is presented with van der Waals radii with oxygen atoms shaded.

TG yielded a host:guest ratio of 1:2 for **DA4M**. It crystallised in the space group $P2_1/c$ with Z = 2. A stereoview of the molecular structure is shown in **Figure 5.14**. The crystal packing, as viewed down [010], is shown in **Figure 5.15**. The 4-methylcyclohexanone guest molecules were found to be located in the channel running parallel to [001]. These channels have a diameter of ~6Å at the widest part, ~5Å at the narrowest part. A view down [001] shows that the host forms constrictions of 2Å along [010] (see **Figure 5.16** a)). Hence giving rise only to the channels running parallel to [001] (see Figure 5.16 b)). The packing factor for this structure was calculated to be 18.5Å^3 / non hydrogen atom.

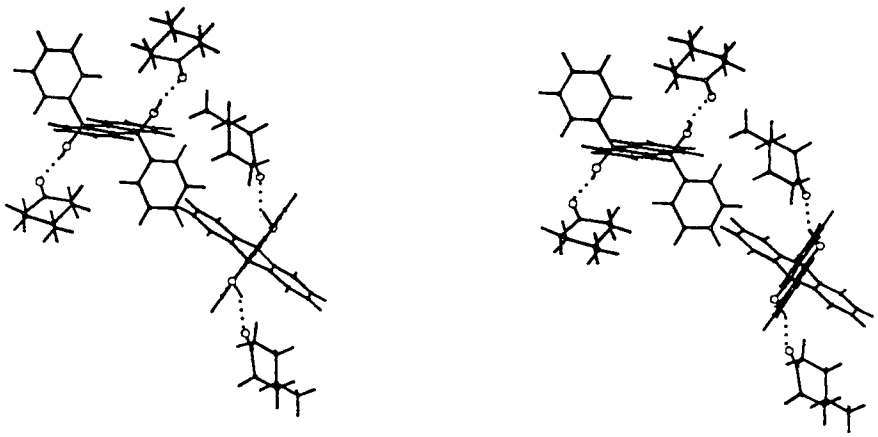

Figure 5.14 A stereoview of molecular structure of **DA4M**. The hydrogen bonds are indicated as dotted line.

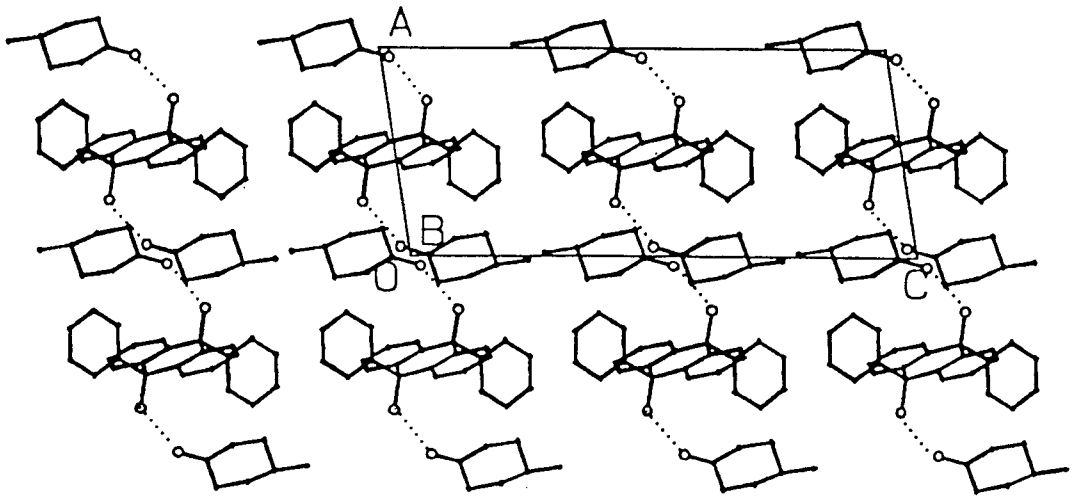

Figure 5.15 Projection of crystal packing in **DA4M** viewed down [010]. For clarity the hydrogen atoms are omitted. The hydrogen bond contacts between O···O are shown with dotted lines.

a)

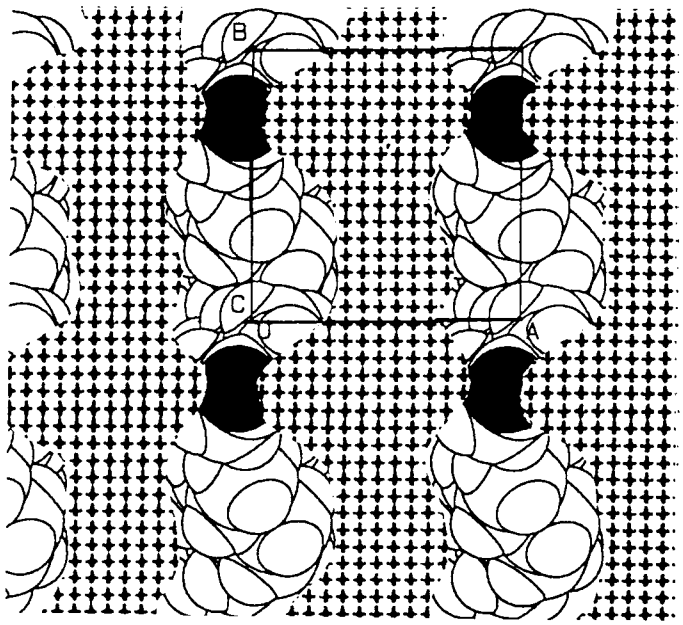

b)

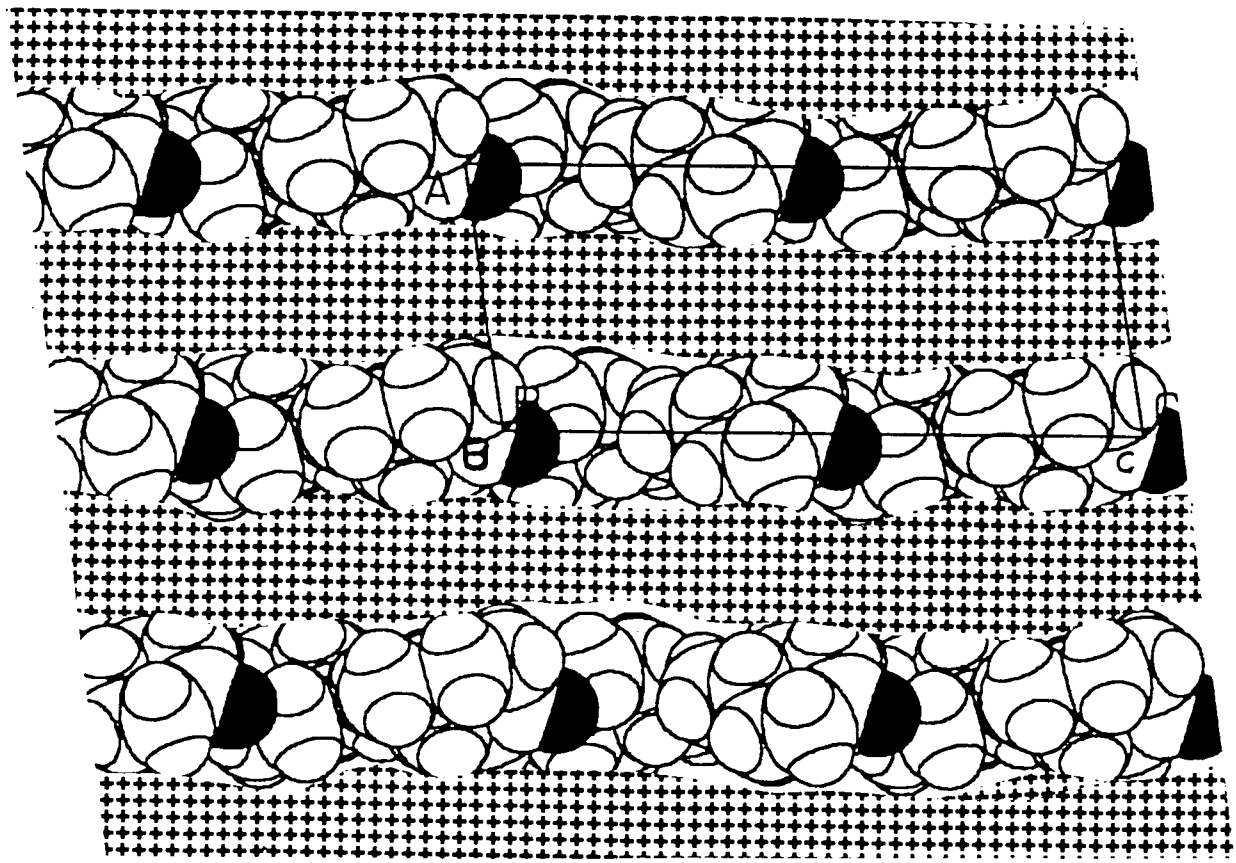

Figure 5.16 A cross section of the host molecules of **DA4M**, a) viewed down [001], cut at z = 0.65; b) viewed down [010], cut at y = 0.5, showing channels running parallel to [001]. The host frame-work is represented by hatched area, the guest is shown in van der Waals radii with oxygen atoms shaded.

5.3. Host conformation and packing

5.3.1. Host conformation

In all four structures, the host molecules were located at a centre of symmetry. For **DACH** and **DA3M**, the central 1,4-cyclohexadiene ring of the host possesses internal torsion angles of less than 2° and the maximum root mean squared (RMS) deviations from the least-squares plane through atoms C(1), C(2), C(7), C(1A), C(2A) and C(7A) are to within 0.02Å. Based on the work done by Duax and Norton[8], Schubert[9] suggested that RMS deviations of this ring with values of $d \geq 0.03$Å indicate significant deviation from planarity. The conformation of the tricyclic carbon skeletons of the host in the structures of **DACH** and **DA3M** are therefore planar as are those in the structures of **DA2M** and **DA4M**[2]. This was observed in all previously reported studies of **DDDA**[10-17] except one[18].

The phenyl substituents of the host molecules are planar, since the maximum RMS deviations from mean squares planes are to within 0.004Å and 0.008Å for **DACH** and **DA3M** respectively, and 0.006Å for both **DA2M** and **DA4M**[2]. These phenyl groups are perpendicularly orientated with respect to their tricyclic backbones making dihedral angles of 89.8°, 83.8°, 86.9° and 91.0° in structures of **DACH**, **DA3M**, **DA2M**[2] and **DA4M**[2] respectively.

The different bond types observed in the host compound are indicated schematically in **Figure 5.17**, and the range of bond lengths observed in each structure are summarised in **Table 5.3**. The host conformations for all four structures are very similar and may be described by means of the torsion angle which defined the orientation of the phenyl substituent groups and central tricyclic group. This torsion angle is C(2)-C(1)-C(8)-C(9) (τ), which is indicated in Figure 5.17, and of which values for each structure are given in Table 5.3.

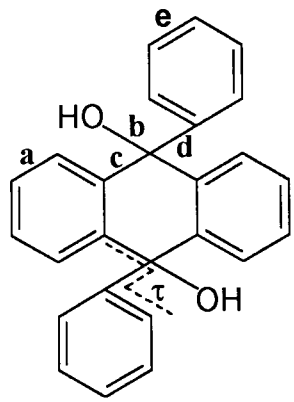

Figure 5.17 Labelling scheme of different bonds and torsion angle for the host.

Table 5.3 Bond length ranges and torsion angle observed for all four compounds.

Compounds	DACH	DA2M*	DA3M	DA4M*
a = C_{ar}≃C_{ar} (Å)	1.366(5)-1.416(5)	1.367(9)-1.407(5)	1.368(3)-1.398(3)	1.368(6)-1.407(6)
b = C_{sp}^3-O (Å)	1.450(5)	1.434(6)	1.437(2)	1.432(4)
c = C_{ar}-C_{sp}^3 (Å)	1.515(5)-1.516(5)	1.525(5)-1.527(7)	1.518(3)-1.521(3)	1.521(6)
d = C_{sp}^3-C_{ar} (Å)	1.528(5)	1.539(5)	1.530(3)	1.545(6)
e = C_{ar}≃C_{ar} (Å)	1.352(8)-1.395(6)	1.361(9)-1.401(6)	1.359(3)-1.386(3)	1.339(9)-1.398(7)
τ (°)	-54.7(4)	-68**	-54.4(2)	-61**

* taken from reference [2].
** calculated from published data, no esd given.

All bond lengths in the structures are comparable with each other, as well as with those reported for structures containing the same host DDDA[10-18]. The torsion angles measured were in the range -55--68°. The corresponding torsion angle in the structure of the host α-phase was measured on the CSDS as -62°. Hence the presence of the guests does not have significant effect on the host conformation.

5.3.2. Host packing

When the host packing is viewed perpendicular to the plane of the central tricyclic ring of the host for all four crystal structures, namely **DACH**, **DA2M**, **DA3M** and **DA4M**, two different packing patterns of host **DDDA** are observed.

The molecular packings of the host in the four structures are shown in **Figure 5.18**. The two packing patterns of the host are summarised schematically in **Figure 5.19**.

The first type of host packing is the stacked packing observed in **DACH**, **DA2M** and **DA3M**. The second is the herringbone packing seen in **DA4M**. From the same view, the packing of the host α-phase[11] is shown in **Figure 5.20**. A similar stacked packing motif is observed, although the DDDA molecules are more densely packed. The packing factors for the host alone are 27.4, 29.6, 28.8, 29.1 and 16.3Å^3/non hydrogen atom in the structures of **DACH**, **DA2M**, **DA3M**, **DA4M** and DDDA respectively.

A search of the CSDS revealed that sixteen structures involving this host compound have been elucidated. This includes the α-phase of host DDDA alone and fifteen inclusion compounds, of which nine crystallised in the space group P $\bar{1}$ with Z = 1 and show similar stacked packing.

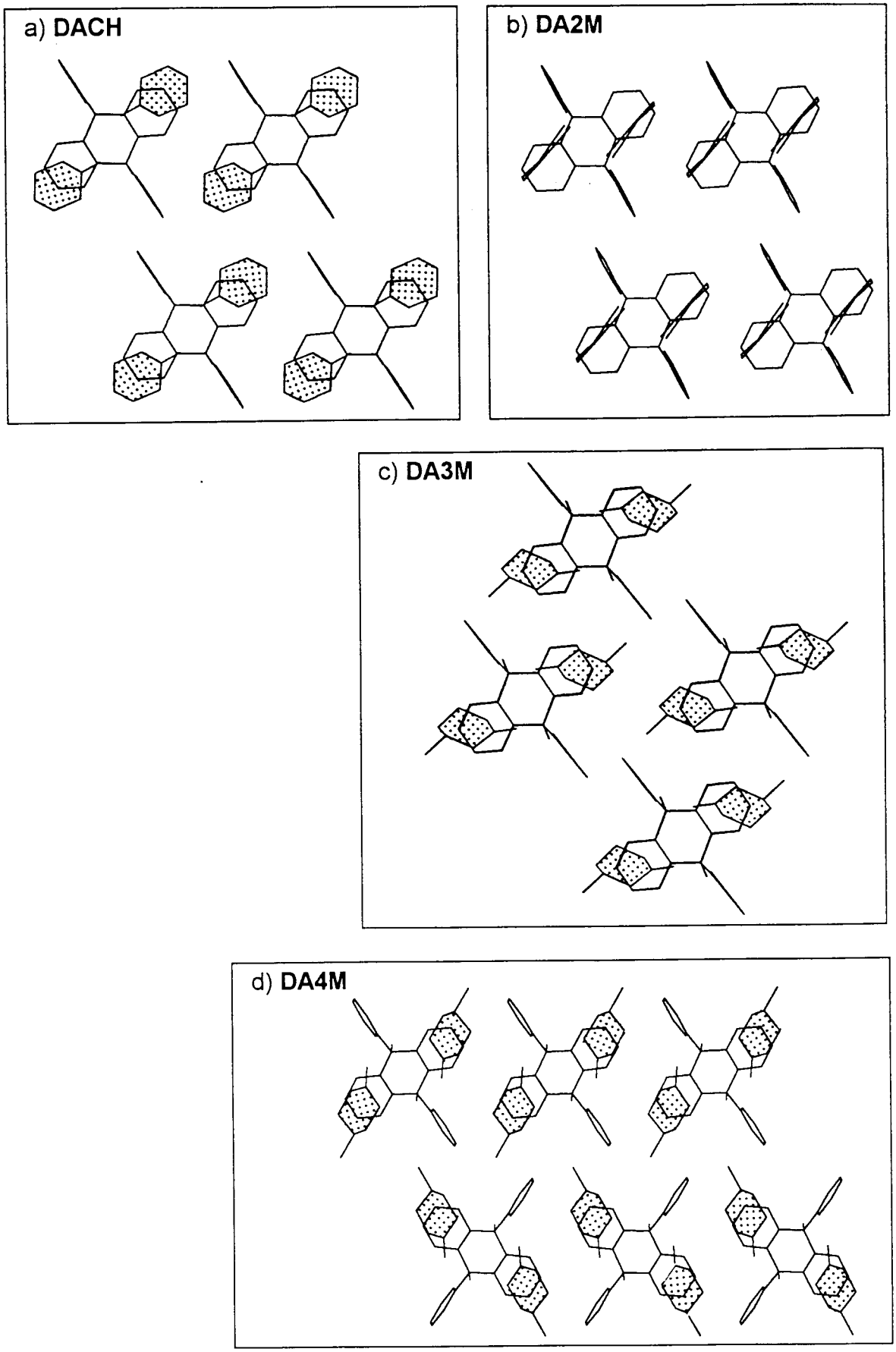

Figure 5.18 Packing diagrams of crystal structure of a) **DACH**, b) **DA2M**, c) **DA3M** and d) **DA4M**, viewed perpendicular to the central tricyclic plane. The guest molecules are shaded.

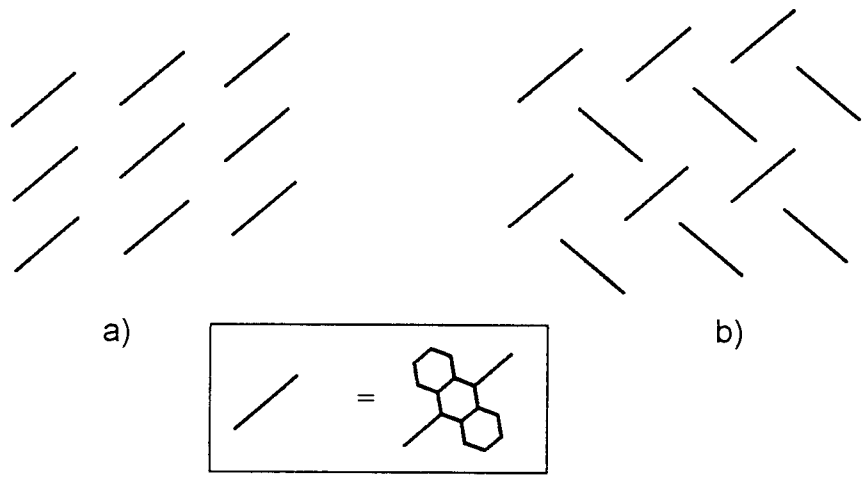

Figure 5.19 A schematic representation of the host packing patterns observed in all four compounds, when the host molecules are viewed perpendicular to the central tricyclic plane. a) stacked hosts, b) herringbone pattern.

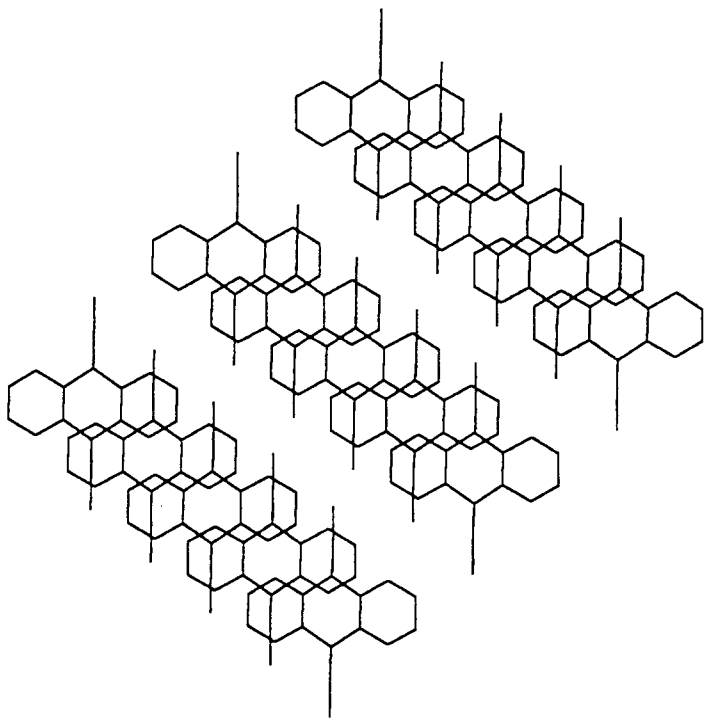

Figure 5.20 A packing diagram of the host α-phase, viewed perpendicular to the central trcyclic plane.

5.4. Discussion

The crystal structures of the two inclusion compounds **DACH** and **DA3M** were elucidated, and compared with the other two inclusion compounds **DA2M** and **DA4M**. The main interactions in all of them were similar, namely each host molecule hydrogen bonded to two guest molecules. The strength of hydrogen bonds observed are average[19] (the distances of O···O are all larger than 2.80Å, except one of the disordered models of **DACH**, which is 2.70Å). The stability of these inclusion compounds cannot be attributed solely to the host-guest interactions, but also to the topology of host-guest assembly. Structure analysis showed that the host packing in **DACH**, **DA3M** and **DA4M** formed channels running parallel to one of the crystallographic axes, in which the guest molecules are positioned in alternating head-tail arrangements. While the host in **DA2M** formed cross-linked channels running along two axes. The packing factors of all the four structures are within the range of 18.3 - 18.8 $Å^3$ / non hydrogen atom, with **DA2M** being 18.8 $Å^3$/non hydrogen atom and **DACH** **DA2M** and **DA3M** being very similar, between 18.3 and 18.5$Å^3$/non hydrogen atom.

The crystal structures of **DACH**, **DA2M** and **DA3M** are isostructural. They exhibit the same host packing motif, with two guests hydrogen bonded to one host molecule. The main differences observed in the packing can be attributed to the relative positions of the guest molecules. The unit cell parameters of the three structures are also similar, with the volume of **DA2M** being larger than **DACH** and **DA3M**, as also shown in the packing factors. This give rise to the presence of two sets of channels in **DA2M**, versus one in **DACH** and **DA3M**.

Table 5.2. Crystal data, experimental and refinement parameters.

	DACH	DA3M
Guest	Cyclohexanone	3-methylcyclohexanone
Molecular formula	$C_{26}H_{20}O_2 \cdot 2C_6H_{10}O$	$C_{26}H_{20}O_2 \cdot 2C_7H_{12}O$
Molecular weight (g mol^{-1})	560.70	588.75
Space group	P $\bar{1}$	P $\bar{1}$
a (Å)	8.741(3)	9.171(6)
b (Å)	9.008(3)	9.692(3)
c (Å)	10.863(7)	10.359(2)
α (°)	112.30(6)	93.82(2)
β (°)	93.290(6)	104.93(4)
γ (°)	101.14(3)	112.54(4)
Z	1	1
Volume ($Å^3$)	768.5(4)	807.5(6)
Density (calc.) (g cm^{-3})	1.212	1.211
F(000)	300	316
$\mu(MoK_\alpha)$ (cm^{-1})	0.77	0.76
Data collection		
Crystal dimensions (mm)	0.2 x 0.3 x 0.3	0.3 x 0.3 x 0.3
Range scanned θ(°)	2.05 - 24.97	2.07 - 24.97
Range of indices h, k, l	-10,10; -10,9; 0,12	-10,10; -11,11; 0,12
No. of reflections collected	2855	3021
No. of reflections observed with $I_{rel} > 2\sigma(I_{rel})$	1469	1802
Final refinement		
No. of restraints	3	2
No. of parameters	206	209
R1 ($I_{rel} > 2\sigma(I_{rel})$)	0.0797	0.0446
wR2 ($I_{rel} > 2\sigma(I_{rel})$)	0.2374	0.1089
Extinction coefficient	0.09(2)	-
Max. height in electron density map ($eÅ^{-3}$)	0.459	0.185
Min. height in electron density map ($eÅ^{-3}$)	-0.191	-0.172
S	1.053	1.045

References

1. Cambridge Structural Database System, Version 5.14, Oct. 1997, Cambridge Crystallographic Data Centre, Cambridge.
2. D. R. Bond, L. R. Nassimbeni and F. Toda, *J. Crystallogr. Spectrosc. Res.*,19, 1989. p847.
3. G. M. Sheldrick, 'SHELX-86: Crystallographic computing 3', G. M. Sheldrick, C. Kruger and R. Goddard (eds.), Oxford University Press, 1985.
4. G. M. Sheldrick, SHELXL-93: Programme for Crystal Structure Determination, unpublished work
5. I. Olovsson and P. Jönsson, 'The Hydrogen Bond - Structure and Spectroscopy', P. Schuster, G. Zundel and C. Sarderfy (eds.) North-Holland Publishing Company, U.S.A., 1975.
6. F. H. Allen, O. Kennard, D. G. Watson, L. Brammer, A. G. Orpen and R. Taylor, *J. Chem. Soc., Perkin Trans.* 2, 1987, S1-S19.
7. L. J. Barbour, PhD Thesis, University of Cape Town, 1994.
8. W. L. Duax and D. A. Norton (Eds.), 'Altas of Steroid Structure', Vol 1, Plenum Press, London, 1975.
9. W. -D. Schubert, M.Sc. Thesis, University of Cape Town, 1991.
10. F. Toda, K. Tanaka and T. C. W. Mak *J. Inclu. Phenom.* 3, 1985, p225.
11. F. Toda, K. Tanaka, S. Nagamatsu and T. C. W. Mak *Isr. J. Chem.* 25, 1985, p346.
13. L. J. Barbour, M. R. Caira and L. R. Nassimbeni, *J. Chem. Soc. Perkin Trans* 2, 1993, P2321.
15. L. J. Barbour, M. R. Caira and L. R. Nassimbeni, *J. Chem. Cryst.* 24, 1994, P539
16. D. R. Bond, M. R. Caira, G. A. Harvey, L. R. Nassimbeni and F. Toda, *Acta. Crystallogr.* B46, 1990, p771.
17. D. R. Bond, L. R. Nassimbeni and F. Toda, *J. Inclu. Phenom.*, 7, 1989. p623.

18. F. Toda, K. Tanaka and T. C. W. Mak *Tetrahedron Lett.*, 25,1984, p1359.

19. P. Gilli, V. Bertolasi, V. Ferretti and G. Gilli, *J. Am. Chem. Soc.* 116, 1994, p909.

CHAPTER 6

COMPETITION EXPERIMENTS

6. COMPETITION EXPERIMENTS

6.1. Introduction

Separation of close isomers by enclathration is one of the important uses of inclusion chemistry and has considerable future industrial prospect. This process generally follows the same simple methodology. A suitable host compound is recrystallized from the mixture of close isomers. The resulting clathrate crystals are filtered and heated gently to release the guest. A high purity of the required isomer can then be achieved after several cycles of recrystallization. The host compound may be recovered and recycled during the process. This process may also be carried out in suspension for solid-solid reactions[1,2].

The principle of separation by enclathration is based on molecular recognition, a subject which has been extensively reviewed[3,4]. It is generally accepted that the molecular recognition during crystallisation depends on the complementarity of molecular features[5]. The process of crystallisation is also subject to both kinetic and thermodynamic factors. Therefore the recognition or selectivity of a host for different guests may be evaluated through the studies of physical properties, kinetics, thermal stabilities and molecular structures. The competition experiments thus were conducted, in an attempt to find reasonable trends in terms of measured physico-chemical quantities.

6.2. Competition experiments

Competition experiments were performed by dissolving the host in mixtures of two-component or three-component guests, and allowing crystals of the inclusion compounds to be formed by the slow cooling method. The relative amounts of the guests initially prepared in the mixture and finally included in the crystals were analysed using Gas Chromatography. Cyclohexanone (**G1**)

was separated from the three methylcyclohexanone isomers (**G2**, **G3** and **G4**) using a 10% OV101 on Chromosorp Packing Column (1m). But it was not possible to separate the three isomers from one another on this column. Using a Supelcowax Fused Silica Capillary Column (30m, 0.20mm LD, 0.20μm film thickness), separation of **G4** from **G2** and **G3** was accomplished. In spite of various attempts to change the rate of the carrier gas, oven temperature programme *etc.*, **G2** and **G3** could not be separated.

Competition experiments were conducted between two-component guest mixtures: **G1** and 2-methylcyclohexanone (**G2**), **G1** and 3-methylcyclohexanone (**G3**), **G1** and 4-methylcyclohexanone (**G4**), **G4** and **G2**, **G4** and **G3**. The results are presented graphically in **Figure 6.1** and **6.2**.

Figure 6.1 shows the competition results between **G1** and either of **G2**, **G3** and **G4**. In the case of the competition experiment between **G1** and **G2**, **G1** was favoured. At molefractions of less than 20% of **G1**, selective inclusion of **G2** was observed. This phenomenon of concentration dependence on guest selectivity has been observed in competition experiments carried out between a cyclophane host and pizoline isomers[6]. As soon as the molefraction of **G1** increased to above 30%, more than 70% of **G1** was selectively included in the crystals.

Similar results were observed for the competition between **G1** and **G3**. In this case, though, no separation was observed when molefraction of **G1** less than 10%. Above this level, **G1** was favoured. The selectivity for **G1** over **G3** was not as good as that for **G1** over **G2**.

The competition results between **G1** and **G4** show a concentration-dependent selectivity. At molefraction of less than 45% of **G1**, **G4** was selectively included. Above 45% of **G1**, **G1** was favoured. Therefore, no selectivity of **G1** above **G4** can be convincingly predicted.

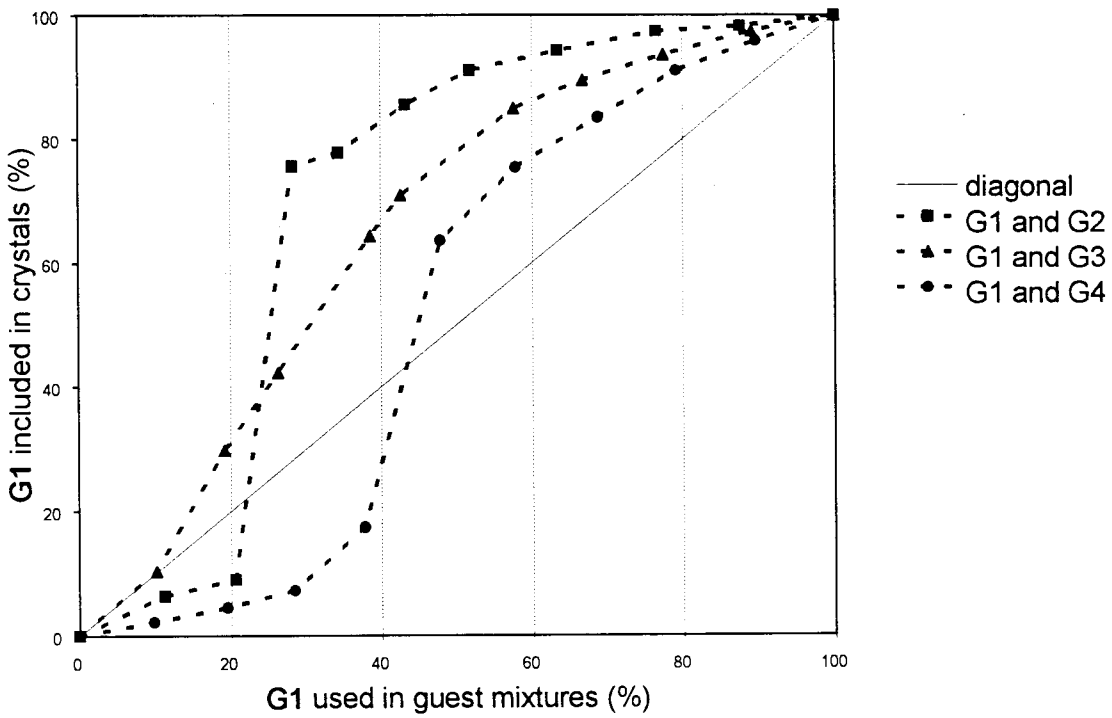

Figure 6.1 Results of the competition experiments carried out between two-component guests **G1** and **G2**, **G1** and **G3**, **G1** and **G4**, respectively.

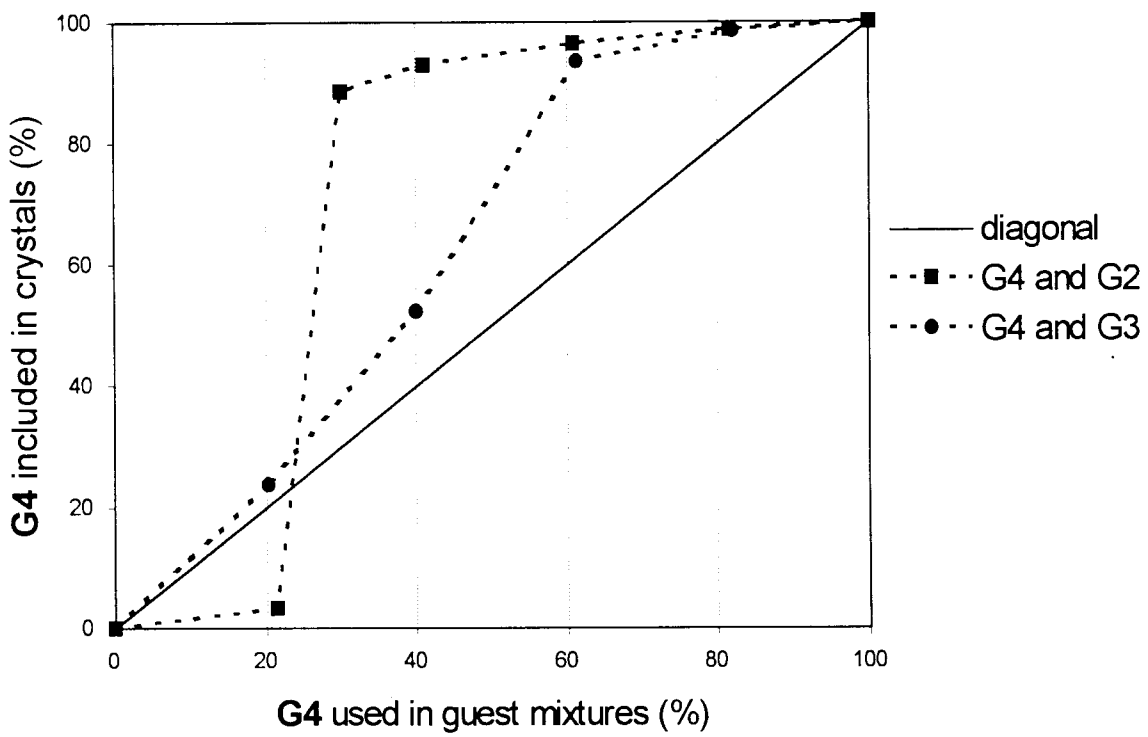

Figure 6.2 Results of the competition experiments carried out between 2-component guests **G4** and **G2**, **G4** and **G3** respectively.

In Figure 6.2 the competition experiments between **G4** and **G2**, **G4** and **G3** are depicted. It is clear that **G4** is strongly favoured above **G2**. Above 20% molefraction of **G4**, more than 80% of it is included. While **G4** shows less selectivity over **G3**, with only 50% inclusion at an original molefraction of 40%, rising to 80% inclusion from about 60% starting molefraction.

Summarising all those two-component competition results, we would expect to observed the following trend: **G1** $\cong$ **G4** > **G3** and **G1** $\cong$ **G4** >> **G2**.

In order to test this prediction, a set of three-component guest mixtures was prepared, consisting of equal molefractions of **G1**, **G2** and **G4**, similarly **G1**, **G3** and **G4**. The results are summarised in **Figure 6.3** and **6.4** respectively.

Composition of guests used ⟶ Composition of guests inluded

Figure 6.3 The competition result between **G1**, **G2** and **G4**.

From Figure 6.3, **G1** is favoured above **G2**, with hardly any change in the molefraction of **G4** between the starting guest mixtures and the crystals. Only 7.7% of **G2** was finally included, whereas 57.4% of **G1** was included.

Composition of guests used ⟶ Composition of guests included

Figure 6.4 The competition result between **G1**, **G3** and **G4**.

Selectivity of **G1** over **G3** was also observed in the other three-component competition. As predicted this selectivity was not as good as **G1** over **G2** in the case of three-component competition between **G1**, **G2** and **G4**. And again, no selectivity for **G4** was observed. Only 21.7% of **G3** was included, whereas 45.8% of **G1** was included.

References

1. M. R. Caira, A. Horne, L. R. Nassimbeni and F. Toda, *J. Mater. Chem.*, 1997, p2145; *J. Chem. Soc. Perkin Trans.* 2, 1997, p1717.
2. M. R. Caira, A. Horne, L. R. Nassimbeni, K. Okuda and F. Toda, *J. Chem. Soc. Perkin Trans.* 2, 1995, p1063.
3. 'Inclusion compounds', J. L. Atwood, J. E. D. Davies and D. D. MacNicol (eds.), vol.1-3, Academic Press, London, 1984; vol.4-5, Oxford University Press, Oxford, 1991.
4. 'Comprehensive Supramolecular Chemistry', J. -M. Lehn, J. L. Atwood, J. E. D. Davies, D. D. MacNicol and F. Vögtle (eds.), vol.1-3, Pregamon Press, Oxford, 1996.
5. G. R. Desiraju, *Chem. Commun.*, 1997, p1475.
6. S. Apel and L. R. Nassimbeni, unpublished results.

CHAPTER 7

CONCLUSION

7. CONCLUSION

The decomposition reactions, thermal stabilities and crystal structures of the inclusion compounds between the host, *trans*-9,10-dihydroxy-9,10-diphenyl-9,10-dihydroanthracene, and four related guests, cyclohexanone and the three methyl-substituted cyclohexanones, have been studied. Some of the results obtained in this study are summarised in **Table 7.1**.

Table 7.1 Some of the results in this study for all the four inclusion compounds.

Compounds	**DACH**	**DA2M**	**DA3M**	**DA4M**
Packing factors ($Å^3$/non-hydrogen atoms)	18.30	18.82	18.35	18.49
H-bond / d(O···O) (Å)	2.749(3) *	2.894(4)	2.862(3)	2.806(5)
E_a (kJ/mol)	86(3)	85(4)	101(3)	79(5)
T_{on} - T_b (°C)	-27.1	-81.1	-88.2	-61.1
ΔH (kJ/mol) (normalised)	35.5	39.1	53.5	51.5

* is the average value due to guest disorder (see Chapter 5)

All four inclusion compounds have host:guest ratios of 1:2, which were confirmed using TG. The inclusion compounds can be formed either by exposure of the host powder to the guest vapours or crystallisation of the inclusion compounds in the guest solvents. Using XRD, it was found that the decomposition of the inclusion compounds are accompanied by a phase change. The β-phases of the inclusion compounds collapse to the non-porous α-phase of the host alone upon desolvation.

The crystal structures of two of the four inclusion compounds, **DACH** and **DA3M**, were elucidated and compared with those of **DA2M** and **DA4M** reported in the literature. In all four inclusion compounds, each host molecule is hydrogen bonded to two guest molecules via the hydroxyl groups on the host

to the carbonyl oxygen on the guest. In each case, the host molecules were all located on a centre of symmetry. Three of the four structures, **DACH**, **DA2M** and **DA3M**, are isostructural. They crystallised in the space group, P $\bar{1}$, and exhibited the same host packing motif, with two guest molecules hydrogen bonded to one host molecule at only slightly different orientations and positions. **DA4M** crystallised in a herringbone fashion, which is significantly different from the stacked packing observed in the other three inclusion compounds. From the single crystal structures, it was evident that the guests are located in channels formed by the host molecules along crystallographic axes in all four inclusion compounds. The packing factors, which is the volume per non-hydrogen atoms, are similar for **DACH**, **DA3M** and **DA4M**, and imply that **DA2M** is less dense packed. The O···O distance of the hydrogen bond is often related to the strength of the hydrogen bond. The trend in order of increasing hydrogen bonding distance is as follows:

DACH < **DA4M** < **DA3M** < **DA2M**

All four inclusion compounds decay in a single step. The single crystals of the four inclusion compounds underwent similar thermal changes on the Hotstage. The guest release was followed by the sublimation and recrystallisation of the desolvated host, which finally melts at approximately 269°C. The onset temperatures for the guest release as well as the enthalpy changes were obtained from DSC. From the values of T_{on} - T_b in Table 7.1, as a crude measure of thermal stabilities of the inclusion compounds, **DACH** appears to be more stable than **DA2M**, **DA3M** and **DA4M**.

Competition experiments show the preferential formation of the inclusion compound **DACH** over **DA3M** and **DA2M**. **DA4M** was also preferred over **DA3M** and **DA2M**. A slight preference for **DACH** over **DA4M** was observed, at mole fraction of cyclohexanone above 45%.

The kinetics of decomposition of the four inclusion compounds yielded the

activation energies, which ranged between 79 - 101 kJ/mol. Previous kinetic studies on organic inclusion compounds of related hosts showed that the activation energy of decomposition is related to the topology of the host and guest assemblies. The inclusion compounds, in which the guest molecules are located along channels, are known to have activation energies between 58 - 151 kJ/mol[1-3]. This is lower than that for inclusion compounds, in which the guest molecule or molecules are located in cavities surrounded by host molecules in all dimensions, in which the activation energies lie between 116 - 284 kJ/mol[4,5]. In this study, the guest molecules in all four inclusion compounds are located in channels with no physical barriers to the diffusion of the guest molecules out of the host lattice. The activation energies of decomposition obtained here fall in the range observed for channel type inclusion compounds.

The kinetics of decomposition of **DACH** exhibited compensation behaviour. The Arrhenius parameters obtained for the decomposition of **DACH**, carried out using different apparatus and samples with different pre-treatment and particle sizes show an interdependent relationship. This is a very significant result, yielding the isokinetic temperature, at which the rates of the decomposition reactions are equal, irrespective of the experimental conditions. Compensation behaviour was also observed for the kinetics of decomposition of the four different inclusion compounds, using the same apparatus and experimental conditions. In this case, a linear relationship exists between the Arrhenius parameters, according to the following equation:

$$\ln A = bE_a + c$$

where the parameter b characterises the strength of the bond to be broken, while c is proposed to be related to the structure of, and defects in, the starting materials. In all four structures, the guests are hydrogen bonded to the host via the hydroxyl moiety of the host. The existence of the compensation effect confirms that these four decomposition reactions are similar with respect to the types of bonds that are to be broken. The same reaction mechanism, that of the contracting area geometrical model (R2), was observed for all four

decomposition reactions. R2 describes a phase-boundary controlled reaction, of which rate is determined by two-dimensional growth of the product interface at a constant velocity on cylindrical particles.

References

1. J. L. Scott, PhD Thesis, University of Cape Town, 1995.
2. A. Coetzee, PhD Thesis, University of Cape Town, 1996.
3. M. R. Caira, A. Coetzee, L. R. Nassimbeni, E. Weber and A. Wierig, *J. Chem. Soc. Perkin Trans.*2, 1997, p237 and p281.
4. J. L. Scott, *J. Chem. Soc. Perkin Trans.* 2, 1995, p495.
5. S. A. Bourne, B. M. Oom and F. Toda, *J. Chem. Soc., Perkin Trans.*2, 1997, p585.

APPENDICES

Appendix A

X-ray powder diffraction patterns of:

A 1) Experimental **DA4M** prepared from the levitating balance (LB) by exposing the host to the guest vapour and
   2) calculated form the crystal stucture data of **DA4M**.
B 1) Experimental **DA3M** obtained from the LB and
   2) calculated from the crystal stucture data of **DA3M**.
C 1) Experimental **DA2M** obtained from the LB and
   2) calculated form the crystal stucture data of **DA2M**.

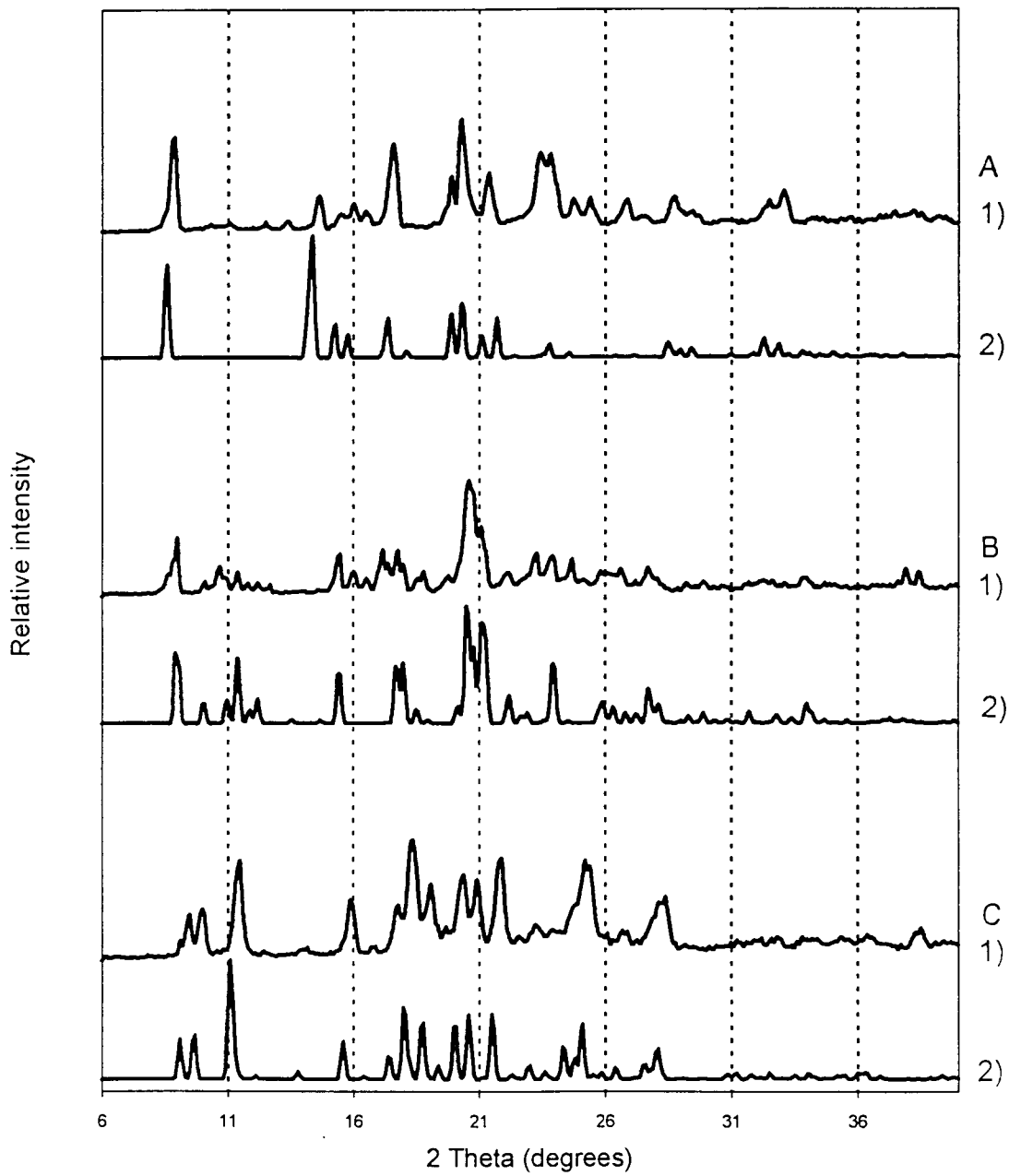

Appendix A (Cont.)

X-ray powder diffraction patterns of:

1. The desolvated product of the inclusion compound **DA2M**.
2. The desolvated product of the inclusion compound **DA3M**.
3. The desolvated product of the inclusion compound **DA4M**.
4. Calculated for the non-porous α-phase of the host DDDA.

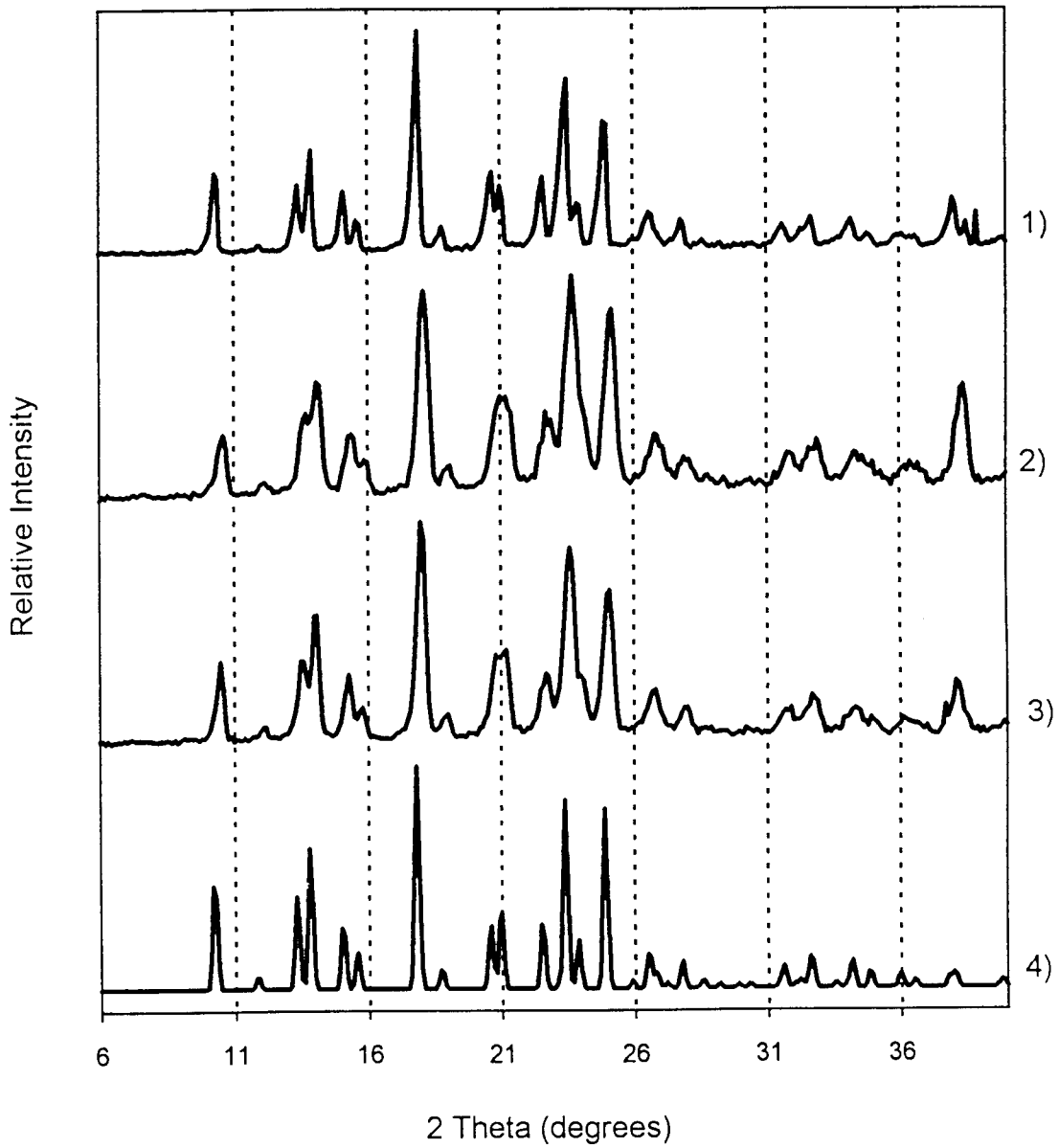

Appendix B

Supplementary data for the crystal structure of **DACH**

Table 1a Atomic co-ordinates and equivalent isotropic displacement parameters (Å^2) for **DACH**. U_{eq} is defined as one third of the trace of the orthogonalized U_{ij} tensor.

Atoms	x	y	z	U_{eq}
C(2)	0.5473(4)	0.6685(4)	0.5134(4)	0.055(1)
C(1)	0.5193(4)	0.5326(4)	0.3735(4)	0.058(1)
C(8)	0.3991(5)	0.5617(4)	0.2824(3)	0.059(1)
C(7)	0.5337(4)	0.6387(4)	0.6281(4)	0.057(1)
C(6)	0.5658(5)	0.7736(4)	0.7547(4)	0.072(1)
C(4)	0.6235(5)	0.9618(4)	0.6488(5)	0.079(1)
C(5)	0.6097(5)	0.9319(4)	0.7639(4)	0.083(1)
C(3)	0.5924(5)	0.8315(4)	0.5252(4)	0.069(1)
O(1)	0.6669(4)	0.5451(4)	0.3195(4)	0.095(1)
C(9)	0.2480(5)	0.5594(4)	0.3132(4)	0.067(1)
C(13)	0.4369(6)	0.5916(5)	0.1709(4)	0.081(1)
C(10)	0.1362(6)	0.5855(5)	0.2315(5)	0.088(2)
C(11)	0.1768(8)	0.6138(5)	0.1214(5)	0.098(2)
C(12)	0.3248(9)	0.6162(5)	0.0910(4)	0.100(2)
C(1G)	0.9015(7)	0.2457(7)	0.3206(6)	0.110(2)
C(2G)	0.848(1)	0.1737(9)	0.1803(7)	0.147(3)
C(5G)	0.920(1)	-0.031(1)	0.317(1)	0.155(3)
C(6G)	0.980(2)	0.162(1)	0.3765(8)	0.233(6)
C(4G)	0.881(1)	-0.1014(9)	0.170(1)	0.162(3)
C(3G)	0.802(2)	-0.013(1)	0.1188(9)	0.243(7)
O(1GA)	0.8705(7)	0.3813(8)	0.3757(6)	0.102(2)
O(1GB)	0.773(1)	0.265(1)	0.1623(9)	0.111(3)

Table 2a Bond lengths [Å] and angles [°] for **DACH**.

C(2)-C(7)	1.377(5)	C(2)-C(3)	1.399(5)
C(2)-C(1)	1.515(5)	C(1)-O(1)	1.450(5)
C(1)-C(7)#1	1.516(5)	C(1)-C(8)	1.528(5)
C(8)-C(9)	1.379(5)	C(8)-C(13)	1.382(5)
C(7)-C(6)	1.416(5)	C(7)-C(1)#1	1.516(5)
C(6)-C(5)	1.366(5)	C(4)-C(3)	1.376(6)
C(4)-C(5)	1.383(6)	C(9)-C(10)	1.395(6)
C(13)-C(12)	1.376(7)	C(10)-C(11)	1.366(8)
C(11)-C(12)	1.352(8)	C(1G)-O(1GA)	1.231(7)
C(1G)-C(6G)	1.384(9)	C(1G)-C(2G)	1.418(9)
C(2G)-O(1GB)	1.208(9)	C(2G)-C(3G)	1.51(1)
C(5G)-C(4G)	1.46(1)	C(5G)-C(6G)	1.57(1)
C(4G)-C(3G)	1.40(1)		
C(7)-C(2)-C(3)	119.1(3)	C(7)-C(2)-C(1)	123.3(3)
C(3)-C(2)-C(1)	117.6(3)	O(1)-C(1)-C(2)	107.1(3)
O(1)-C(1)-C(7)#1	109.2(3)	C(2)-C(1)-C(7)#1	113.3(3)
O(1)-C(1)-C(8)	107.0(3)	C(2)-C(1)-C(8)	109.9(3)
C(7)#1-C(1)-C(8)	110.0(3)	C(9)-C(8)-C(13)	118.8(4)
C(9)-C(8)-C(1)	118.9(3)	C(13)-C(8)-C(1)	122.3(4)
C(2)-C(7)-C(6)	119.2(3)	C(2)-C(7)-C(1)#1	123.4(3)
C(6)-C(7)-C(1)#1	117.4(4)	C(5)-C(6)-C(7)	120.8(4)
C(3)-C(4)-C(5)	119.7(4)	C(6)-C(5)-C(4)	120.0(4)
C(4)-C(3)-C(2)	121.3(4)	C(8)-C(9)-C(10)	120.0(4)
C(12)-C(13)-C(8)	120.4(5)	C(11)-C(10)-C(9)	119.9(5)
C(12)-C(11)-C(10)	120.3(5)	C(11)-C(12)-C(13)	120.6(5)
O(1GA)-C(1G)-C(6G)	128.9(6)	O(1GA)-C(1G)-C(2G)	112.1(6)
C(6G)-C(1G)-C(2G)	119.0(6)	O(1GB)-C(2G)-C(1G)	104.5(7)
O(1GB)-C(2G)-C(3G)	126.2(9)	C(1G)-C(2G)-C(3G)	115.0(6)
C(4G)-C(5G)-C(6G)	112.5(6)	C(1G)-C(6G)-C(5G)	116.3(7)
C(3G)-C(4G)-C(5G)	114.8(7)	C(4G)-C(3G)-C(2G)	119.7(7)

Symmetry transformations used to generate equivalent atoms:
#1 -x+1,-y+1,-z+1

Table 3a Anisotropic displacement parameters ($Å^2$) for **DACH**. The anisotropic displacement factor exponent takes the form:
$-2\pi^2[h^2a^{*2}U_{11} + ... + 2h\ ka^*b^*U_{12}]$

Atoms	U_{11}	U_{22}	U_{33}	U_{23}	U_{13}	U_{12}
C(2)	0.050(2)	0.039(2)	0.070(2)	0.019(2)	-0.009(2)	0.008(1)
C(1)	0.053(2)	0.044(2)	0.076(2)	0.024(2)	0.007(2)	0.011(2)
C(8)	0.077(3)	0.037(2)	0.057(2)	0.015(2)	0.002(2)	0.012(2)
C(7)	0.056(2)	0.040(2)	0.069(2)	0.018(2)	-0.007(2)	0.012(1)
C(6)	0.088(3)	0.051(2)	0.068(3)	0.016(2)	-0.013(2)	0.016(2)
C(4)	0.089(3)	0.038(2)	0.095(3)	0.021(2)	-0.026(2)	0.005(2)
C(5)	0.104(3)	0.040(2)	0.083(3)	0.008(2)	-0.027(2)	0.014(2)
C(3)	0.072(2)	0.045(2)	0.084(3)	0.027(2)	-0.013(2)	0.004(2)
O(1)	0.075(2)	0.063(2)	0.150(3)	0.039(2)	0.043(2)	0.021(1)
C(9)	0.065(2)	0.062(2)	0.072(2)	0.028(2)	-0.005(2)	0.011(2)
C(13)	0.127(4)	0.058(2)	0.066(3)	0.027(2)	0.027(2)	0.033(2)
C(10)	0.077(3)	0.064(3)	0.111(4)	0.031(2)	-0.024(3)	0.008(2)
C(11)	0.146(5)	0.054(2)	0.076(3)	0.018(2)	-0.043(3)	0.016(3)
C(12)	0.186(6)	0.068(3)	0.052(3)	0.023(2)	0.009(3)	0.044(3)
C(1G)	0.113(4)	0.091(4)	0.114(5)	0.026(3)	0.012(3)	0.030(3)
C(2G)	0.226(8)	0.112(5)	0.108(5)	0.043(4)	-0.017(5)	0.066(5)
C(5G)	0.202(8)	0.163(7)	0.170(8)	0.116(7)	0.053(6)	0.086(6)
C(6G)	0.39(2)	0.183(8)	0.124(6)	0.019(5)	-0.073(8)	0.18(1)
C(4G)	0.217(9)	0.098(5)	0.170(8)	0.042(5)	0.029(7)	0.053(5)
C(3G)	0.34(2)	0.173(8)	0.144(7)	-0.029(6)	-0.111(8)	0.142(9)
O(1GA)	0.091(4)	0.098(4)	0.116(4)	0.034(3)	0.022(3)	0.035(3)
O(1GB)	0.149(8)	0.123(7)	0.111(7)	0.077(6)	0.037(5)	0.077(6)

Table 4a Hydrogen co-ordinates and isotropic displacement parameters ($Å^2$) for **DACH**.

Atoms	**x**	**y**	**z**	U_{eq}
H(6)	0.5569(5)	0.7543(4)	0.8325(4)	0.091(5)
H(4)	0.6537(5)	1.0695(4)	0.6549(5)	0.091(5)
H(5)	0.6302(5)	1.0196(4)	0.8477(4)	0.091(5)
H(3)	0.6015(5)	0.8522(4)	0.4480(4)	0.091(5)
H(1)	0.733(8)	0.458(7)	0.3015(4)	0.21(3)
H(9)	0.2207(5)	0.5404(4)	0.3883(4)	0.091(5)
H(13)	0.5387(6)	0.5950(5)	0.1496(4)	0.091(5)
H(10)	0.0342(6)	0.5837(5)	0.2520(5)	0.091(5)
H(11)	0.1023(8)	0.6315(5)	0.0672(5)	0.091(5)
H(12)	0.3512(9)	0.6347(5)	0.0155(4)	0.091(5)

Table 5a Selected torsion angles(°)for **DACH**.

C7-C2-C1-O1	-117.3(4)	C3-C2-C1-O1	61.3(4)
C7-C2-C1-C7#1	3.2(5)	C3-C2-C1-C7#1	-178.3(3)
C7-C2-C1-C8	126.7(4)	C3-C2-C1-C8	-54.7(4)
O1-C1-C8-C9	-178.9(3)	C2-C1-C8-C9	-62.9(4)
C7#1-C1-C8-C9	62.6(4)	O1-C1-C8-C13	0.6(4)
C2-C1-C8-C13	116.6(4)	C7#1-C1-C8-C13	-118.0(4)
C3-C2-C7-C6	-0.1(5)	C1-C2-C7-C6	178.5(3)
C3-C2-C7-C1#1	178.0(3)	C1-C2-C7-C1#1	-3.5(6)
C2-C7-C6-C5	0.04(6)	C1#1-C7-C6-C5	-178.1(4)
C7-C6-C5-C4	-0.1(6)	C3-C4-C5-C6	0.2(6)
C5-C4-C3-C2	-0.2(6)	C7-C2-C3-C4	0.2(5)
C1-C2-C3-C4	-178.5(3)	C13-C8-C9-C10	0.5(5)
C1-C8-C9-C10	-180.0(3)	C9-C8-C13-C12	-0.9(6)
C1-C8-C13-C12	179.6(3)	C8-C9-C10-C11	-0.2(6)
C9-C10-C11-C12	0.2(6)	C10-C11-C12-C13	-0.5(7)
C8-C13-C12-C11	0.9(7)	O1GA-C1G-C2G-O1GB	-7(1)
C6G-C1G-C2G-O1GB	174(1)	O1GA-C1G-C2G-C3G	-149.4(8)
C6G-C1G-C2G-C3G	32(1)	O1GA-C1G-C6G-C5G	144.1(8)
C2G-C1G-C6G-C5G	-37(1)	C4G-C5G-C6G-C1G	41(1)
C6G-C5G-C4G-C3G	-42(1)	C5G-C4G-C3G-C2G	40(2)
O1GB-C2G-C3G-C4G	-166(1)	C1G-C2G-C3G-C4G	-33(2)

Symmetry transformations used to generate equivalent atoms:
#1 -x+1,-y+1,-z+1

Appendix B (Cont.)

Supplementary data for the crystal structure of **DA3M**

Table 1b Atomic co-ordinates and equivalent isotropic displacement parameters (Å^2) for **DA3M**. U_{eq} is defined as one third of the trace of the orthogonalized U_{ij} tensor.

Atoms	x	y	z	U_{eq}
O(1)	0.4104(2)	0.8406(2)	0.6836(2)	0.052(1)
C(1)	0.4510(2)	0.9789(2)	0.6301(2)	0.040(1)
C(2)	0.3270(2)	0.9504(2)	0.4911(2)	0.039(1)
C(3)	0.1606(3)	0.9049(2)	0.4835(2)	0.051(1)
C(4)	0.0401(3)	0.8746(3)	0.3623(2)	0.059(1)
C(5)	0.0837(3)	0.8876(3)	0.2443(2)	0.062(1)
C(6)	0.2460(3)	0.9317(3)	0.2495(2)	0.052(1)
C(7)	0.3709(2)	0.9646(2)	0.3728(2)	0.039(1)
C(8)	0.4344(2)	1.0936(2)	0.7278(2)	0.039(1)
C(9)	0.4480(3)	1.2330(2)	0.6954(2)	0.048(1)
C(10)	0.4270(3)	1.3359(3)	0.7797(2)	0.055(1)
C(11)	0.3945(3)	1.3011(3)	0.8986(2)	0.055(1)
C(12)	0.3840(3)	1.1653(3)	0.9327(2)	0.060(1)
C(13)	0.4027(3)	1.0605(3)	0.8482(2)	0.050(1)
O(1G)	0.3210(2)	0.5601(2)	0.5095(2)	0.080(1)
C(1G)	0.2163(3)	0.4660(3)	0.4126(2)	0.058(1)
C(2G)	0.0555(3)	0.4739(3)	0.3464(3)	0.072(1)
C(3G)	0.0010(3)	0.4391(3)	0.1937(3)	0.067(1)
C(4G)	0.0126(3)	0.2955(3)	0.1434(3)	0.074(1)
C(5G)	0.1846(4)	0.3034(3)	0.2017(3)	0.080(1)
C(6G)	0.2403(3)	0.3344(3)	0.3561(3)	0.071(1)
C(7G)	-0.1698(4)	0.4359(4)	0.1348(3)	0.095(1)

Table 2b Bond lengths (Å) and angles (°) for **DA3M**.

O(1)-C(1)	1.437(2)	C(1)-C(2)	1.518(3)
C(1)-C(7)#1	1.521(3)	C(1)-C(8)	1.530(3)
C(2)-C(7)	1.385(3)	C(2)-C(3)	1.396(3)
C(3)-C(4)	1.368(3)	C(4)-C(5)	1.380(3)
C(5)-C(6)	1.368(3)	C(6)-C(7)	1.398(3)
C(7)-C(1)#1	1.521(3)	C(8)-C(9)	1.380(3)
C(8)-C(13)	1.382(3)	C(9)-C(10)	1.384(3)
C(10)-C(11)	1.374(3)	C(11)-C(12)	1.359(3)
C(12)-C(13)	1.386(3)	O(1G)-C(1G)	1.213(3)
C(1G)-C(6G)	1.484(3)	C(1G)-C(2G)	1.491(4)
C(2G)-C(3G)	1.503(4)	C(3G)-C(4G)	1.505(4)
C(3G)-C(7G)	1.514(4)	C(4G)-C(5G)	1.507(4)
C(5G)-C(6G)	1.520(4)		
O(1)-C(1)-C(2)	109.3(2)	O(1)-C(1)-C(7)#1	108.7(2)
C(2)-C(1)-C(7)#1	113.1(2)	O(1)-C(1)-C(8)	106.5(2)
C(2)-C(1)-C(8)	109.1(2)	C(7)#1-C(1)-C(8)	110.0(2)
C(7)-C(2)-C(3)	119.0(2)	C(7)-C(2)-C(1)	123.3(2)
C(3)-C(2)-C(1)	117.7(2)	C(4)-C(3)-C(2)	121.7(2)
C(3)-C(4)-C(5)	119.3(2)	C(6)-C(5)-C(4)	119.9(2)
C(5)-C(6)-C(7)	121.5(2)	C(2)-C(7)-C(6)	118.6(2)
C(2)-C(7)-C(1)#1	123.5(2)	C(6)-C(7)-C(1)#1	117.8(2)
C(9)-C(8)-C(13)	118.4(2)	C(9)-C(8)-C(1)	120.0(2)
C(13)-C(8)-C(1)	121.6(2)	C(8)-C(9)-C(10)	120.9(2)
C(11)-C(10)-C(9)	120.0(2)	C(12)-C(11)-C(10)	119.5(2)
C(11)-C(12)-C(13)	121.0(2)	C(8)-C(13)-C(12)	120.2(2)
O(1G)-C(1G)-C(6G)	121.4(2)	O(1G)-C(1G)-C(2G)	122.1(2)
C(6G)-C(1G)-C(2G)	116.5(2)	C(1G)-C(2G)-C(3G)	114.4(2)
C(2G)-C(3G)-C(4G)	110.8(2)	C(2G)-C(3G)-C(7G)	111.0(2)
C(4G)-C(3G)-C(7G)	113.0(2)	C(3G)-C(4G)-C(5G)	111.7(2)
C(4G)-C(5G)-C(6G)	111.7(2)	C(1G)-C(6G)-C(5G)	112.1(2)

Symmetry transformations used to generate equivalent atoms:
#1 -x+1,-y+2,-z+1

Table 3b Anisotropic displacement parameters ($Å^2$) for **DA3M**. The anisotropic displacement factor exponent takes the form:
$2\pi^2[h^2a^{*2}U_{11} + ... + 2hka^*b^*U_{12}]$.

Atoms	U_{11}	U_{22}	U_{33}	U_{23}	U_{13}	U_{12}
O(1)	0.068(1)	0.042(1)	0.047(1)	0.008(1)	0.022(1)	0.020(1)
C(1)	0.041(1)	0.042(1)	0.035(1)	0.005(1)	0.013(1)	0.015(1)
C(2)	0.035(1)	0.038(1)	0.041(1)	-0.002(1)	0.011(1)	0.013(1)
C(3)	0.040(1)	0.057(1)	0.050(1)	-0.005(1)	0.016(1)	0.015(1)
C(4)	0.032(1)	0.068(2)	0.064(2)	-0.014(1)	0.006(1)	0.017(1)
C(5)	0.046(1)	0.075(2)	0.053(1)	-0.011(1)	-0.003(1)	0.029(1)
C(6)	0.047(1)	0.066(2)	0.039(1)	0.000(1)	0.007(1)	0.026(1)
C(7)	0.037(1)	0.042(1)	0.036(1)	-0.001(1)	0.007(1)	0.017(1)
C(8)	0.033(1)	0.042(1)	0.036(1)	0.001(1)	0.009(1)	0.012(1)
C(9)	0.049(1)	0.047(1)	0.047(1)	0.007(1)	0.019(1)	0.016(1)
C(10)	0.048(1)	0.043(1)	0.066(2)	-0.001(1)	0.013(1)	0.017(1)
C(11)	0.048(1)	0.061(2)	0.052(1)	-0.0012(1)	0.012(1)	0.023(1)
C(12)	0.069(2)	0.075(2)	0.042(1)	0.004(1)	0.024(1)	0.033(1)
C(13)	0.055(1)	0.056(1)	0.041(1)	0.008(1)	0.018(1)	0.024(1)
O(1G)	0.088(1)	0.070(1)	0.059(1)	-0.006(1)	0.006(1)	0.023(1)
C(1G)	0.068(2)	0.054(1)	0.048(1)	0.005(1)	0.016(1)	0.022(1)
C(2G)	0.086(2)	0.075(2)	0.063(2)	0.002(1)	0.022(1)	0.046(2)
C(3G)	0.065(2)	0.071(2)	0.061(2)	0.011(1)	0.014(1)	0.027(1)
C(4G)	0.070(2)	0.075(2)	0.057(2)	-0.009(1)	0.012(1)	0.018(1)
C(5G)	0.086(2)	0.075(2)	0.079(2)	-0.009(2)	0.029(2)	0.036(2)
C(6G)	0.068(2)	0.061(2)	0.081(2)	0.007(1)	0.012(1)	0.034(1)
C(7G)	0.071(2)	0.112(3)	0.097(2)	0.029(2)	0.010(2)	0.041(2)

Table 4b Hydrogen co-ordinates and isotropic displacement parameters ($Å^2$) for **DA3M**.

Atoms	x	y	z	U_{eq}
H(1)	0.386(3)	0.76(2)	0.618(2)	0.082(9)
H(3)	0.1308(3)	0.8949(2)	0.5628(2)	0.064(2)
H(4)	-0.0699(3)	0.8455(3)	0.3595(2)	0.064(2)
H(5)	0.0027(3)	0.8665(3)	0.1612(2)	0.064(2)
H(6)	0.2740(3)	0.9400(3)	0.1694(2)	0.064(2)
H(9)	0.4716(3)	1.2580(2)	0.6158(2)	0.064(2)
H(10)	0.4349(3)	1.4288(3)	0.7559(2)	0.064(2)
H(11)	0.3798(3)	1.3698(3)	0.9554(2)	0.064(2)
H(12)	0.3639(3)	1.1424(3)	1.0139(2)	0.064(2)
H(13)	0.3939(3)	0.9676(3)	0.8725(2)	0.064(2)
H(2G1)	0.0651(3)	0.5751(3)	0.3755(3)	0.099(3)
H(2G2)	-0.0298(3)	0.4027(3)	0.3778(3)	0.099(3)
H(3G)	0.0786(3)	0.5224(3)	0.1638(3)	0.099(3)
H(4G1)	-0.0172(3)	0.2786(3)	0.0450(3)	0.099(3)
H(4G2)	-0.0660(3)	0.2101(3)	0.1686(3)	0.099(3)
H(5G1)	0.2618(4)	0.3834(3)	0.1701(3)	0.099(3)
H(5G2)	0.1863(4)	0.2080(3)	0.1691(3)	0.099(3)
H(6G1)	0.1779(3)	0.2448(3)	0.3877(3)	0.099(3)
H(6G2)	0.3567(3)	0.3541(3)	0.3896(3)	0.099(3)
H(7G1)	-0.2018(4)	0.4135(4)	0.0373(3)	0.147(9)
H(7G2)	-0.1675(4)	0.5331(4)	0.1635(3)	0.147(9)
H(7G3)	-0.2482(4)	0.3590(4)	0.1662(3)	0.147(9)

Table 5b Selected torsion angles (°) for **DA3M**.

O1-C1-C2-C7	-117.1(2)	C7_$2-C1-C2-C7	4.1(3)
C8-C1-C2-C7	126.8(2)	O1-C1-C2-C3	61.7(2)
C7_$2-C1-C2-C3	-177.1(2)	C8-C1-C2-C3	-54.4(2)
C7-C2-C3-C4	-0.2(3)	C1-C2-C3-C4	-179.1(2)
C2-C3-C4-C5	0.7(4)	C3-C4-C5-C6	-0.6(4)
C4-C5-C6-C7	-0.1(4)	C3-C2-C7-C6	-0.5(3)
C1-C2-C7-C6	178.3(2)	C3-C2-C7-C1#1	176.7(2)
C1-C2-C7-C1#1	-4.5(3)	C5-C6-C7-C2	0.6(3)
C5-C6-C7-C1#1	-176.7(2)	O1-C1-C8-C9	-172.9(2)
C2-C1-C8-C9	-55.0(2)	C7_$2-C1-C8-C9	69.5(2)
O1-C1-C8-C13	5.9(3)	C2-C1-C8-C13	123.7(2)
C7_$2-C1-C8-C13	-111.7(2)	C13-C8-C9-C10	-1.3(3)
C1-C8-C9-C10	177.4(2)	C8-C9-C10-C11	1.0(3)
C9-C10-C11-C12	0.3(3)	C10-C11-C12-C13	-1.1(4)
C9-C8-C13-C12	0.5(3)	C1-C8-C13-C12	-178.2(2)
C11-C12-C13-C8	0.7(4)	O1G-C1G-C2G-C3G	137.5(3)
C6G-C1G-C2G-C3G	-44.1(3)	C1G-C2G-C3G-C4G	48.6(3)
C1G-C2G-C3G-C7G	175.0(2)	C2G-C3G-C4G-C5G	-55.8(3)
C7G-C3G-C4G-C5G	178.9(3)	C3G-C4G-C5G-C6G	57.3(3)
O1G-C1G-C6G-C5G	-137.5(3)	C2G-C1G-C6G-C5G	44.1(3)
C4G-C5G-C6G-C1G	-50.2(3)		

Symmetry transformations used to generate equivalent atoms:
#1 -x+1,-y+2,-z+1

Appendix C

Structure Factors

Tables of observed and calculated structure factors for **DACH** and **DA3M** are contained in files in the attached diskette. The files are called **DACH**.SFT and **DA3M**.SFT respectively. All files are text files and can be viewed in an editor, under any of the following operating systems:

DOS

WINDOWS 3.1

WINDOWS 95

OS/2

APPLE MAC

UNIX

VMS

Linux